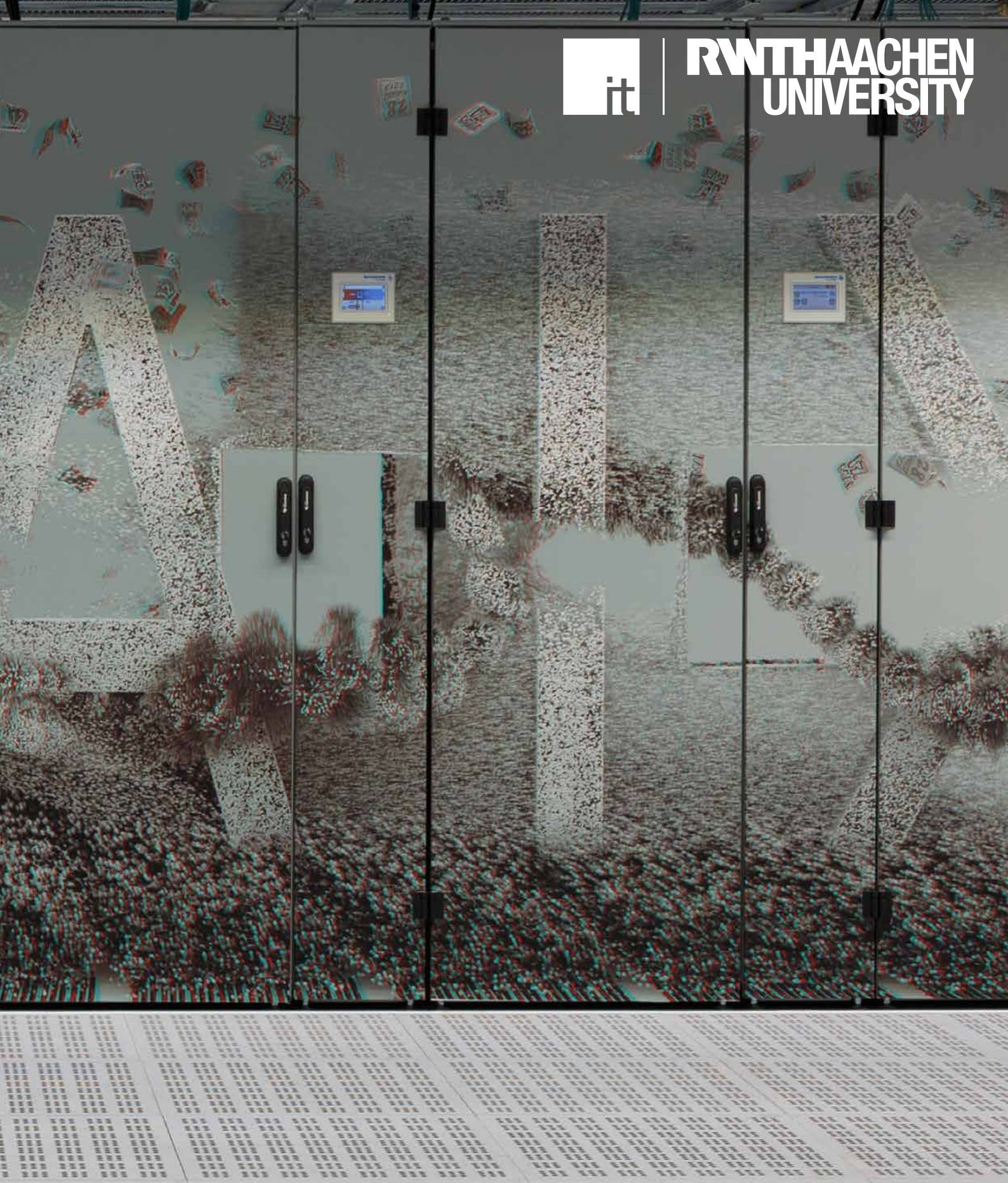

RWTH AACHEN UNIVERSITY

CLAIX Projects 2018

High Performance Computing at RWTH Aachen University

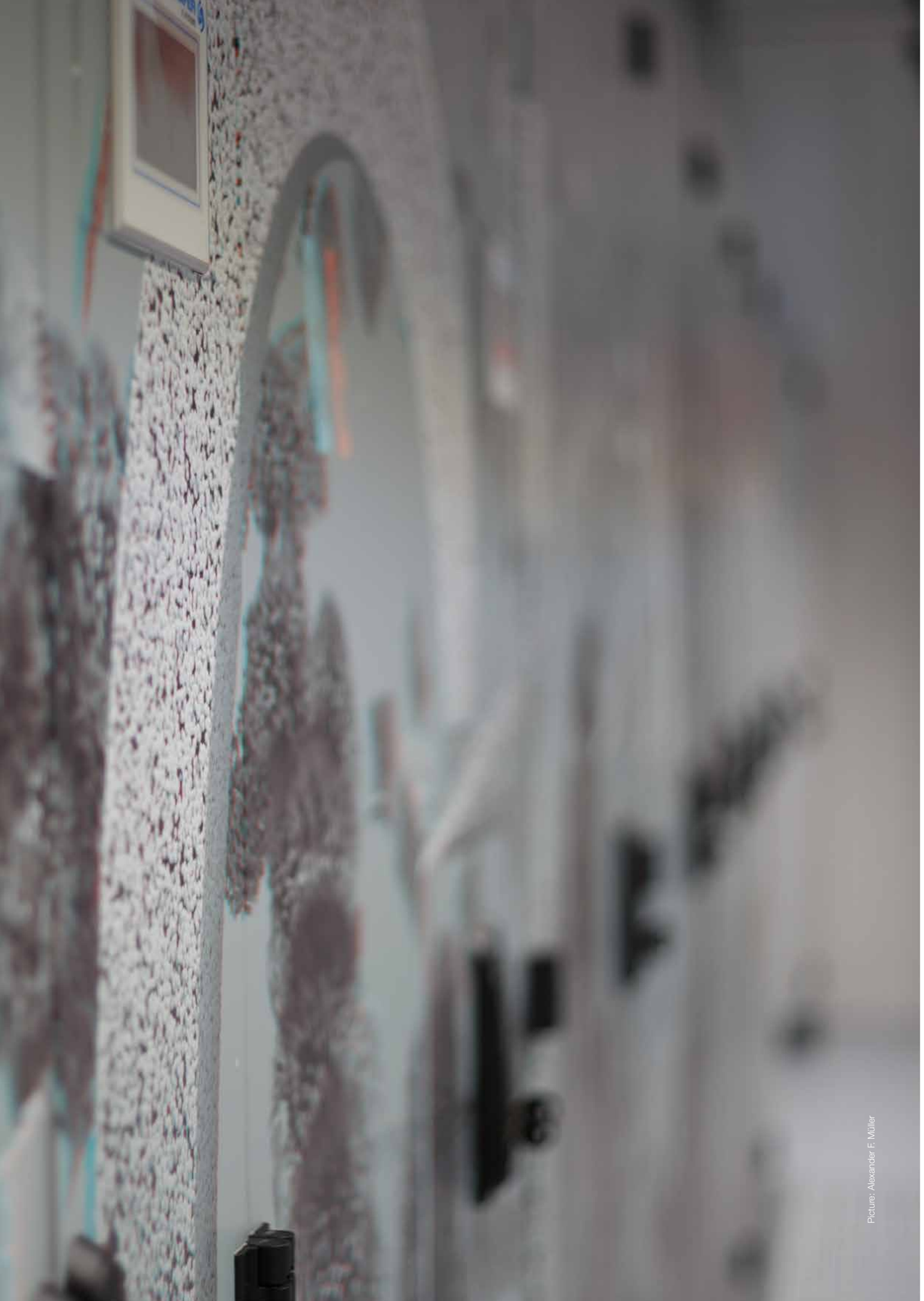

Picture: Alexander F. Müller

CLAIX Projects 2018

High Performance Computing at RWTH Aachen University

Content

Picture: Alexander F. Müller

Preface

Dear reader,

Computer simulations are of enormous importance for many areas of our daily life. You can no longer imagine scientific research without them. This insight is not new and the reason for extensive investments in new and powerful high-performance computers such as the Cluster Aix-la-Chapelle (CLAIX) system at RWTH Aachen University.

Started in 2016 and expanded in 2018, CLAIX is now the fastest high-performance computer at a German University and among the 100 most powerful computer systems in the world (as of June 2019). Since 2016, more than 1300 scientific projects from small “thesis projects” up to large simulations e.g. in engineering sciences consumed almost 800 million compute hours. In this report, we like to present a variety of exciting research projects using the CLAIX system in 2018.

For example, petabytes of precision spectroscopy data about cosmic rays from the AMS detector installed at the international space station were analyzed on CLAIX (see page 86). AMS has been constructed and is now operated by an international collaboration of more than 200 scientists and engineers, the I. Physics Institute B, RWTH Aachen University among others from Europe, America and Asia.

The development of a new video compression standard nicknamed as “Versatile Video Coding” (VVC) is another example for top-class science using CLAIX. The VVC standard is necessary for streaming of 4K-videos or Virtual Reality applications. The design goal of the new standard is to double the compression efficiency compared to previous MPEG standards and thereby making new and emerging applications such as UHD video streaming and immersive video widely available. The Institut für Nachrichtentechnik at RWTH Aachen University is developing the VVC standard together with other international experts in the Joint Video Expert Team (see page 139).

Other projects using computing time on CLAIX include Improvement of Flamelet Models for the Prediction of Soot Emissions from Aero Engines using LES (project by Institute for Combustion Technology, RWTH Aachen University, see page 114) or the Quantum mechanically guided design of ultra-strong metallic glasses (project by Materials Chemistry, RWTH Aachen University, page 124).

Yours sincerely

Matthias Müller

PROF. DR. MATTHIAS MÜLLER

The HPC system CLAIX: Cluster Aix-la-Chapelle

The research projects in this report represent a selection of projects using the high-performance computing system CLAIX - Cluster Aix-la-Chapelle - at RWTH Aachen University in 2018. The system is operated by the IT Center and currently consists of three parts: the Tier-2 part from the procurement phases 2016 and 2018 and the Tier-3 part from the procurement phase 2018.

CLAIX-2016

The system consists of over 600 systems with 2x Intel Xeon Broadwell processors. Specialized node types with up to 144 cores at 1 Terabyte main memory or integrated GPGPUs or NVRAM complete the system for special tasks. All nodes as well as the parallel Lustre file system with a capacity of 3 petabytes are connected with an Intel Omni-Path network at 100-GigaBit/s speed. The overall system achieves a computing power of approx. 670 TeraFlop/s.

CLAIX-2016 started test operation in November 2016 and since December 2016 the system has been available without restriction for use by computing time projects

CLAIX-2018

CLAIX-2018 consists of over 1000 computing nodes with 2x Intel Xeon Skylake processors, each with 24 cores and 192 GB RAM. In addition, there are 48 computing nodes of identical architecture, each equipped with two NVIDIA Volta V100 GPUs (incl. NVLink) as accelerators and available for special applications such as machine learning. A high-performance Lustre-based storage system offers a file system capacity of 10 petabytes and a bandwidth of 150 gigabytes/s (read and write). For interactive work with the system, CLAIX has eight additional dialog systems that are equipped with the same CPUs but have 384 GB more RAM. All nodes are connected to an Intel Omni-Path 100 Gigabit/s network.

The Tier-3 part consists of over 220 compute nodes with identical configuration (6 of those with GPUs) and are fully integrated into the overall cluster.

CLAIX-2018 started test operation in November 2018 and since January 2019 the system has been available without restriction for use by computing time projects.

Application for Compute Time

The allocation of compute time follows the recommendations of the Gauss Alliance for the establishment of nationally coordinated application and approval procedures. Depending on the amount of compute time request, independent national and international experts assess each proposal. According to regulations of the Deutsche Forschungsgemeinschaft (DFG), the Vergabegremium (VGG) of JARA-HPC or RWTH determines detailed scientific and technical criteria for the assessment of proposals for computing time. The VGG is also being supported by experts on operating supercomputers from both facilities.

Technical Summary

	CLAIX-2016	CLAIX-2018
# compute notes for projects	609 standard nodes + special nodes	1080 standard nodes + 221 Tier-3 std. nodes
Processor type	Intel Xeon E5-2650v4 (Broadwell-EP)	Intel Xeon Platinum 8160 (Skylake)
# cores per node	24	48
Main memory per node [GB]	192	128
Capacity of Lustre HPC filesystem	3 PB	10 PB
Bandwidth of Lustre HPC filesystem	45 GB/s	150 GB/s
Theoretical peak performance	0.53 Pflops	3.55 Pflops
LINPACK performance	0.51 PFlops	2.04 Pflops on 2014 nodes

Figure: Front row of the CLAIX-2018 system

Life Sciences

Basic Biological and Medical Research | DFG 201

Picture: kjpargeter / Freepik

Basic Biological and Medical Research | DFG 201

Molecular basis of agonist “access control” across bitter taste receptors

Project ID: jara0165
ALEJANDRO GIORGETTI
Institute for Advanced Simulation
and Institute of Neuroscience and Medicine,
Computational Biomedicine (IAS-5/INM-9),
FZ Jülich

MERCEDES ALFONSO-PRIETO
Institute for Advanced Simulation
and Institute of Neuroscience and Medicine,
Computational Biomedicine (IAS-5/INM-9),
FZ Jülich

FABRIZIO FIERRO
EMILIANO IPPOLITI
PAOLO CARLONI
Institute for Advanced Simulation
and Institute of Neuroscience and Medicine,
Computational Biomedicine (IAS-5, /INM-9),
FZ Jülich

EDA SUKU
Department of Biotechnology,
University of Verona, Verona, Italy

Scientific work accomplished and results obtained

Here we used sub-microsecond long MM/CG molecular dynamics simulations in order to investigate the structural determinants of beta-glucoside binding to hTAS2R16 (Fierro et al., in preparation). We studied three ligands (phenyl-beta-D-glucopyranoside, arbutin and salicin) for which there are extensive experimental data vailable. These three ligands consist of a common glucose ring, covalent bound to a variable phenyl aglycon. First, we run some preliminary simulations to test the accuracy of the parameters used to describe the ligands. After determining the best parameterization, several independent production simulations were run for each ligand, differing in the initial binding pose and in the initial velocities. In particular, two different binding poses were initially tested. The first binding pose is characterized by the phenyl aglycon buried inside the receptor and the glucose ring pointing towards the water solvent (“glucose-out” orientation). The second binding pose has the opposite orientation (i.e. “glucose-in”), as the ligand is rotated by 180 degrees along the membrane axis. Our simulations showed that the latter binding mode, proposed by Sakurai and coworkers (Sakurai 2010a, 2010b), is not stable, and the ligand starts to escape from the binding site after 300-400ns. Instead, for the glucose-out orientation, the phenyl-beta-D-glucopyranoside ligand quickly moved further inside the receptor (after ~12.5 ns) and stayed there for the rest of the simulation (~800ns). The fast convergence of the MM/CG simulation might be due to the reduction of the degrees of freedom respect to an all-atom molecular dynamics. The simulations of the glucose-in binding pose confirmed that all three ligands explore the same binding cavity. Moreover, we found that, for the glucose-out binding pose, two different ligand orientations are possible, differing only by a rotation of 180 degrees around the receptor axis. Our simulations show that both gluco-se-out binding modes are stable and, although they exhibit slightly different protein-ligand interactions, they are both compatible with the available mutagenesis data (with recall values of 0.66-0.83 and precision of 0.8-1.0) and ligand structure-activity relationship data (Bufe et al., 2002; Sakurai et al., 2010a; Sakurai et al., 2010b; Thomas et al., 2017). The existence of a dynamic H-bond network around the binding cavity allows the receptor to establish similar interactions with the ligands in both binding poses, but involving different glucose oxygen atoms. Moreover, the bottom of the binding cavity is lined with aromatic and hydrophobic residues that can interact with the phenyl aglycon. Given that hTAS2R16 can recognize beta-glucosides with very diverse aglycons (Bufe et al., 2002; Sakurai et al., 2010a; Sakurai et al., 2010b; Thomas et al., 2017), we hypothesize that the existence of this dual binding mode may allow to accommodate this broad range of aglycons into the hydrophobic bottom of the binding site (Fierro et al., in preparation).

Realization of the project

As mentioned in section 1, the MD simulations of the hTAS2R16/ligand complexes were performed using the molecular mechanics/coarse grained approach (MM/CG) developed

in our group (Leguebe et al., 2012; Tarenzi et al., 2017). The code employed is an in-house version of GROMACS 4.5.1 (http://www.gromacs.org/) modified in order to introduce the MM/CG routines required for this project and uses pure MPI for parallelization. In this approach, the extracellular part of the receptor, including the binding site with the docked ligand, was treated at atomistic resolution, as well as the water drop (approx. 5,300 molecules) solvating it. In particular, the protein was described using the GROMOS96 43a1 force field (Scott et al., 1999), whereas the SPC model (Berweger et al., 1995) was used for the water molecules. The parameters for the ligands were built by combining the GROMOS 56a6_CARBO forcefield (Plazinski et al., 2016) parameters for the glucopyranose and the PRODRG (Schuttelkopf and van Aalten, 2004) generated parameters for the aglycon. RESP charges (Bayly et al., 1993) were used for all ligands, calculated with Gaussian09 (Frisch et al., 2009) at the B3LYP/6-31G(d,p) level of theory and fitted with Antechamber (Wang et al., 2001). On the other hand, the intracellular part of the receptor, which is not involved in binding, was described at the coarse grained level using a Go-like potential (Go and Abe, 1981) between CG beads centered on the Calpha atoms of the corresponding residues. The MM and the CG parts are connected by an interface region (I), which mediates the bonded and non-bonded interactions between the two levels of resolution. The initial complexes were first minimized in six steps; the first three were performed with the steepest descent algorithm and the last three with the conjugate gradient algorithm. In each minimization step performed with the same algorithm, the maximum step size was progressively increased by one order of magnitude (from 0.001 to 0.01 and to 0.1 nm) and each minimization was run until no changes in potential energy were detected. Next, a simulated annealing protocol was carried out to increase the temperature of the complex from 0 to 300 K in 6 ns using velocity rescaling as thermostat. During the heating, positional restraints were applied on the protein backbone using a force constant of 1000 kJ/mol*nm^2 in each direction of the position vector. After the simulated annealing phase, three further equilibration steps of 3 ns each were performed. In each step, the force constant applied on the protein backbone was progressively decreased (from 500 to 250 and to 125 kJ/mol*nm^2). After removing the restraints, simulations were extended until 800 ns, using a timestep of 2 fs.

We performed eight simulations for each ligand, starting from two different binding poses and running four replicas for each binding pose, differing only for the initial velocities. Since we studied three ligands, this gives a total of 24 simulations. The simulations were performed using either 96 cores (4 nodes, ca. 70% computational efficiency) or 72 cores (in order to optimize the balance between performance and queue waiting time).
We would like to note that here we are not considering the simulations of the glucose-in binding mode (see above), which were stopped in the 300-400 ns timescale, since the ligand was not stable and escaped the binding site. In addition, we are not taking into account the preliminary simulations used to discriminate the best parameterization of the ligands. Indeed, in the first stage of the project, the core hours were not used in a timely manner due to problems with the aforementioned ligand parameterization. We tested different parameterization schemes, ranging from full PRODRG-generated parameters to full GROMOS 56a6_CARBO parameters. These tests show the best structural description of the ligand is achieved by combining the two force fields as described above, in terms of keeping the chair conformation of the glucose ring, as well as minimizing artefactual intramolecular hydrogen bonds between the glucose groups. Hence, the complexes were unfortunately not ready to undergo long production simulations until we found the correct parameters for the ligands.

Theses completed within the project

Mr. Fabrizio Fierro is planning to present his PhD thesis in January 2019 in RWTH Aachen University. His PhD manuscript will include the simulations on hTAS2R16 explained in this report.

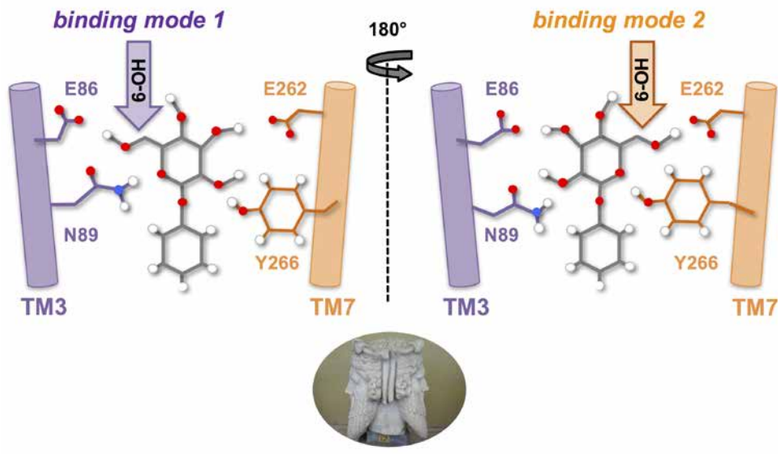

Bitter or sweet? Some sugars are detected by the human bitter taste receptor hTAS2R16 instead of by sweet taste receptors, and thus taste bitter. Within the “bitter sugars” recognized by hTAS2R16, there are cyanogenic glucosides, which are toxic, and thus detecting them as bitter is crucial to avoid their ingestion. However, there are also other hTAS2R16-specific glucosides, present in broccoli, brussels sprouts or berries, whose consumption has health benefits. Therefore, understanding this sweet-taste dichotomy has a potential impact in human health.

References

- BAYLY CI, CIEPLAK P, CORNELL W, KOLLMAN PA.
  A well-behaved electrostatic potential based method using charge restraints for deriving atomic charges: the RESP model. The Journal of Physical Chemistry. 1993;97(40):10269-10280.
- BERWEGER CD, VANGUNSTEREN WF, MULLERPLATHE F.
  Force-Field Parametrization by Weak-Coupling - Reengineering Spc Water. Chemical Physics Letters.1995;232(5-6):429-436. doi: Doi 10.1016/0009-2614(94)01391-8.
- BIARNES X, MARCHIORI A, GIORGETTI A, LANZARA C, GASPARINI P, CARLONI P, ET AL.
  Insights into the binding of Phenyltiocarbamide (PTC) agonist to its target human TAS2R38 bitter receptor. PLoS One. 2010;5(8):e12394. doi: 10.1371/journal.pone.0012394.
- BUFE B, HOFMANN T, KRAUTWURST D, RAGUSE JD, MEYERHOF W.
  The human TAS2R16 receptor mediates bitter taste in response to beta-glucopyranosides. Nat Genet. 2002;32(3):397-401. doi: 10.1038/ng1014.
- CHARLIER L, TOPIN J, DE MARCH CA, LAI PC, CRASTO CJ, GOLEBIOWSKI J.
  Molecular modelling of odorant/olfactory receptor complexes. Methods Mol Biol. 2013;1003:53-65. doi: 10.1007/978-1-62703-377-0_4.
- CHOTHIA C, LESK AM.
  The relation between the divergence of sequence and structure in proteins. EMBO J. 1986;5(4):823-826.
- FIERRO F, SUKU E, ALFONSO-PRIETO M, GIORGETTI A, CICHON S, CARLONI P.
  Agonist binding to chemosensory receptors: a systematic bioinformatics analysis. Frontiers in molecular biosciences. 2017;4:63.
- FIERRO F, ALFONSO-PRIETO M, GIORGETTI A, CARLONI P.
  Molecular basis of human bitter taste receptor selectivity towards “sugar-bitter” agonists. 2018. In preparation.
- FRISCH MJ, TRUCKS G, SCHLEGEL HB, SCUSERIA G, ROBB M, CHEESEMAN J, ET AL.
  Gaussian 09, revision A. 1. Gaussian Inc. Wallingford CT. 2009;27:34.
- GO N, ABE H.
  Non-Interacting Local-Structure Model of Folding and Unfolding Transition in Globular-Proteins. 1. Formulation. Biopolymers. 1981;20(5):991-1011. doi: DOI 10.1002/bip.1981.360200511.

- LAI PC, GUIDA B, SHI J, CRASTO CJ.
  Preferential binding of an odor within olfactory receptors: a precursor to receptor activation. Chem Senses. 2014;39(2):107-123. doi: 10.1093/chemse/bjt060.
- LEGUEBE M, NGUYEN C, CAPECE L, HOANG Z, GIORGETTI A, CARLONI P.
  Hybrid molecular mechanics/coarse-grained simulations for structural prediction of G- protein coupled receptor/ligand complexes. PLoS One. 2012;7(10):e47332. doi: 10.1371/journal.pone.0047332.
- MARCHIORI A, CAPECE L, GIORGETTI A, GASPARINI P, BEHRENS M, CARLONI P, ET AL.
  Coarse-Grained/Molecular Mechanics of the TAS2R38 Bitter Taste Receptor: Experimentally-Validated Detailed Structural Prediction of Agonist Binding. Plos One. 2013;8(5). doi: UNSP e6467510.1371/journal.pone.0064675.
- PLAZINSKI W, LONARDI A, HÜNENBERGER PH.
  Revision of the GROMOS 56A6CARBO force field: Improving the description of ring-conformational equilibria in hexopyranose-based carbohydrates chains. Journal of computational chemistry. 2016;37(3):354-365.
- SAKURAI T, MISAKA T, ISHIGURO M, MASUDA K, SUGAWARA T, ITO K, ET AL.
  Characterization of the beta-D-Glucopyranoside Binding Site of the Human Bitter Taste Receptor hTAS2R16. Journal of Biological Chemistry. 2010;285(36):28373-28378. doi: 10.1074/jbc.M110.144444.
- SAKURAI T, MISAKA T, UENO Y, ISHIGURO M, MATSUO S, ISHIMARU Y, ET AL.
  The human bitter taste receptor, hTAS2R16, discriminates slight differences in the configuration of disaccharides. Biochem Biophys Res Commun. 2010;402(4):595-601. doi: 10.1016/j.bbrc.2010.10.059.
- SANDAL M, BEHRENS M, BROCKHOFF A, MUSIANI F, GIORGETTI A, CARLONI P, ET AL.
  Evidence for a Transient Additional Ligand Binding Site in the TAS2R46 Bitter Taste Receptor. Journal of Chemical Theory and Computation. 2015;11(9):4439-4449. doi: 10.1021/acs.jctc.5b00472.
- SCHUTTELKOPF AW, VAN AALTEN DM. PRODRG:
  a tool for high-throughput crystallography of protein-ligand complexes. Acta Crystallogr D Biol Crystallogr. 2004;60(Pt 8):1355-1363. doi: 10.1107/S0907444904011679.
- SCOTT WRP, HUNENBERGER PH, TIRONI IG, MARK AE, BILLETER SR, FENNEN J, ET AL.
  The GROMOS biomolecular simulation program package. Journal of Physical Chemistry A. 1999;103(19):3596-3607. doi: DOI 10.1021/jp984217f.
- TARENZI T, CALANDRINI V, POTESTIO R, GIORGETTI A, CARLONI P.
  Open boundary simulations of proteins and their hydration shells by Hamiltonian adaptive resolution scheme. Journal of chemical theory and computation. 2017;13(11):5647-5657.
- THOMAS A, SULLI C, DAVIDSON E, BERDOUGO E, PHILLIPS M, PUFFER BA, ET AL.
  The bitter taste receptor TAS2R16 achieves high specificity and accommodates diverse glycoside ligands by using a two-faced binding pocket. Scientific reports. 2017;7(1):7753.
- WANG J, WANG W, KOLLMAN PA, CASE DA.
  Antechamber: an accessory software package for molecular mechanical calculations. J. Am. Chem. Soc. 2001;222:U403.

Publications

- ALFONSO-PRIETO M, NAVARINI L, CARLONI P.
  Understanding ligand binding to G-protein coupled receptors using multiscale simulations. Frontiers in Molecular Biosciences. 2019;6:29. doi: 10.3389/fmolb.2019.00029.
- FIERRO F, GIORGETTI A, CARLONI P, MEYERHOF W, ALFONSO-PRIETO M.
  Dual binding mode of “bitter sugars” to their human bitter taste receptor target. Scientific Reports. 2019. in press, to be published on June 11th 2019. doi: 10.1038/s41598-019-44805-z.
- FIERRO F, ALFONSO-PRIETO M, GIORGETTI A, CARLONI P.
  Molecular basis of human bitter taste receptor selectivity towards “sugar-bitter” agonists. 2018. In preparation.

Selected conference participations

- FABRIZIO FIERRO
  “Bitter sugars” binding to their target human bitter taste receptor hTAS2R16, INM-ICS retreat 2018 (Seventh Annual Retreat of the Institute of Neuroscience and Medicine and the Institute of Complex Systems), FZ Jülich, July 02-03, 2018
- MERCEDES ALFONSO-PRIETO
  Multiscale simulations of chemosensory receptors, Kick-off workshop of the FIRST project on Multiscale Simulation, Vietnam National University, University of Science, Hanoi, Vietnam, January 19, 2018
- MERCEDES ALFONSO-PRIETO
  Multiscale simulations of chemosensory receptors, CECAM workshop “Physiological role of ions in the brain: towards a comprehensive view by molecular simulation”, Scuola Normale Superiore Pisa, Italy, May 21-23, 2018
- MERCEDES ALFONSO-PRIETO
  How sugars can taste bitter: multiscale simulations of the human bitter taste receptor hTAS2R16, 7th International Conference on the Development of Biomedical Engineering “Recent computational and experimental advances in molecular medicine”, Biomedical Engineering Department, International University & Vietnam National University HCMC, Ho Chi Minh City, Vietnam, June 27-29, 2018
- FABRIZIO FIERRO
  E Molecular basis of bitter taste receptor selectivity towards bitter sugars, European ChemoReception Organization (ECRO) meeting 2018, Würzburg, Germany, September 05-08, 2018
- FABRIZIO FIERRO
  “Bitter sugars” binding to their target human bitter taste receptor hTAS2R16, INM-ICS retreat 2018 (Seventh Annual Retreat of the Institute of Neuroscience and Medicine and the Institute of Complex Systems), FZ Jülich, July 02-03, 2018
- MERCEDES ALFONSO-PRIETO
  Multiscale simulations of chemosensory receptors, Kick-off workshop of the FIRST project on Multiscale Simulations, Vietnam National University, Hanoi University of Science, Hanoi, Vietnam, January 19, 2018
- MERCEDES ALFONSO-PRIETO
  Multiscale simulations of chemosensory receptors, CECAM workshop “Physiological role of ions in the brain: towards a comprehensive view by molecular simulation”, Scuola Normale Superiore Pisa, Italy, May 21-23, 2018
- MERCEDES ALFONSO-PRIETO
  How sugars can taste bitter: multiscale simulations of the human bitter taste receptor hTAS2R16, 7th International Conference on the Development of Biomedical Engineering “Recent computational and experimental advances in molecular medicine”, Biomedical Engineering Department, International University & Vietnam National University HCMC, Ho Chi Minh City, Vietnam, June 27-29, 2018

National and international cooperations

- Ernesto Illy Foundation, Trieste, Italy
- illy Caffè S.p.A, Trieste, Italy

Functional Implications of Isocitrate Dehydrogenase 1 (IDH1) and its Cancer-Related Mutation R132H

Project ID: jara0170
RICCARDO GUARESCHI
Institute for Advanced Simulations, Computational Biomedicine (IAS-5/INM-9), FZ Jülich

Work done:

Epigenetic modifications[1] are emerging as a crucial factor for the regulation of life processes[2–4]. These modifications are chemical alterations performed by specific enzymes that act upon DNA or histone proteins. Importantly, recent findings have associated specific mutated forms of these enzymes to abnormal catalytic activity that is frequently connected to a wide spectrum of diseases, included cancer[5,6]. Therefore, to understand how epigenetic enzymes work and how mutations affect their function may help the discovery of innovative medicines[2,4,7]. In this scenario, the epigenetic modification enzyme isocitrate dehydrogenase 1 (IDH1), plays a central role in the control of metabolic pathways and epigenetic traits[8,9]. Remarkably, the single R132H mutation drastically alters the catalytic activity of IDH1, inducing a complete new enzymatic activity. That is, the mutated form R132H catalyzes the reduction of aKG to 2-hydroxyglutarate (2HG)[10]. This is radically different from the function of the wild-type (WT) form of IDH1 that ultimately synthesizes aKG from isocitrate (ICT), as shown in Figure 1. While high-resolution X-ray structures of IDH1 have been recently solved, the mechanisms for IDH1 catalysis and how the cancer-related mutation R132H affects IDH1 function, remain largely unclear.

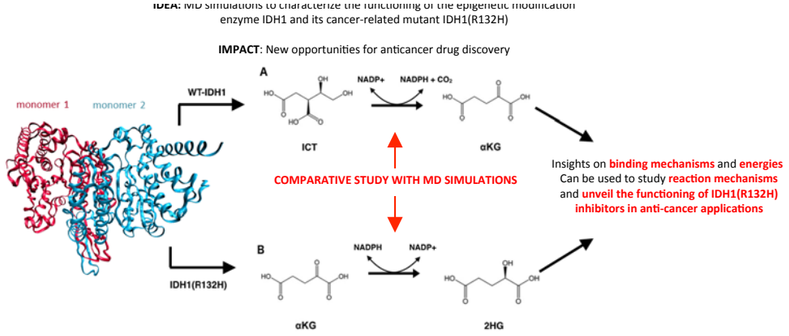

Figure 1: Overview of the proposed study

Based on these experimental evidence and structural data, here we will use multiscale molecular simulations to understand how the epigenetic modification enzyme IDH1, and its mutant R132H, operate at the molecular level. Setup of the simulations for (WT) IDH1 and R132H IDH1: Both systems underwent energy minimization, followed by NVT and NPT equilibration. Production runs have been started and preliminary analyses have been carried out. It was noticed that stronger constraints needed to be added to avoid the breakdown of the catalytic complex around the Fe(II) ion present in the active site. The production run was restarted with updated parameters. The project suffered a major slowdown, because the candidate Ph.D. student that was carrying out the simulations suddenly abandoned its position. I am looking for new candidates to carry out this project. Local resources will be used to this aim.

References

[01] BERGER SL, KOUZARIDES T, SHIEKHATTAR R, SHILATIFARD A.
An operational definition of epigenetics. Genes Dev. 2009;23:781–783.
[02] PORTELA A, ESTELLER M.
Epigenetic modifications and human disease. Nat. Biotechnol. 2010;28:1057–1068.
[03] ZOGHBI HY, BEAUDET AL.
Epigenetics and Human Disease. Cold Spring Harb. Perspect.Biol. 2016;8.
[04] EGGER G, LIANG G, APARICIO A, JONES PA.
Epigenetics in human disease and prospects for epigenetic therapy. Nature. 2004;429:457–463.
[05] GALLUZZI L, KEPP O, VANDER HEIDEN MG, KROEMER G.
Metabolic targets for cancer therapy. Nat Rev Drug Discov. 2013;12:829–846.
[06] KONDO Y.
Epigenetic Cross-Talk between DNA Methylation and Histone Modifications in Human Cancers. Yonsei Med. J. 2009;50:455–463.
[07] HALUSKOVA J.
Epigenetic studies in human diseases. Folia Biol. 2010;56:83–96.
[08] WONG CC, QIAN Y, YU J.
Interplay between epigenetics and metabolism in oncogenesis: mechanisms and therapeutic approaches. Oncogene. 2017;1–16. doi:10.1038/onc.2016.485
[09] BORODOVSKY A, SELTZER MJ, RIGGINS GJ.
Altered cancer cell metabolism in gliomas with mutant IDH1 or IDH2. Curr. Opin. Oncol. 2012;24:83–89.
[10] DANG L, ET AL.
Cancer-associated IDH1 mutations produce 2-hydroxyglutarate. Nature. 2009;462:739–744.

Selected conference participations

- EuroQSar2018, September 2018, Thessaloniki, Greece

Selected national and international cooperations

- VNU-KeyLab, VNU University of Science, Hanoi, Vietnam

Adenylyl Cyclase-catalyzed reaction mechanism of ATP cyclization

Project ID: jara0163

EMILIANO IPPOLITI
Institute for Advanced Simulations (IAS-5),
Institute for Neuroscience and Medicine (INM-9),
FZ Jülich

RODRIGO CASASNOVAS PERERA
Universitat de les Illes Balears, Spain

PAOLO CARLONI
Institute for Advanced Simulations (IAS-5),
Institute for Neuroscience and Medicine (INM-9),
FZ Jülich

VIACHESLAV BOLNYKH
Faculty of Mathematics,
Computer Science and Natural Sciences,
RWTH Aachen University

Scientific work accomplished and results obtained:

During the granting period we have investigated the enzymatic mechanism of adenylyl cyclase (AC) in complex with its activator protein G_sa. ACs are key component of many signaling cascades [1] and their role is to catalyze the conversion of adenosine triphosphate (ATP) to cyclic adenosine monophosphate (cAMP), a second messenger involved in signaling cascade pathways. This type of reactions are ubiquitous in biology, yet they are still not fully understood and highly debated in literature, especially because of the role played by metal ions (Mg^{2+}) and water molecules [2-4].

This project is part of the effort in the context of the Human Brain Project (HBP, www.humanbrainproject.eu). Our research group is one of the five groups dedicated to molecular simulation in the Brain Simulation Platform (i.e. sub- project 6 or SP6) of HBP. While other partners in the molecular simulation team perform protein diffusion simulations in crowded environments or coarse - grain simulations of protein - protein complexes, our task is to provide atomistic information of enzyme - catalyzed chemicalreactions and of protein - ligand binding and unbinding processes that govern neuronal cascades.

Our modeling started with the structural data of a mammalian $G_s\alpha$ domain interacting with its downstream effector AC (PDB: 1CJK) [5, 6]. In this crystallographic structure, AC is a pseudosymmetric heterodimer made by subunits C1 and C2 from isoforms AC5 and AC2, respectively, which form a catalytic dimer. The C1 - C2 interface is indeed the catalytically active region. Two Mg^{2+} ions, bound to ATP, are known to be crucial for the enzymatic catalysis [7]. C2 binds to an ATP analog, to $G_s\alpha$•GTP and to forskolin (a nonphysiological diterpene ligand). The presence of either $G_s\alpha$•GTP or forskolin increases the catalytic activity significantly, and the two interactors work synergistically (Table 1).

Activator	Activity [μmol/(min mg)]	$\Delta G^{\neq}$ [kcal/mol]
None	≈ 0	
$G_s\alpha$•GTP	≈ 55	≈ 15.7
Forskolin	≈ 55	≈ 15.7
$G_s\alpha$•GTP + forskolin	≈ 150	≈ 15.1

Table 1. Adenylyl cyclase activity in the presence and absence of activators and estimated activation free energies $\Delta G^{\neq}$ [8-10].

This experimentally observed increase in catalytic activity is supposed to arise, at least in part, from a change in the conformation of the C1/C2 interface: $G_s\alpha$ along with forskolin induces a rotation of C2 relative to C1 and promotes a transition from an 'open' to a 'closed' active site around ATP [11]. In fact, our force field - based long - timescale molecular dynamics simulations confirm this hypothesis showing that the binding of $G_s\alpha$ to AC steers the ATP and the residues close together in the active site into a configuration favorable for the ATP to cAMP reaction. In particular, the side chain of residue Arg1029 is steered 11 Å towards the active site to finally hydrogen - bond ATP [12]. Moreover, $G_s\alpha$ and ATP synergistically stabilize each other when binding simultaneously in the AC:ATP:$G_s\alpha$ complex.

From this structural information we have built a hybrid quantum mechanical / molecular mechanical (QM/MM) model in order to characterize at molecular level the mechanism of the enzymatic conversion from ATP to cAMP, which involves the hydrolysis of the Pα atom of ATP. The first model was successfully equilibrated but subsequently it resulted to be instable losing the original coordination of the Mg^{2+} ion. The second model was stable during the testing molecular dynamics run but instabilities came out when metadynamics step was attempted. Finally, the third model, obtained by including additional water molecules in the enlarged QM box and improving the partial charge accuracy of the classical atoms close to the boundaries of the QM region, provided a fully stable system.

We assumed the reaction proceeds via the nucleophilic attack of ribose oxygen O3' to the alpha phosphorous (Pα) of the ATP triphosphate moiety. Four independent metadynamics simulations were planned in order to obtain the free energy profiles of the four steps depicted in Fig. 1, namely: 1) the nucleophilic attack of the protonated O3' to Pα, 2) the proton transfer of the protonated cAMP O3' to the Oγ of the resulting pyrophosphate, 3) the proton transfer from O3' to Oγ before the nucleophilic attack, and 4) the nucleophilic attack of the deprotonated O3' to Pα.

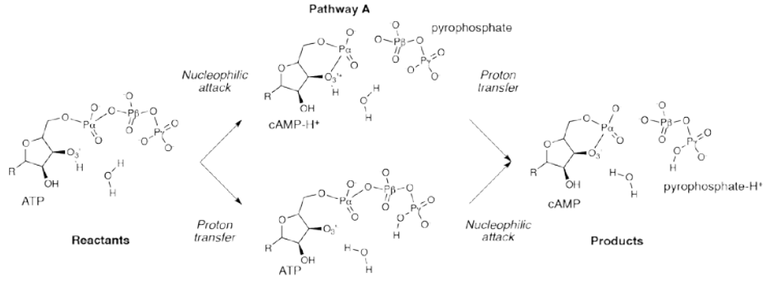

Figure 1. Possible reaction mechanisms for the AC-catalyzed ATP to cAMP conversion. Only the reacting atoms of ATP and one water molecule in the active site are shown. Protein atoms, Mg^{2+} ions and bulk water are removed for clarity. The substituent R in the ATP ribose stands for the adenine moiety of ATP.

Due to the reduction of the requested allocation and the resources used up to build a stable QM/MM model and overcome the stability issues previously mentioned, only the first two metadynamics simulations have been completed within the granted period. We are going to finalize the project by perform the two missing metadynamics runs in the next months by using computational resources from our HBP partners involved in the project as well. The four simulations altogether are essential to get a complete picture of the reaction mechanism. In fact, from the free energy profiles of each simulation we can calculate the free energy barrier of the enzymatic reaction and, by recalling the transition state theory, the associated microscopic kinetic constant of that step. With this information we can identify the dominant, i.e. the most kinetically favorable, reaction pathway or if the two pathways are both kinetically important because they present similar free energy barriers.

In addition, the analysis from the first two simulations supports the hypothesis that the interaction of the ATP phosphate moiety with the positively charged side chain of Arg1029 reduces the free energy barrier of this step (Fig. 2). This effect is due to the polarization of Pa, which favors the addition of the O3' electron density to form the O3'-Pa bond. The interaction of the phosphate moiety with the two Mg^{2+} ions also polarizes Pa and favors the nucleophilic attack for the same reason.

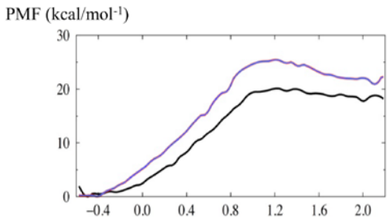

Figure 2. Potential of mean force along the reaction coordinate calculated as the difference of the distances O3'- Pα and OS- Pα for the AC-catalyzed ATP to cAMP reaction with a protonated (black line) or deprotonated (violet line) arginine R1029.

Realization of the project

Preliminary force field - based long - timescale molecular dynamics simulations for the AC:ATP:$G_s\alpha$ complex were performed with the GROMACS code [13] using the AMBER99SB-ildn force field [14-18] for the protein, the Joung et al. parameters for K^+ and Cl^- [19] and the Allnér et al. parameters for the Mg^{2+} ions [20], TIP3P [21] for water and GAFF [22] for the ATP. The K^+ and Cl^- ions were used to neutralize the system and to reproduce the physiological ionic strength. First the systems were equilibrated at 310 K and 1 bar with the CSVR thermostat [23] and Parrinello - Rahman barostat [24], respectively. Then, 1.5 ms - long NPT simulations were performed to investigate the effect of $G_s\alpha$ and ATP on the conformation of the AC active site.

From a stable configuration of the classical molecular dynamics we start to build a QM/MM model in order to characterize the enzymatic conversion from ATP to cAMP. With the first attempt we equilibrated a QM/MM system that resulted to be unstable during the Car - Parrinello molecular dynamics test. The second built model passed all the preliminary tests after equilibration but it showed instabilities during the metadynamics runs and no reliable free energy profile could be obtained. Finally, after enlarging the QM part in order to include a larger number of water molecules and after improving the partial charges associated to the classical atoms close to the boundaries of the QM region, we obtained a stable QM/MM model that we have used for the subsequent metadynamics simulations. All the QM/MM simulations were performed with the code CPMD (www.cpmd.org) version 4.1 [25] in combination with the QM/MM interface developed by Röthlisberger and co - workers [26] based on the Gromos MD engine [27]. In particular, the quantum region of the stable model, treated at DFT level, comprised 97 atoms in total, including the ribose and triphosphate moieties of ATP, the two Mg^{2+} ions and their coordinating environment: the side chains of D396 and D440, the backbone amide unit I297/E298, all the water molecules in the quantum box, and K1065 and R1029 side chains. The remaining part of the system (~183.000 atoms) was treated at AMBER99SB - ildn force field level along with the latest parameters for ions in order to keep consistency with the previous classical molecular dynamics simulations. The quantum problem was solved within the BLYP functional approximation expanding the wave function in a plane wave basis set up to 80 Ry in a parallelepiped QM box with the size of 37.4 a.u. x 42.3 a.u. x 43.1 a.u.. Only the valence electrons were treated explicitly, while the core electrons were described using norm - conserving pseudopotentials of the Martins–Troullier type [28]. Adapted monovalentcarbon pseudopotential was employed to saturate the dangling bonds in between the QM and MM regions [29]. Isolated system conditions were imposed in the QM part by employing the Martyna - Tuckerman scheme [30]. A quadratic potential was used to avoid that water molecules treated at the QM level diffuse out of the QM box. We run all the simulations in a setup with 96 cores as planned.

The equilibration step consisted of an initial annealing molecular dynamics simulation where the small fraction of the kinetic energy of the system was regularly extract from the system in order to reach a minimal energy configuration. In fact, the CPMD QM/MM implementation does not allow directly performing an energy minimization run. Subsequently, we performed an additional 5ps - long equilibration run, using an integration time - step of ~0.12 fs. During the first 2.5 ps of this run the temperature was gradually increased up to 300 K, while during the rest of the equilibration run the temperature was kept constant at 300 K using a velocity rescaling thermostat.

The subsequent testing step consisted of a 20ps - long Car - Parrinello molecular dynamics simulatio in the NVT ensemble where the temperatures of both QM and MM parts were maintained at 300 K through a Nosé - Hoover thermostat [31] with a 4000 cm^{-1} coupling frequency.

Finally, we performed the first two metadynamics runs [32] (with 1 and 2 collective variables, respectively) in order to accelerate the phase space exploration along the collective variables described in the proposal and to reconstruct the corresponding free energy surfaces associated to the partial reactions depicted in Fig. 1. In particular, we employed the well tempered flavour of metadynamics algorithm [33 - 34] in combination with the multiple walker approach [35] that leads to a fully linear scaling algorithm with respect to the number of employed “walkers”: loosely interacting (almost independent) metadynamics runs (two in our case) performed at the same time to calculate each free energy profile. For each metadynamics simulation the bias potential of the metadynamics algorithm was added every 100 steps. After preliminary short trial runs by using large bias depositions in order to have a rough estimation of the underlying free energy landscape, the height of the deposited hills was selected as about 5% of the estimated free energy barriers. The rest of the setup for the metadynamics runs was identical to the testing step mentioned above. As mentioned in the previous section, we could not run the other two planned metadynamics simulations within the granted period. However, the project is proceeding and the rest of the simulations are currently running by using computational resources from HBP partners involved in the project.

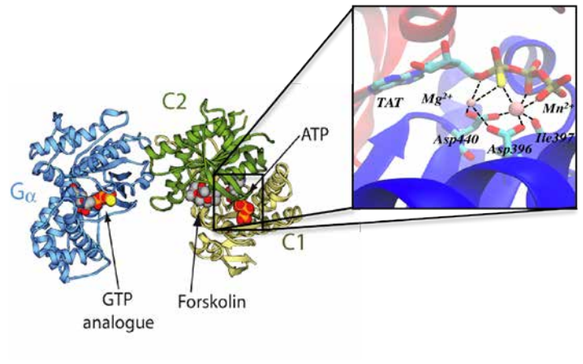

Figure 3. Crystal structure of the dimeric catalytic cytoplasmic domains of the transmembrane adenylyl cyclase protein (AC) in complex with $G_s\alpha$ - GTP, forskolin and an ATP molecule. Inset: Active site of AC in the crystal structure, including one Mg^{2+} and one Mn^{2+} ions and the ATP molecule. In this case Mn^{2+} replaces a second Mg^{2+} ion in order to help crystalizing the complex with the ATP analogue. The C1 and C2 domains of AC are depicted in the inset as blue and red secondary structure cartoon, respectively.

References

[1] LINDER JU, SCHULTZ JE.
The class III adenylyl cyclases: multi-purpose signalling modules. Cellular Signalling. 2003;15(12):1081-1089.

[2] KLAEHN M, ROSTA E
Warshel A. On the mechanism of hydrolysis of phosphate monoesters dianions in solutions and proteins. Journal of the American Chemical Society. 2006;128(47):15310-15323.

[3] PRASAD BR, PLOTNIKOV NV, WARSHEL A.
Addressing Open Questions about Phosphate Hydrolysis Pathways by Careful Free Energy Mapping. Journal of Physical Chemistry B. 2013;117(1):153-163.

[4] GENNA V, et al.
A Self-Activated Mechanism for Nucleic Acid Polymerization Catalyzed by DNA/RNA Polymerases. Journal of the American Chemical Society. 2016;138(44):14592-14598.

[5] TESMER JJG, et al.
Two-metal-ion catalysis in adenylyl cyclase. Science. 1999;285(5428):756-760.

[6] TESMER JJG, et al.
Crystal structure of the catalytic domains of adenylyl cyclase in a complex with G(s alpha). GTP gamma S. Science. 1997;278(5345):1907-1916.

[7] PALERMO G, et al.
Catalytic Metal Ions and Enzymatic Processing of DNA and RNA. Accounts of Chemical Research. 2015;48(2):220-228.
[8] WHISNANT RE, GILMAN AG, DESSAUER CW.
Interaction of the two cytosolic domains of mammalian adenylyl cyclase. Proc Natl Acad Sci USA. 1996;93:6621-6625.
[9] SUNAHARA RK, et al.
Interaction of Gsalpha with the cytosolic domains of mammalian adenylyl cyclase. J Biol Chem. 1997;272(35):22265-71.
[10] DESSAUER CW, SCULLY TT, GILMAN AG.
Interactions of forskolin and ATP with the cytosolic domains of mammalian adenylyl cyclase. J Biol Chem. 1997;272(35):22272-7.
[11] TESMER JJG.
The quest to understand heterotrimeric G protein signaling. Nature Structural & Molecular Biology. 2010;17(6):650-652.
[12] FREZZA E, MARTIN J, LAVERY R.
A molecular dynamics study of adenylyl cyclase: The impact of ATP and G--protein binding. PLoS ONE. 2018;13(4):e0196207.
[13] HESS B, et al.
GROMACS 4: Algorithms for highly efficient, load-balanced, and scalable molecular simulation. Journal of Chemical Theory and Computation. 2008;4(3):435-447.
[14] CHEATHAM TE, CIEPLAK P, KOLLMAN PA.
A modified version of the Cornell et al. force field with improved sugar pucker phases and helical repeat. Journal of Biomolecular Structure & Dynamics. 1999;16(4):845-862.
[15] CORNELL WD, et al.
A 2nd generation force-field for the simulation of proteins, nucleic acids, and organic molecules. J. Am. Chem. Soc. 1995;117:5179.
[16] Wang J, Cieplak P, Kollman PA.
How well does a restrained electrostatic potential (RESP) model perform in calculating conformational energies of organic and biological molecules? Journal of Computational Chemistry. 2000;21(12):1049-1074.
[17] HORNAK V, et al.
Comparison of multiple Amber force fields and development of improved protein backbone parameters. Proteins: Structure, Function, and Bioinformatics. 2006;65(3):712-725.
[18] LINDORFF-LARSEN K, et al.
Improved side-chain torsion potentials for the Amber ff99SB protein force field. Proteins: Structure, Function, and Bioinformatics. 2010;78(8):1950-1958.
[19] JOUNG IS, CHEATHAM TE.
Determination of Alkali and Halide Monovalent Ion Parameters for Use in Explicitly Solvated Biomolecular Simulations. The Journal of Physical Chemistry B. 2008;112(30):9020-9041.
[20] ALLNÉR O, NILSSON L, VILLA A.
Magnesium Ion–Water Coordination and Exchange in Biomolecular Simulations. Journal of Chemical Theory and Computation. 2012;8(4):1493-1502.
[21] JORGENSEN WL, et al.
Comparison of simple potential functions for simulating liquid water. J. Chem. Phys. 1983;79(2):926-935.
[22] WANG JM, et al.
Development and testing of a general amber force field. Journal of Computational Chemistry. 2004;25(9):1157-1174.
[23] BUSSI G, DONADIO D, PARRINELLO M.
Canonical sampling through velocity rescaling. The Journal of Chemical Physics. 2016;126(1):014101.
[24] PARRINELLO M, RAHMAN A.
Polymorphic transitions in single crystals: A new molecular dynamics method. Journal of Applied Physics. 1981;52(12):7182-7190.
[25] HUTTER J, ET AL. CPMD,
http://www.cpmd.org/, Editor. 2000-2012. Copyright IBM Corp, MPI für Festkörperforschung Stuttgart.
[26] LAIO A, VANDEVONDELE J, ROTHLISBERGER U.
A Hamiltonian electrostatic coupling scheme for hybrid Car-Parrinello molecular dynamics simulations. Journal of Chemical Physics. 2002;116(16):6941-6947.
[27] VAN GUNSTEREN WF, BILLETER SR, EISING AA, HÜNENBERGER PH, KRÜGER P, MARK AE, SCOTT WRP, TIRONI IG.
Biomolecular Simulation: The GROMOS96 Manual and User Guide. Vdf Hochschulverlag AG an der ETH Zürich. 1996;1-1042.
[28] TROULLIER N, MARTINS JL.
Efficient pseudopotentials for plane-wave calculations. Phys Rev B Condens Matter. 1991;43(3):1993-2006.
[29] VON LILIENFELD OA, et al.
Variational optimization of effective atom centered potentials for molecular properties. J Chem Phys. 2005;122(1):14113.
[30] MARTYNA GJ, TUCKERMAN ME.
A reciprocal space based method for treating long range interactions in ab initio and force-field-based calculations in clusters. The Journal of chemical physics. 1999;110(6):2810-2821.
[31] BARDUCC A, BUSSI G, PARRINELLO M.
Well-Tempered Metadynamics: A Smoothly Converging and Tunable Free-Energy Method. Physical Review Letters. 2008;100:020603.
[32] ENSING B, et al.
Metadynamics as a tool for exploring free energy landscapes of chemical reactions. Acc Chem Res. 2006;39(2):73-81.
[33] NOSÉ S.
A unified formulation of the constant temperature molecular-dynamics methods. Journal of Chemical Physics. 1984;81(1):511–519.
[34] HOOVER WG.
Canonical dynamics: Equilibrium phase-space distributions. Phys. Rev. A. 1985;31(3):1695–1697.
[35] RAITERI P, et al.
Efficient Reconstruction of Complex Free Energy Landscapes by Multiple Walkers Metadynamics. The Journal of Physical Chemistry B. 2006;110(8):3533-3539.

Selected conference participations

- 2018 BioExcel Summer School on Biomolecular Simulations, Pula, Italy, June 18-22, 2018
- FIRST project kick-off workshop on multiscale simulations, Hanoi, Vietnam, January 18, 2018

Selected national and international cooperations

- University de les Illes Balears, Spain
- Universiteit Utrecht, The Netherlands
- The Cyprus Institute, Cyprus
- École polytechnique fédérale de Lausanne, Switzerland
- Universidad de los Andes, Colombia

Molecular dynamics of the SLC26 family of ion channels and transporters

Project ID: jara0177
JAN-PHILIPP MACHTENS
Institute of Complex Systems, Cellular Biophysics (ICS-4), FZ Jülich

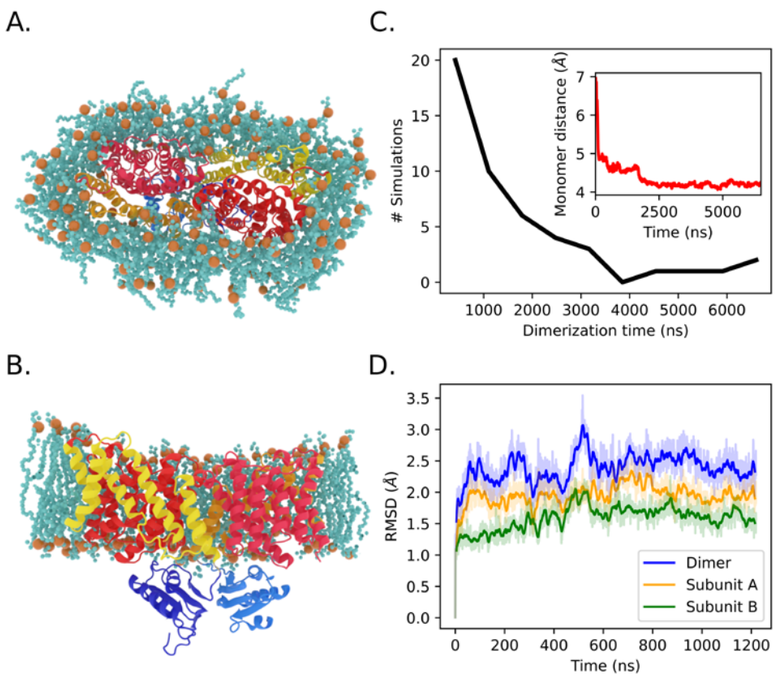

Multiscale molecular dynamics simulations to obtain the native dimeric structure of SLC26 transporters.

The SLC26 protein family of anion channels and transporters plays essential roles in human physiology, and dysfunction is related with a variety of diseases such as chronic diarrhea or deafness. Here, multiscale molecular dynamics simulations of SLC26Dg, a bacterial homologue of the human SLC26 family with known X-ray crystal structure in the monomeric state, have been performed to obtain the native dimeric structure in a membrane environment that is required for SLC26 function.

A,B, Coarse-grained molecular dynamics (MD) was used to simulate spontaneous formation of dimers, starting from separated monomers (A, top view on a representative dimer; B, side view). C, Histogram of dimerization times in independent coarse-grained simulations. D, Dimer structures obtained by coarse-grained simulations were transformed to all-atom representation. All-atom MD simulations show good structural stability as indicated by root-mean-squared deviations to the starting structure.

Selected conference participations

- Conference presentation at the 63th Annual Meeting of the Biophysical Society (Baltimore, MD, USA). Bridging the Gap between Functional and Structural Data, Verena Burtscher, Matej Hotka, Thomas Stockner,Jan-Philipp Machtens, Walter Sandtner, DOI:https://doi.org/10.1016/j.bpj.2018.11.2997

Selected national and international cooperations

- DOMINIK OLIVER
  Institut für Physiologie, Uni Marburg, Germany
- ERIC GEERTSMA
  Institute of Biochemistry, Biocenter N200/1.08, Goethe-University Frankfurt, Germany

Natural Sciences

Molecular Chemistry | DFG 301
Chemical Solid State and Surface Research | DFG 302
Physical and Theoretical Chemistry | DFG 303
Condensed Matter Physics | DFG 307
Particles, Nuclei and Fields | DFG 309
Astrophysics and Astronomy | DFG 311

Picture: Katemangostar / Freepik

Molecular Chemistry | DFG 301

Computational studies of reactivities in organic and organometallic transformations

Project ID: jara0091
FRANZISKA SCHOENEBECK
Institute of Organic Chemistry,
RWTH Aachen University

Our research group is interested in understanding reactivity and mechanisms, with an ultimate goal of designing new catalysts, reactivities and transformations. By combining computational and experimental approaches, the group has investigated and discovered a number of reactivity phenomena. More specifically, we have studied divergent reactivities in transmetalation of the trifluoromethyl moiety,[1] as well as the effects of ligand in C-TeCF$_3$ bond formation.[2] Moreover, in continuation of our longstanding interest in the reactivity of dinuclear palladium complexes we have gained further mechanistic insights on their reactivities in cross-coupling reactions.[3] Furthermore, we have also explored the selectivity of trinuclear palladium complexes in oxidative addition.[4] Recently we have also broadened our research program by dynamics simulations in order to explore new reactivity phenomena that cannot be explained through classical transition state theory, i.e. dynamic effects.[1b] In the following two projects should be highlighted.

(1) Mechanistic Insights into Hiyama Transmetalation

During our research we achieved significant progress in study of the mechanism transmetallation of Hiyama couplings.[1b] By using the combination of transition state calculations and state-of-the-art Born-Oppenheimer molecular dynamics (BOMD) simulations, a new mechanistic picture of the transfer of CF_3 moiety from silanes to a Palladium center was uncovered (Scheme 1). In the unprecedented mechanism, a novel five-membered transition state leads to the activation of the Si-C bond in silanes, followed by the formation of a free difluorocarbene, which then recombines with Pd and undergoes a facile [1,2]-fluoride shift that forms the Pd-CF_3 intermediate.

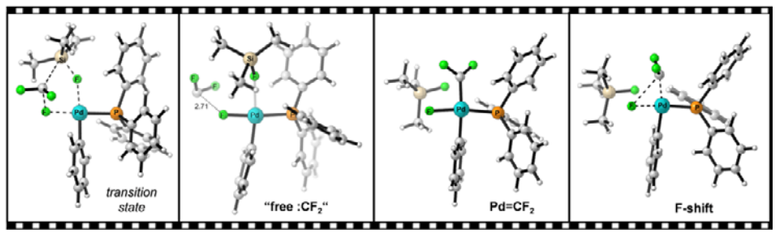

Scheme 1. Selected snapshots from DFT-based BOMD simulations initiated from the transmetalation transition state.

(2) Pd(I) dimer reactivity

Based on our previous studies of dinuclear reactivity at Pd(I)-Pd(I), we studied the mechanism of dinuclear Pd(I)-mediated thiolation (Scheme 2). In line with previous results, we found that the transition state for dinuclear oxidative addition of aryl iodide to thiolate-bridged [(PtBu$_3$)PdI(μ-SEt)]$_2$ dimer was favored over alternative modes of activation, such as

substitution or activated exchange mechanisms. Moreover, we found that a Pd(I) dimer containing mixed iodide/thiolate-bridges was more reactive than the doubly thiolate-bridged Pd(I) dimer both with regards to oxidative addition and reductive elimination ($\Delta\Delta G^{\ddagger}$ = 6.1 and 10.7 kcal/mol, respectively). In line with previous results, the dinuclear catalytic cycle is thermodynamically driven with driving forces of 17.9 and 13.0 kcal/mol for the two consecutive catalytic cycles.

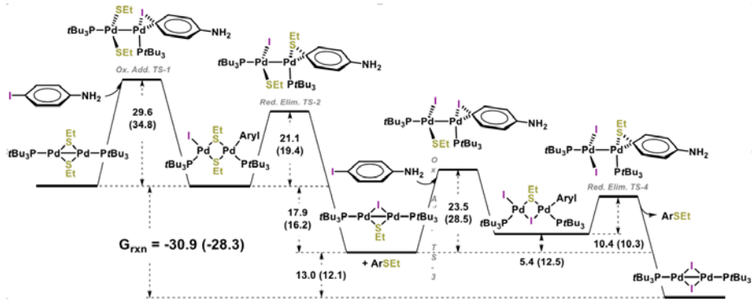

Scheme 2. Gibbs free energy pathway for dinuclear Pd(I)-mediated C(sp^2)-SEt bond formation. Energies (in kcal/mol) were calculated at the CPCM (toluene) M06L/6-311++G(d,p) [SDD for Pd,I] or CPCM (toluene) M06L/def2TZVP (values in parentheses) level of theory. Geometries were optimized at B3LYP/6-31G(d) [with LANL2DZ for Pd,I].

References

[1] KEAVENEY ST, SCHOENEBECK F.
Angew. Chem. Int. Ed. 2018;57:4073-4077.
b) PU M, SANHUEZA IA, SENOL E, SCHOENEBECK F.
Angew. Chem. Int. Ed. 2018;57:15081-15085.

[2] SPERGER T, GUVEN S, SCHOENEBECK F.
Angew. Chem. Int. Ed. 2018;57:16903-16906.

[3] SCATTOLIN T, SENOL E, YIN G, GUO Q, SCHOENEBECK F.
Angew. Chem. Int. Ed. 2018;57:12425-12429.

[4] DIEHL CJ, SCATTOLIN T, ENGLERT U, SCHOENEBECK F.
Angew. Chem. Int. Ed. 2018;58:211-215.

Publications

[1] DIEHL CJ, SCATTOLIN T, ENGLERT U, SCHOENEBECK F.
C-I Selective Cross-Coupling Enabled by a Cationic Pd Trimer.
Angew. Chem. Int. Ed. 2019;58:211. [selected as very important paper (VIP)]

[2] SPERGER T, GUVEN S, SCHOENEBECK F.
Chemoselective Pd-Catalyzed C-TeCF3 Coupling of Aryl Iodides.
Angew. Chem. Int. Ed. 2018;57:16903. [selected as very important paper (VIP)]

[3] PU M, SANHUEZA IA, SENOL E, SCHOENEBECK F.
Divergent Reactivity of Stannane and Silane in the Trifluoromethylation of Pd(II): Cyclic Transition State versus Difluorocarbene Release.
Angew. Chem. Int. Ed. 2018;57:15081. [selected as very important paper (VIP)]

[4] SCATTOLIN T, SENOL E, YIN G, GUO Q, SCHOENEBECK F.
Site-Selective C-S Bond Formation at C-Br over C-OTf and C-Cl Enabled by an Air-Stable, Easy-to-Recover & Recyclable Pd(I) Catalyst. Angew. Chem. Int. Ed. 2018;57:12425.

[5] YE J, KALVET I, SCHOENEBECK F, ROVIS T.
Direct α-alkylation of primary aliphatic amines enabled by CO2 and electrostatics.
Nature Chem. 2018;10:1037.

[6] KEAVENEY ST, SCHOENEBECK F.
Palladium-Catalyzed Decarbonylative Trifluoromethylation of Acid Fluorides.
Angew. Chem. Int. Ed. 2018;57:4073. [selected as very important paper (VIP)]

[7] BOSHKOW J, SCATTOLIN T, SCHOENEBECK F.
Carreira EM. [1,3]-Sigmatropic Shift of an Allylic Chloride.
Helv. Chim. Acta 2018;101:e18001.

Selected honors

- Steinhofer Lectureship, University of Freiburg, 2018

Selected conference participations

- Lecture at University of Cologne, Germany, January 2018
- Lecture at Universität Heidelberg, Germany, January 2018
- Lecture at Dechema, Frankfurt, Germany, January 2018
- Lecture at Goethe-Universität Frankfurt, Germany, February 2018
- Lecture at Universität Freiburg, Germany, April 2018
- 'Journées de la Catalyse de Paris Saclay', Gif-sur-Yvette, France, April 2018
- 2nd International Symposium on Organic Reaction Mechanisms, China, May 2018
- Computational Catalysis for Sustainable Chemistry, Tarragona, Spain, June 2018)
- 16th Belgian Organic Synthesis Symposium (BOSS XVI), Belgium, July 2018
- Institutional Lectureship, Syngenta, UK, August 2018
- Symposium 'Physical-Organic Chemistry at its Best', Halle, Germany, September 2018
- 8th annual Organic Chemistry Symposium, Madrid, Spain, October 2018
- Lecture at TU Munich, Germany, November 2018
- Lecture at University of Vienna, Austria, November 2018

National and international cooperations

- Rovis, Columbia University, NY, USA
- Carreira, ETH Zürich, Switzerland

Chemical Solid State and Surface Research | DFG 302

Quantum chemistry of functional chalcogenide for phase-change memories and other applications

Project ID: jara0033
PHILIPP KONZE
RALF STOFFEL
RICHARD DRONSKOWSKI
Chair of Solid-State and Quantum Chemistry and JARA-HPC, Institute of Inorganic Chemistry, RWTH Aachen University

This project deals with **chalcogenide functional materials for storage-class memory**. We utilize large-scale atomistic simulations based on density-functional theory (DFT) to model stabilities of solids and surfaces, investigate electronic properties, and perform chemical-bonding analysis. From the calculation of pristine surfaces, to surface oxidation, and ligand-covered terminations, this project has matured to include new concepts to understand the electronic properties of phase-change materials (PCMs) and to introduce new materials for future applications. Furthermore, this project keeps making important contributions to the collaborative research center CRC 917 “Nanoswitches”.

Notwithstanding these ambitious goals, our project is necessary grounded on fundamental research, some of which is reported here. We have been studying **electronic properties of pseudochalcogenide compounds containing the carbodiimide ion NCN^{2-}** [1,2]. New ternary post-transition metal carbodiimides were recently synthesized and characterized in our group. Our calculations helped to interpret powder X-ray diffraction data and understand the chemical bonding situation in these compounds, highlighting similarities in the bonding situation, despite different coordination polyhedra.

Also, DFT studies in the pseudo-binary chalcogenide systems GeTe–GeSe and Sb_2Te_3–Sb_2Se_3 have been carried out (see Manuscripts in preparation), corroborating experimental high-pressure structures and heat capacities. The latter were calculated in the framework of the quasi-harmonic approximation. The influence of 2D defects on properties of PCMs was investigated for prototype materials such as In_2Se_3 and Sb_2Te_3.

Publications during the current accounting period

[1] CORKETT AJ, KONZE PM, DRONSKOWSKI R.
Synthesis, Crystal Structure, and Chemical-Bonding Analysis of $BaZn(NCN)_2$.
Inorganics. 2017;6:1.
[2] CORKETT AJ, KONZE PM, DRONSKOWSKI R.
The Ternary Post-transition Metal Carbodiimide $SrZn(NCN)_2$.
Z. Anorg. Allg. Chem. 2017;643:1456–1461.

Manuscripts in preparation

Four additional manuscripts, which are based on data obtained during the present accounting period, are in preparation or have been submitted to a journal. **First**, we investigated the phases of In_2Se_3 using chemical-bonding analysis [3].

In the **second** submitted project we used ab initio thermochemistry to obtain the theoretical heat capacities of several compositions in the $Sb_2Te_{3-x}Se_x$ solid solution which were in excellent agreement with experimentally measured data [4].
Furthermore, an investigation of the impact of 2D defects on optical and electrical properties of PCMs is being finalized in cooperation with electron microscopy data [5]. Finally, we carried out density-functional theoretical calculations to support high-pressure studies on the crystal structures of several compounds in the Ge-Se_xTe_{1-x} system [6].

[3] KÜPERS M, KONZE PM, MELEDIN A, WUTTIG M, MAYER J, ENGLERT U, DRONSKOWSKI R.
Controlled crystal growth of indium selenide, In_2Se_3, and the crystal structures of α-In_2Se_3, submitted to Inorg. Chem. 2018.
[4] HERRMANN MG, STOFFEL RP, DRONSKOWSKI R, FRIESE K.
The low-temperature heat capacity of the $Sb_2Te_{3-x}Se_x$ solid solution from experiment and theory, submitted to J. Phys. Cond. Matt. 2018.
[5] MIO AM, MELEDIN A, KONZE PM, KÜPERS M, POHLMAN M, KAMINSKI M, JOST P, DRONSKOWSKI R, MAYER J, WUTTIG M.
Impact of Bonding on the Stacking Defects in Chalcogenides, in preparation 2018.
[6] HERRMANN MG, KÜPERS M, STOFFEL RP, AIT HADDOUCH M, EICH A, GLAZYRIN A, GRZECHNIK A, DRONSKOWSKI R, FRIESE K.
New insights on the $GeSe_xTe_{1-x}$ phase diagram from theory and practice, in preparation 2018.

Additional publications

[1] KONZE PM, DRONSKOWSKI R, DERINGER VL.
Phys. Status Solidi RRL. 2019;13:1800579.
[2] HERRMANN MG, STOFFEL RP, KÜPERS M, AIT HADDOUCH M, EICH A, GLAZYRIN K, GRZECHNIK A, DRONSKOWSKI R, FRIESE K. Acta Crystallogr., Sect. B. 2019;75:246.
[3] KÜPERS M, KONZE PM, MELEDIN A, WUTTIG M, MAYER J, ENGLERT U, DRONSKOWSKI R. Inorg. Chem. 2018;57:11775.
[4] HERRMANN MG, STOFFEL RP, DRONSKOWSKI R, FRIESE K. J. Phys. Cond. Matt. 2018;30:405702.
[5] MÖLLER A, KONZE PM, DRONSKOWSKI R. Z. Anorg. Allg. Chem. 2018;644:1881.
[6] CORKETT AJ, KONZE PM, DRONSKOWSKI R. Inorganics. 2017;6:1.
[7] CORKETT AJ, KONZE PM, DRONSKOWSKI R. Z. Anorg. Allg. Chem. 2017;643:1456.
[8] SCHÄFER T, KONZE PM, HUYENG JD, DERINGER VL, LESIEUR T, MÜLLER P, MORGENSTERN M, DRONSKOWSKI R, WUTTIG M.
Chem. Mater. 2017;29:6749.
[9] KÜPERS M, KONZE PM, MAINTZ S, STEINBERG S, MIO AM, COJOCARU-MIRÉDIN O, ZHU M, MÜLLER M, LUYSBERG M, MAYER J, WUTTIG M, DRONSKOWSKI R.
Angew. Chem. Int. Ed. 2017;56:10204.
[10] DERINGER VL, DRONSKOWSKI R. J. Phys. Chem. C. 2016;120:8813.
[11] KONZE PM, DERINGER VL, DRONSKOWSKI R. Chem. Mater. 2016;28:6682.
[12] DERINGER VL, DRONSKOWSKI R. Angew. Chem. Int. Ed. 2015;54:15334.
[13] STOFFEL RP, DERINGER VL, SIMON RE, HERMANN RP, DRONSKOWSKI R.
J. Phys.: Condens. Matter. 2015;27:085402.
[14] DERINGER VL, STOFFEL RP, WUTTIG M, DRONSKOWSKI R.
Chem. Sci. 2015;6:5255.
[15] DERINGER VL, DRONSKOWSKI R. J. Appl. Phys. 2014;116:173703.
[16] DERINGER VL, DRONSKOWSKI R. Chem. Sci. 2014;5:894.
[17] DERINGER VL, DRONSKOWSKI R. ChemPhysChem. 2013;14:3108.
[18] DERINGER VL, DRONSKOWSKI R. J. Phys. Chem. C. 2013;117:24455.

Selected conference participations related to this project:

- MRS Fall Meeting: „Solid-State Chemistry of Inorganic Materials”, Boston, MA, USA, November 25-30, 2018

Selected national and international cooperations related to this project:

- VOLKER L. DERINGER, Department of Engineering, University of Cambridge, UK
- MIN ZHU, Shanghai Institute of Micro-System and Information Technology, Chinese Academy of Sciences, Shanghai, China
- MATTHIAS WUTTIG, I. Institute of Physics (IA), RWTH Aachen University

Quantum chemistry and structural exploration of crystalline molecular networks

Project ID: jara0069
DAMIAN MROZ
JANINE GEORGE
RICHARD DRONSKOWSKI
Chair of Solid-State and Quantum Chemistry and JARA-HPC, Institute of Inorganic Chemistry, RWTH Aachen University

In this project, we explore molecular crystals and especially their electronic and phononic properties by electronic-structure theory.

We continued our work on thermal motion and the calculation of ab initio anisotropic displacement parameters (ADPs) [1-3]. We showed that calculating ADPs in the quasi-harmonic approximation (inclusion of volume expansion) leads to reliable ADPs up to at least 200 K for very different molecular crystals (urea, bromomalonic aldehyde, pentachloropyridine, and naphthalene; see Figure 1). In one case, the ADPs were even in good agreement up to room temperature. Furthermore, the influence of normal-mode anharmonicity on ADPs of molecular crystals was tested for the first time [1]. It could be shown that the frequent overestimation of the ADPs in the quasi-harmonic approximation can (at least in part) be explained by neglecting anharmonicity, which lowers the values of the calculated ADPs.

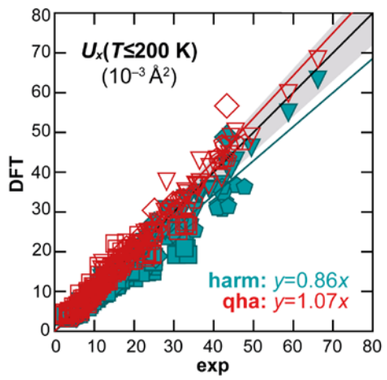

Figure 1. Comparision of calculated ADPs in the harmonic (harm) and quasi-harmonic approximation (qha) with experimental data for urea, bromomalonic aldehyde, pentachloropyridine, and naphthalene (Adjusted from [1]).

Furthermore, calculated ADPs served as fixed numerical entries in the Rietveld refinement of neutron powder diffraction data of $[CH_4ClN_2][AuCl_4]$ – a chloro formamidinium salt [2]. This helped to better handle the strong absorption of gold and the incoherent scattering of hydrogen, and it improved the data-to-parameter ratio in the refinement so that the hydrogen positions could be refined freely. Additionally, the very first full structural characterization of chloro formamidinium salts was complemented with ab initio electronic band structures and densities of states confirming the ionic nature of the compounds (see Figure 2) [2].

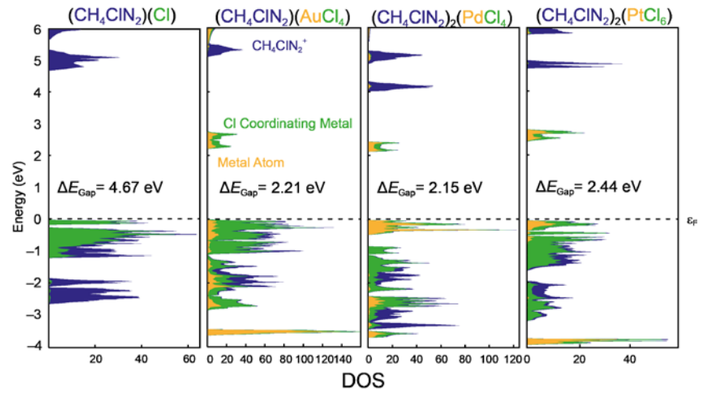

Figure 2. Local DOS for four different chloro formamidinium salts. The local DOS of the metal atoms is shown in yellow, the one of the coordinating chlorine atoms in green, and the one of the cationic atoms in blue. This figure is taken from [2].

Publications in peer-reviewed journals:

[1] CORKETT AJ, KONZE PM, DRONSKOWSKI R.
GEORGE J, WANG R, ENGLERT U, DRONSKOWSKI R.
Lattice thermal expansion and anisotropic displacements in urea, bromomalonic aldehyde, pentachloropyridine, and naphthalene. J. Chem. Phys. 2017;147:074112.

[2] MÖLLER A, GEORGE J, DRONSKOWSKI R.
First Full Structural Characterization of Chloro Formamidinium Salts.
Z. Anorg. Allg. Chem. 2018. DOI: 10.1002/zaac.201800164.

All publications were in collaboration with experimentalists.

Other publications

[3] GEORGE J.
Dichtefunktionaltheoretische Betrachtungen intermolekularer Wechselwirkungen und thermischer Bewegung in Molekülkristallen und metallorganischen Verbindungen. Dissertation. RWTH Aachen University. 2017.

Selected honors

- Borchers Badge for JANINE GEORGE (2018)
  (Award for Doctorate with Distinction (summa cum laude))

Selected conference participations

- Ab Initio Anisotropic Displacement Parameters of Molecular Crystals, Contributed Talk at the Symposium on Theoretical Chemistry in Halle (Saale), Germany, September 2018.
- How Computational Chemistry Can Help Crystallographers and Practical Chemists, Invited Academic Talk at the 3rd Meeting of the German Young Crystallographers in Aachen, Germany, September 2018.

Selected national and international cooperations

- Cooperation with Englert, Institute of Inorganic Chemistry, RWTH Aachen University
- Cooperation with Dr. George, Institute of Condensed Matter and Nanoscience, Université Catholique de Louvain, Belgium

Ionic conductivity of Gd-doped ceria from molecular dynamics simulations

Project ID: rwth0273
STEFFEN GRIESHAMMER
Chair of Physical Chemistry I
and Institute of Physical Chemistry,
RWTH Aachen University

In this project, ionic conductivity of Gd-doped ceria was simulated, using molecular dynamics (MD) and kinetic Monte Carlo (KMC) methods, to investigate the influence of doping fraction and temperature.

In MD simulations, all lattice dynamics are captured, which are important for oxygen ion conductivity; however, the simulated time span is limited to a few nanoseconds. In the KMC simulations, the individual vibrations are disregarded and the hopping rates of defects are parametrized resulting in faster simulations and the possibility to simulate longer time spans.

MD simulations were performed with the program package LAMMPS[1] based on the empirical pair potentials (EPP) according to Pedone et al.[2] Simulations were performed for temperatures between 1200 and 1500 K with dopant fractions of x=0.05 to 0.3 in $Ce_{1-x}Gd_xO2_{-x/2}$ in a simulation box of 14x14x14 unit cells. An electric field of 0.5 MV/cm was applied to obtain the ionic conductivity from the displacement of oxygen ions.

KMC simulations were performed with the in-house software iCon.[3] For the parametrization of the individual hopping rates, migration energies for different defect environments were calculated with the GULP[4] code. Resulting conductivities from MD simulations are shown in Figure 1. The conductivity increases with increasing dopant fraction. At lower temperatures a maximum in the conductivity is observed at intermediate doping fractions as found in experiments. The KMC simulations showed the same trend for the conductivity but with a slightly more pronounced maximum implying that the defect interactions were overestimate in these simulations.

Publications

[1] PLIMPTON S. J. Comp. Phys. 1995;117:1-19.
[2] PEDONE A, et al. J. Phy. Chem. B. 2006;110:11780-11795.
[3] http://icon.pc.rwth-aachen.de/
[4] GALE J. Faraday Trans. 1997;93:629-637.

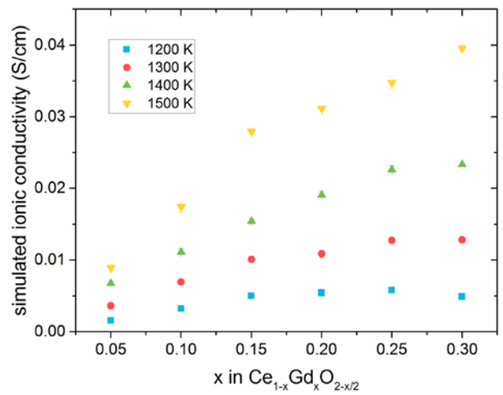

Figure 1: Simulated ionic conductivity depending on the dopaing level.

Investigation of the new materials for safe management of high level nuclear waste

Project ID: jara0037, jara0038, jiek61
PIOTR KOWALSKI
Institute of Energy and Climate Research:
Nuclear Waste Management
and Reactor Safety (IEK-6),
FZ Jülich

Short descriptions of these projects:
The safe disposal of (high-level) radioactive wastes, including spent nuclear fuels, requires a solid scientific basis that can help to reliably assess the long-term performance of the waste materials in a deep geological repository. Spent nuclear fuels and reprocessing wastes contain actinides and long-lived fission and activation products, which can remain radioactive for hundreds of thousands of years. The isolation of these elements from the biosphere for up to one million years is a key aspect of the planned deep geological disposal. The ongoing multidisciplinary research covers various aspects of the performance of deep geological repositories and focuses on, but is not limited to, the performance of spent nuclear fuels, the durability of waste forms and waste containers, and the radionuclide interaction with the surrounding host rocks and cementitious materials used in the construction of the reposity. Due to the complex chemistry of radioactive compounds, the thermodynamic and physical properties of many An-bearing materials are poorly understood. In our institute we synthesize different radionuclide-containing materials and perform systematic analysis of their structural, chemical, physical and thermodynamic properties. The challenge is to understand changes in structural and thermodynamic properties of these materials due to incorporation of different radioactive elements and the thermodynamic properties of secondary minerals that form due to the reactions between a corroded waste form, ground water and the host rocks. This research benefits from HPC-aided simulations, which permit a unique atomic-scale insight into the outlined processes and provide important data which are difficult to measure due to the radiotoxicity of investigated materials. The aim of currently ongoing JARA-HPC projects is: (i) to characterize the structural and thermodynamic properties of ceramics nuclear waste forms and spent nuclear fuel, (ii) to understand the underlying reasons for selective extraction of radionuclides by organic extraction ligands (e.g. diglycolamide mTDDGA), (iii) to understand retention of radionuclides by different cementitious materials and secondary mineral phases and (iv) to understand the atomic scale properties of irradiated borosilicate glasses. We succeeded in setting up accurate and feasible computational methodologies which provide results of accuracy comparable to the experiments and allow for joint modeling and experimental activities. The already finalized projects allowed us, among others, to explain the variation of elastic and heat transfer properties in different ceramic compounds, to derive the excess thermodynamic parameters of monazite-type (La_1-x(Ln,An)$_x$$PO_4$) and barite-type solid solutions ((Ba,Sr,Ra)SO_4), to understand different selectivity of distereomers of double methylated TODGA organic extractant, to construct phase diagrams of various actinide-bearing compounds and to understand the capability of different materials to retard radionuclides.

Publications

[1] MURPHY G, WANG CHH, ZHANG Z, KOWALSKI PM, BERIDZE G, AVDEEV M, MURANSKY O, BRAND H, GU Q, KENNEDY B.
Controlling Oxygen Defect Formation and its Effect on Reversible Symmetry Lowering and Disorder-to-Order Phase Transformations in Non-Stoichiometric Ternary Uranium Oxides. Inorganic Chemistry. 2019;58:6143-6154.
[2] JI Y, MARKS NA, BOSBACH D, KOWALSKI PM.
Elastic and thermal parameters of lanthanide-orthophosphate ($LnPO_4$) ceramics from atomistic simulations. Journal of European Ceramic Society. 2019;39:4264.

[3] DANIELS N, FRANZEN C, MURPHY GL, KVASHNINA K, PETROV V, TORAPAVA N, BUKAEMSKIY A, KOWALSKI PM, SI H, JI Y, HÖLZER A, WALTHER C. Application of Layered Double Hydroxides for ^{99}Tc Remediation. Applied Clay Science. 2019;176:1.

[4] WILDEN A, KOWALSKI PM, KLASS L, KRAUS B, KREFT F, MODOLO G, LI Y, ROTHE J, DARDENNE K, GEIST A, LEONCINI A, HUSKENS J, VERBOOM W. Unique Difference and Unprecedented Inversion of Selectivity in the Complexation of Trivalent f-Elements by Different Diastereomers of a Modified Diglycolamide. Chemistry- European Journal. 2019;25:5507.

[5] JI Y, KOWALSKI PM, KEGLER P, HUITTINEN N, MARKS N, VINOGRAD VL, ARINICHEVA Y, NEUMEIER S, BOSBACH D. Rare-Earth orthophosphates from atomistic simulations. Frontiers in Chemistry 7. 2019;197. (invited).

[6] KVASHNINA K, KOWALSKI PM, BUTORIN S, LEINDERS G, PAKARINEN J, BES R, LI H, VERWERF M. Trends in valence band electronic structure of mixed uranium oxides. submitted to Chemical Communications 54. 2018;9757.

[7] LANGE S, KOWALSKI PM, PŠENIČKA M, KLINKENBERG M, ROHMEN S, BOSBACH D, DEISSMANN G. Uptake of ^{226}Ra in cementitious systems: A complementary solution chemistry and atomistic simulation study. Applied Geochemistry. 2018;96:204.

[8] HUITTINEN N, SCHEINOST AC, JI Y, KOWALSKI PM, ARINICHEVA Y, WILDEN A, NEUMEIER S, STUMPF T. A spectroscopic and computational study of Cm^{3+} incorporation in lanthanide phosphate rhabdophane ($LnPO_4 \times 0.67\ H_2O$) and monazite ($LnPO_4$). Inorganic Chemistry. 2018;57:6252.

[9] MURPHY GL, WANG CHH, BERIDZE G, ZHANG Z, KIMPTON JA, AVDEEV M, KOWALSKI PM, KENNEDY BJ. An Unexpected Crystallographic Phase Transformation in Non-Stoichiometric $SrUO_{4-x}$: Reversible Oxygen Defect Ordering and Symmetry Lowering with Increasing Temperature. Inorganic Chemistry. 2018;57:5948–5958.

[10] VITOVA T, PIDCHENKO I, BISWAS S, BERIDZE G, DUNNE PW, SCHILD D, WANG Z, KOWALSKI PM, BAKER RJ. Dehydration of the Uranyl Peroxide Studtite, $[UO_2(\eta^2\text{-}O_2)(H_2O)_2]\cdot 2H_2O$, Affords a Drastic Change in the Electronic Structure: A Combined X-ray Spectroscopic and Theoretical Analysis. Inorg. Chem. 2018;57:1735.

[11] LI Y, KOWALSKI PM. Energetics of defects formation and oxygen migration in pyrochlore compounds. Journal of Nuclear Materials. 2018;505:255.

Selected honors

- World-wide highlight: Murphy et al. “Reversible Oxygen Defect Ordering and Symmetry Lowering with Increasing Temperature”, Inorganic Chemistry 57, 5948–5958 (2018) (https://phys.org/news/2018-08-uranium-disorder.html)

Selected conference participations

- MRS2018 Fall Meeting and Exhibit “Uptake of Ra and Eu in cementitious systems by joint solution chemistry and atomistic modeling studies”, Boston, USA, November 25-30, 2018

National and international cooperations

- Understanding electronic structure of mixed-uranium oxides, European Synchrotron Radiation Facility/HZDR (Kristina Kvashnina)
- Modeling of irradiated boro-silicate glasses: Lanzhou University, China (Tieshan Wang)
- Modeling of U-bearing secondary phases materials, ceramics and irradiated graphite: ANSTO/U. of Sydney (Zhaoming Wang, Berndan Kennedy)
- Uptake of radionuclides by secondary phases, Trinity College, Ireland (Robert Baker)
- Modeling of thermal conductivity: Curtin U., Australia (Nigel Marks)

Quantum-Chemical Density Functional Theory- and Ab Initio Calculations on Salvarsan $(3\text{-}NH_2\text{-}4\text{-}HOC_6H_3As)_n$ (n=1-6)

Project ID: rwth0219
GERHARD RAABE
Institute of Organic Chemistry,
RWTH Aachen University

DAMIAN PATRICK MROZ
Chair of Solid-State and Quantum Chemistry,
RWTH Aachen University

YUEKUI WANG,
Key Laoratory of Chemical Biology and Molecular Engineering
of the Education Ministry,
Shanxi University, Taiyuan, China

DIETER AN MEY
IT Center,
RWTH Aachen University

Although discovered more than 100 years ago by Paul Ehrlich the structure of Salvarsan $(3\text{-}NH_2\text{-}4\text{-}HOC_6H_3As)_n$, the first synthetic drug active against Treponema pallidum, a bacterium causing Lues (Syphilis), remains widely unknown. ESI masspectrometry was employed by other authors1 to elucidate the structure, and it turned out that in aqueous solution the compound exists most likely as a mixture of cyclic oligomers with n=3 and n=5 (Chart 1) as the leading components. It is the aim of this study elucidate the structure of the compound by quantum- chemical computational methods.

At the highest level of theory employed in this study (CCSD/6-31++G**//CCSD(T)/6-311++G**) the ground state of the monomer (1) turned out to be the lowest triplet state with the lowest singlet about 20kcal/mol higher in energy. This value is somewhat lower than the one obtained for arsinidene (HAs) of 29kcal/mol.

Due to the high flexibility especially of the oligomers with n≥4 the geometry optimizations and normal mode analyses for the compounds with n>1 were performed at the density functional theory level (DFT), employing the B3LYP and the CAM-B3LYP functionals and the 6-311+G** basis set. With both functionals the ground states of the oligomers with n≥2 turned out to be the lowest singlet states with an increasing singlet-triplet gap (ΔEST) from about 20kcal/mol (n=2) to more than 30kcal/mol for n=6.

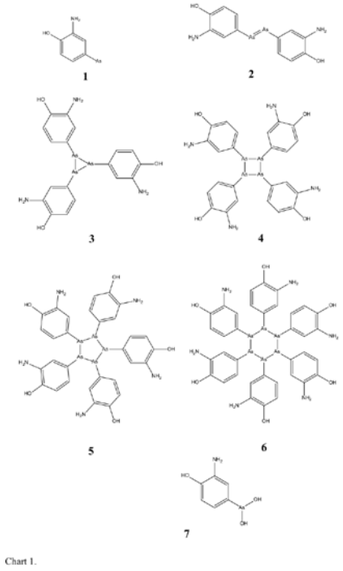

Chart 1.

The incremental energy of oligomerisation (energy of oligomerization/n; where the energy of oligomerization is the total energy of the corresponding oligomer minus n-times the total energy of the monomer in its lowest triplet state) is the least negative for n=2 (B3LYP: - 29, CAM-B3LYP: -28kcal/mol) while with both functionals values between -35 and -37kcal/mol were obtained for n=3-6.

The planned calculations to elucidate the structure of the physiologically active compound, which is most likely different from the oligomers, and to obtain the UV/VIS (ultra violet/visible) and ECD (electronic circular dichroism) spectra could not be finished so far.

National and international co-operations

- Yuekui Wang/Key Laoratory of Chemical Biology and Molecular Engineering of the Education Ministry, Shanxi University, Taiyuan, China
- Dieter an Mey, IT Center, RWTH Aachen University

References:

(1) The composition of Ehrlich's salvarsan: resolution of a century-old debate. Lloyd NC, Morgan HW, Nicholson BK, Ronimus RS. Angew Chem Int Ed Engl. 44(6):941-4 (2005).

Development of a Composition-Structure-Property-Map for the Examples of Ternary, Te-rich Tellurides

Project ID: jara0167
SIMON STEINBERG
Institute of Inorganic Chemistry,
RWTH Aachen University

Scientific work accomplished and results obtained

Materials comprising low-dimensional building units in their crystal structures are alluring systems to explore the formations of Charge Density Waves (CDWs)[1,2] which are periodic modulations of the conducting electron density and related to electronically unfavorable situations.[3] To overcome such unfavorable states by decreasing the electronic energy relative to that of the metallic state, a gap corresponding to a periodic lattice distortion below a certain transition temperature typically opens at the Fermi level.[3,4] The suppressions of the formations of CDWs in low-dimensional building units are crucial for the accomplishments of superconducting states.[5] In the lack of full knowledge of procedures to predict the formations of CDWs in low-dimensional building units, there is a critical need to develop schemes to forecast electronic instabilities in materials with low-dimensional fragments in their crystal structures.

Because the binary and ternary tellurium-rich tellurides often comprise low- dimensional building units, for which some have been reported to undergo structural distortions because of CDW formations,[6-9] this class of materials is predestinated to serve as model system to investigate the influence of the valence electron counts on the occurrence and absence of CDWs in a series of isostructural compounds with dissimilar compositions. In this context, the development of a composition-structure-property-map for the Te-rich tellurides that is the overall goal of this project will facilitate to develop a global procedure for the predictions of electronically unfavorable situations in materials with low-dimensional building units.

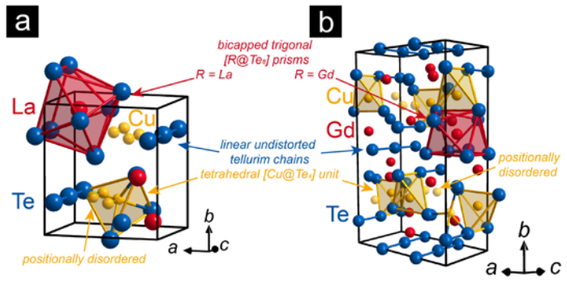

Figure 1: Representations of the crystal structures of (a) $LaCu_xTe_2$ ($0.28 \leq x \leq 0.50$) and (b) $Gd_3Cu_2Te_7$

To understand the origin of the occurrence or absence of structural distortions in low- dimensional tellurium fragments, examinations of the electronic structures and chemical bonding analyses were carried out for the ternary $LaCu_xTe^2$ ($0.28 \leq x \leq 0.50$) and $Gd_3Cu_2Te_7$. Because the low-dimensional tellurium building units often undergo structural distortions because of the formations of CDWs,[1] it is remarkable that the crystal structures of the ternary tellurium-rich $LaCu_xTe_2$ ($0.28 \leq x \leq 0.50$)[10-12] and $Gd_3Cu_2Te_7$[13] both comprise one-dimensional undistorted tellurium chains (Figure 1). In the case of the lanthanum-containing species, inspections of the temperature-dependent electrical resistivity behavior revealed that this telluride should be a semiconductor.[11,12] Because the crystal structures of both tellurides contain disordered copper positions, diverse models approximating the actual crystal structures were developed. The structure models that corresponded to the lowest total energies among the diverse inspected models were expected to be the most favorable to be compared to the experimentally determined model[14] and, hence, were chosen for the examinations of the electronic structures and chemical bonding analyses.

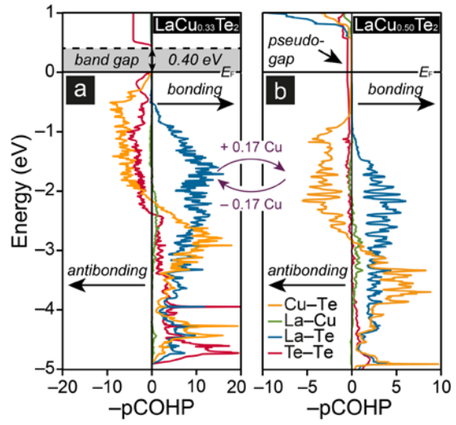

Figure 2. –pCOHP curves of (a) a $LaCu_{0.33}Te_2$ model and (b) a $LaCu_{0.50}Te_2$ model; the Fermi level, EF, is represented by the black horizontal line.

The chemical bonding analyses were accomplished based on the **p**rojected **c**rystal **o**rbital **H**amilton **p**opulation (pCOHP) curves and their respective integrated values and revealed that the majority of the bonding interactions resides between the rare–earth–tellurium contacts (Figure 2). Furthermore, the tellurium–tellurium and copper–tellurium interactions play a minor, but evident role in the overall bonding. In particular, a gedankenexperiment, in which the amount of copper atoms is reduced going from a $LaCu_{0.50}Te_2$ model to a $LaCu_{0.33}Te_2$ model, shows that a gap opens at the Fermi level and that the tellurium chains slightly distort thereby providing more bonding tellurium–tellurium interactions relative to the copper–tellurium interactions in order to optimize overall bonding. The outcome of this quantum chemical investigations implies to determine crystal structures of these ternary tellurides for lower temperatures and copper contents in order to detect the projected distortions within the one-dimensional linear tellurium chains.

To project electronic instabilities as origins of electronically unfavorable situations in materials with low-dimensional building units, it will be beneficial to develop a search tool for detections of such instabilities in the course of high-throughput screenings of compound libraries utilizing quantum chemical techniques. One class of compounds being typically expected to show electronic instabilities at the Fermi levels are superconductors. In particular, the structural instabilities induced by electrons residing in flat bands at the Fermi levels of superconductors are expected to be counterbalanced by electrons from steep bands such that distortions of the structures are hindered according to the steep band/flat band scenario[15,16]. To probe the reliabilities of a projected descriptor and a quantum chemical code which should be used for the high-throughput screenings of the compound libraries for electronic instabilities originating from the occupations of flat bands at the Fermi levels, we examined the electronic band structures of a series of chalcogenide superconductors for the occurrence of occupied flat bands at the Fermi levels. The survey of the features at the Fermi levels in the chalcogenide superconductors demonstrates that occupied flat bands in the forms of van Hove singularities[17] are evident at the Fermi levels for 57% and close to the Fermi levels for 91% of the investigated superconductors. The apparent discrepancy between the presence of superconductivity and the locations of the van Hove singularities close to the Fermi levels can be explained based on the presence of vacancies in the crystal structures of the chalcogenides which influence the relative positions of the singularities.

Realization of the project

All structural optimizations, including lattice parameters and atomic positions, and electronic band structure calculations for the diverse chalcogenides presented in the section **2 Scientific work accomplished and results obtained** were performed with the

projector-augmented wave (PAW) method[18] as coded in the Vienna Ab initio Simulation package (VASP).[19-22] The coordinates of the k-paths within the first Brillouin zones of the diverse chalcogenides were generated using the AFLOW[23] code, while the electronic band structures were visualized utilizing the Python Materials Genomics (pymatgen)[24] program. Chemical bonding analyses for the structurally optimized rare-earth-copper-tellurides were achieved with the aid of the pCOHP technique[25] that is a variant of the crystal orbital Hamilton population (COHP)[26] procedure. Because the COHP method requires the employments of crystal orbitals derived from local basis sets, the Hamilton-weighted populations had to be projected from the plane-wave-based electronic structure computations with the aid of Local-Orbital Basis Suite Towards Electronic-Structure Reconstruction program[25-28] (LOBSTER). All plane-wave-based electronic structure computations were accomplished with the latest version of the VASP[19-22] code which is fully operating on the computer cluster of the IT Center at RWTH Aachen University and scales for up to 144 cores. We expect to use the granted compute time in total by the end of the period of the project.

Publications with project results

Publications in Journals with Peer-review Process

- GLADISCH FC, STEINBERG S.
  Revealing the Nature of Bonding in Rare-Earth Transition-Metal Tellurides by Means of Methods Based on First Principles. Eur. J. Inorg. Chem. 2017;2017:3395–3400.

Other Publications

- GLADISCH FC, STEINBERG S.
  Revealing the Kind of Bonding in Rare-earth Transition-metal Tellurides.
  Poster contribution to the GDCh Wissenschaftsforum Chemie conference in Berlin, Germany. September 2017.
- FRIES KS, STEINBERG S.
  Fermi-Level Characteristics of Potential Chalcogenide Superconductors.
  Chemistry of Materials. 2018;30:2251–2261.
- GÖBGEN KC, GLADISCH FC, STEINBERG S.
  The Mineral Stützite: a Zintl-Phase or Polar Intermetallic? A Case Study Using Experimental and Quantum-Chemical Techniques. Inorganic Chemistry. 2018;57:412–421.

Theses completed within the project

- FRIES KS.
  Examination of the Features at the Fermi level for Intermetallic Chalcogenide Superconductors, B. Sc. Thesis, RWTH Aachen University, Aachen, Germany, 2017.

Additional references

[1] SHELDRICK WS. Z. ANORG. Allg. Chem. 2012;638:2401-2424.
[2] PAPOIAN GA, HOFFMANN R. Angew. Chem. Int. Ed. 2000;39:2408-2448.
[3] GRÜNER G. Rev. Mod. Phys. 1988;60:1129-1181.
[4] CANADELL E, Whangbo MH. Chem. Rev. 1991;91:965-1034.
[5] MOROSAN E, ZANDBERGEN HW, DENNIS BS, BOS JWG, ONOSE Y, KLIMCZUK T, RAMIREZ AP, ONG NP, CAVA RJ. Nature Phys. 2006;2:544-550.
[6] MALLIAKAS CD, IAVARONE M, FEDOR J, KANATZIDIS MG. J. Am. Chem. Soc. 2008;130:3310-3312.
[7] MALLIAKAS CD, BILLINGE SJL, KIM HJ, KANATZIDIS MG. J. Am. Chem. Soc. 2005;127:6510-6511.
[8] MALLIAKAS CD, KANATZIDIS MG. J. Am. Chem. Soc. 2006;128:12612-12613.
[9] MALLIAKAS CD, KANATZIDIS MG. J. Am. Chem. Soc. 2009;131:6896-6897.
[10] DUNG NH, PARDO MP, BOY P. ACTA. Crystallogr, Sect. C. 1983;39:668-670.
[11] HUANG FQ, BRAZIS P, KANNEWURF CR, IBERS JA. J. Am. Chem. Soc. 2000;122:80- 86.
[12] PARDO MP, GARDETTE MF, FLAHAUT J. J. Solid State Chem. 1991;90:1-7.
[13] HUANG FQ, IBERS JA. J. Solid State Chem. 2001;159:186-190.
[14] GAUTIER R, ZHANG X, HU L, YU L, LIN Y, SUNDE TOL, CHON D, POEPPELMEIER KR, ZUNGER A. Nature Chem. 2015;7:308-316.
[15] SIMON A. Angew. Chem. Int. Ed. Engl. 1997;36:1788-1806.
[16] SIMON A. Solid State Sci. 2005;7:1451-1455.
[17] MARKIEWICZ RS. J. Phys. Chem. Solids. 1997;58:1179-1310.
[18] BLÖCHL PE. Phys. Rev. B. 1994;50:17953-17979.
[19] KRESSE G, HAFNER J. Phys. Rev. B. 1993;47:558-561.
[20] KRESSE G, FURTHMÜLLER J. Comput. Mater. Sci. 1996;6:15-50.
[21] KRESSE G, FURTHMÜLLER J. Phys. Rev. B. 1996;54:11169-11186.
[22] KRESSE G, MARSMAN M, FURTHMÜLLER, J. Vienna Ab-initio Simulation Package (VASP), the GUIDE University of Vienna. Vienna, Austria. 2010.
[23] SETYAWAN W, CURTAROLO S. Comput. Mater. Sci. 2010;49:299-312.
[24] ONG SP, RICHARDS WD, JAIN A, HAUTIER G, KOCHER M, CHOLIA S, GUNTER D, CHEVRIER VL, PERSSON KA, CEDER G. Comput. Mater. Sci. 2013;68:314-319.
[25] DERINGER VL, TCHOUGRÉEFF AL, DRONSKOWSKI R. J. Phys. Chem. A. 2011;115:5461- 5466.
[26] DRONSKOWSKI R, BLÖCHL PE. J. Phys. Chem. 1993;97:8617-8624.
[27] MAINTZ S, DERINGER VL, TCHOUGRÉEFF AL, DRONSKOWSKI R. J. Comput. Chem. 2013;34:2557-2567.
[28] MAINTZ S, DERINGER VL, TCHOUGRÉEFF AL, DRONSKOWSKI R. J. Comput. Chem. 2016;37:1030-1035.

Selected conference participations

- Revealing the Nature of Bonding in Polar Intermetallic Compounds, Chemiedozententagung, Jena, Germany, March 07, 2018
- Grenzgänger, Steinheimer Gespräche, Mainz, Germany, June 15, 2018

Physical and Theoretical Chemistry | DFG 303

Quantum Monte Carlo - A study of the Dissociation Energies of ZnO, FeO, FeH, and CrS

Project ID: rwth0278
ARNE LÜCHOW
Institute for Physical Chemistry,
RWTH Aachen University

The theoretical investigation of transition metal compounds is a highly interesting field of research, since the accurate description of those systems is of crucial importance when it comes to elucidating catalytic processes. The large non-dynamic correlation of transition metal compounds still poses a great challenge for high-level theoretical methods. While DFT is often inaccurate, traditional wave function methods can yield accurate results. They however usually suffer from a bad scaling with respect to the number of electrons and the number of CPUs and their accuracy strongly depends on the zeroth order wave function. The quantum Monte Carlo (QMC) approach offers an elegant way to tackle these problems due to its highly parallel regime. The variational (VMC) and diffusion (DMC) Monte Carlo methods are the most commonly used stochastic approaches when an accuracy beyond mean field theory is required. Wave function-based approaches, such as multi-reference CI (MRCI) and multi-reference perturbation theory (CASPT2) account for the non-dynamic correlation through an expansion in determinants. This technique is adopted in QMC, meaning that a linear combination of Slater determinants is employed together with a Jastrow correlation function in order to determine the properties of transition metal compounds.
In this project we computed the dissociation energies of NiC, FeC, ZnO, and CrS. The atomic spectrum of the Nickel atom was evaluated. The ground state as well as two excited states were computed. The energy gaps between different atomic states being experimentally accessible with a high accuracy, the efficiency of the employed approach can be assessed. The single determinant guide functions are not able to predict the correct ground state of Ni. When moving toward multi-reference guide functions and optimizing the orbitals in the presence of a Jastrow correlation function, DMC not only yields the correct ground state of Ni but it also provides very accurate excitation energies.

The carbide compounds need to be further investigated. The substantial amount of parameters that needed to be optimized with VMC proved rather challenging. In addition, we believe that the active space, constructed from the 4s and 3d orbitals of the metal and the 2p orbitals of carbon, is too small to accurately evaluate these systems. We computed a dissociation energy for NiC of 3.946(18) eV for the fully optimized guide function, compared to the experimental one of Matthew et al.[1], which corresponds to 4.167(3) eV. For FeC, only the Jastrow and CI parameters were optimized. The dissociation energy, obtained for this guide function, amounts to 3.451(29) eV. Matthew et al.[1] reported a dissociation energy of 3.961(19) eV for this compound.

As for the remaining two compounds, we were able obtain an excellent agreement with experimental dissociation energies when employing multi-reference DMC (MR-DMC) guide functions. The key role is thereby ascribable to the optimization of the molecular orbitals in the presence of a Jastrow factor with VMC. The results have been submitted to J. Chem. Theory Comput. and are currently under review. They will also be presented at the 10th Triennial Congress of the International Society for Theoretical Chemical Physics. We have shown in that work that it is possible to compute accurate properties, such as the dissociation energy, the harmonic frequency, and the anharmonicity, for the investigated compounds when compact wave functions generated from a small, physically motivated CAS are used.

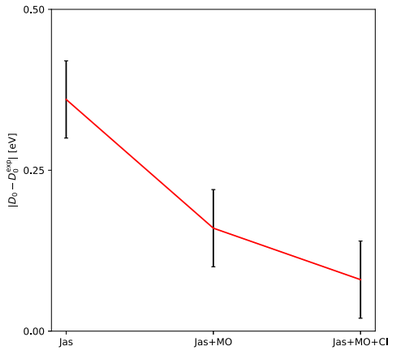

Figure 1: Systematic reduction of the deviation of the computed MR-DMC dissociation energies to the experimental one at various optimization levels.

References

[1] MATTHEW DJ, TIEU E, MORSE MD.
Determination of the bond dissociation energies of FeX and NiX (X = C, S, Se). J. Chem. Phys. 2017;146:144310.

Publications

- LUDOVICY J, HAGHIGHI MOOD K, LÜCHOW A.
  Revision under review in J. Chem. Theory Comput.

Condensed Matter Physics | DFG 307

Theoretical investigation of spin and charge dynamics in nanostructures

Project ID: jara0175
FILIPE S. M. GUIMARÃES
Peter Grünberg Institut and Institute for Advanced Simulation (PGI-1 / IAS-1)
FZ Jülich & JARA

JENS RENÉ SUCKERT
Peter Grünberg Institut and Institute for Advanced Simulation (PGI-1 / IAS-1)
FZ Jülich & JARA

Scientific work accomplished and results obtained

Magnetization dynamics is a highly important topic when dealing with magnetic manipulation. The time-dependence of a magnetic moment is frequently described by the phenomenological Landau-Lifshitz-Gilbert equation [2]

$$\frac{dM}{dt} = -\gamma M \times B + \frac{\alpha}{M} M \times \frac{dM}{dt} \qquad (1)$$

where $\gamma > 0$ is the gyromagnetic factor, M is the (spin) magnetic moment, B is the time- dependent effective magnetic field acting on M, and α is a scalar damping parameter, known as Gilbert damping. The first term on the right-hand side of Eq. (1) describes the torques that set the magnetization into motion, while the second term represents relaxation effects pushing M to the equilibrium direction.

This semi-classical description, however, depends on external parameters such as the renormalized γ, α, as well as the anisotropy fields and eventual couplings between different magnetic units included in the effective field B. Many proposals have been made on how the material-dependent values can be obtained from first principles calculations. In particular, there are many approaches to obtain the Gilbert damping [3–6]. The connections between the different methods and their range of validity were not clear.

With the new implementations made during the past year on TITAN (Time-dependent Transport and Angular momentum in Nanostructures), we embraced the task of implementing all the well-known formulas to calculate α. Since TITAN is based on the electronic structure of the system, it is an ideal code to investigate the intrinsic effects and mechanisms involved in the relaxation process. It also gives a unique framework to treat all the approaches on equal footing. These calculations were also used to test and benchmark the new implementations (described below). Further details on the analytical and numerical results obtained within this investigation can be found in the pre-print arXiv:1807.11808 [cond-mat.mes-hall], which will soon be submitted to publication in a high impact journal [1].

Further calculations to investigate the impact of higher order contributions to the magnetization dynamics (such as moment of inertia) and the spin pumping mechanism are planned for the near future.

Realization of the project

The project schedule was fulfilled almost entirely. The only missing item was the re-implementation of the currents in the new basis format. This occurred because we decided to focus on Fe, Ni and Co bulk and monolayer structures for the calculation of the Gilbert damping (described in the section above). The planned implementation of the energy-dependent mesh and the concurrent modification of the parallelization scheme highly optimized the code, which enabled us to investigate temperature ranges that were never reached before (corresponding to energies of the order ~ 0.1 meV).

Nevertheless, the implementations of the different methods to calculate α went through unforeseen difficulties. They are mainly related to the extremely high number of wave vectors required for an accurate result at low temperatures — up to 10 billion k-points were necessary for the convergence investigation. Such numbers are too large to fit on the standard 4-byte integer. Since compilation flags to change the default integer size caused errors in other parts of the code, all the variables needed to be recognized and modified one by one. Not only the number of vectors itself was too large, but a full list of k-points could take hundreds of Gb of space — especially in the new energy-dependent mesh that used combined {E, k} points. This issue was solved by generating the required k-points for each process locally, greatly improving the memory usage of the program.

An extra addition to the code, not planned in the proposal, was also done: a completely new orbital-dependent charge self-consistency, which can now take into account charge transfer between different elements in the unit cell. These are important for a better description of complex unit cells and are already being used to calculate the ground state of Mn_2Au. In the new self-consistency method, the program solves a system of $8 \times N + 1$ equations (N being the number of sites in the unit cell) to obtain the ground state properties. These equations include the five d orbitals and 3 magnetic moment directions for each site, and an extra equation for the total charge neutrality, adjusting the Fermi level of the system E_F.

Publications with project results

The following pre-print was published using the results obtained in this project and will be soon submitted to publication in a high impact journal [1]:

- GUIMARÃES FSM, SUCKERT JR, CHICO J, BOUAZIZ J, DOS SANTOS DIAS M, LOUNIS S. Comparative study of methodologies to compute the intrinsic Gilbert damping: interrelations, validity and physical consequences. J. Phys.: Condens. Matter 31. 2019;255802. arXiv:1807.11808 [cond-mat.mes-hall]

Theses completed within the project

The master thesis of J. R. Suckert entitled TITAN: A code and its applications for time-dependent transport and angular momentum in nanostructures was done using the results obtained in this project.

References

[1] GUIMARÃES FSM, SUCKERT JR, CHICO J, BOUAZIZ J, DOS SANTOS DIAS M, LOUNIS S. Comparative study of methodologies to compute the intrinsic Gilbert damping: interrelations, validity and physical consequences. May 2018. arXiv:1807.11808.

[2] GILBERT TL. A phenomenological theory of damping in ferromagnetic materials. IEEE Trans. Magn. Nov. 2004;40,no.6:3443–3449.

[3] KAMBERSKY V. On ferromagnetic resonance damping in metals. Czech J Phys. Dec. 1976;26,no.12:1366–1383.

[4] BRATAAS A, TSERKOVNYAK Y, BAUER GEW. Scattering Theory of Gilbert Damping. Phys. Rev. Lett. 2008;101, no.3:037207.

[5] GARATE I, MACDONALD A. Gilbert damping in conducting ferromagnets. I. Kohn-Sham theory and atomic-scale inhomogeneity. Phys. Rev. B. Feb. 2009;79,no.6:064403.

[6] EDWARDS DM. The absence of intrabandscattering in a consistent theory of Gilbert damping in pure metallic ferromagnets. J. Phys.: Condens. Matter. Mar. 2016;28,no.8:086004.

Electronic and transport properties of magnetic systems at high temperature from ab-initio calculations

Project ID: jara0051
PHIVOS MAVROPOULOS
Peter Grünberg Insitute,
Quantum Theory of Materials, (IAS-1),
FZ Jülich

ROMAN KOVACIK
Peter Grünberg Insitute,
Quantum Theory of Materials (IAS-1),
FZ Jülich

Scientific work accomplished and results obtained

The central aim of this project has been to promote the understanding of electronic, magnetic and transport properties of magnetic materials at high temperature, and especially close to the magnetic phase transition temperature, based on quantum-mechanical, density-functional calculations coordinated with Monte Carlo and spin-dynamics simulations.

The flagship among the sub-projects was the development of an ab-initio program for the description of the electronic structure and transport properties of ferromagnetic systems at high temperature (close to the Curie temperature), when the magnetic moment fluctuations become important. The approach was based on density-functional calculations for the electronic states, a Heisenberg Hamiltonian for the description of the magnetic interactions, a Monte Carlo treatment of the magnetic state at high temperatures, and a Landauer-Büttiker approach to electron transport.

In parallel, we developed a spin-dynamics code based on a self-consistent tight-binding method, in order to monitor the time-dependent evolution of the magnetic structure at elevated temperatures. The implementation and results of this part were described in previous reports.

The calculated transport properties included the spin-disorder resistivity, Seebeck coefficient, spin conductivity and spin-Seebeck coefficient. These results were also described in previous reports. Here we focus on results of the spectral function.

In disordered systems with periodic lattice structure, the Bloch spectral function A(k;E) represents a “k-dependent density of states”. The spectral function is defined by the following relation [Soven 1966; Faulkner 1980]

$$A(\boldsymbol{k};E) = -\frac{1}{\pi}\mathrm{Im}\sum_{m,n}\int d^3r\, G(\boldsymbol{r}+\boldsymbol{R}_n,\boldsymbol{r}+\boldsymbol{R}_m;E)e^{i\boldsymbol{k}\cdot(\boldsymbol{R}_n-\boldsymbol{R}_m)}, \quad (1)$$

where $G(r+R_n,r+R_m;E)$ is the Green function and R_n and R_m are lattice vectors. In case of an ordered system, A(k;E) has the form of a **δ**-function, $\boldsymbol{\delta}(E-E_k)$, at energies E and crystal momenta k satisfying the band-structure. $E=E_k$. In the presence of disorder, the bands appear broadened and “smeared out” in energy. In our case, the disorder is not chemical, but magnetic, and stems from the random orientation of the magnetic moments at different sites. For the calculation of the average Green function we applied the method described in Sec. 2.

We applied formula (1) to the case of magnetic Heusler alloys with different properties (see also Fig.1).

- NiMnSb, a half-Heusler alloy in the $C1_b$ structure, is a prototypical half-metallic ferromagnet, i.e., its ground state is characterized by an energy gap around E_F in one spin direction, while it is metallic in the other spin direction. Its ground state magnetization is M = 4 μ_B per formula unit (f.u.). The measured Curie temperature is 732 K [Webster 1984].
- Mn_2CoAl, an inverse Heusler alloy, is a spin gapless ferrimagnetic semiconductor (i.e., the conduction band and the valence band touch, as in a semi-metal, but correspond to only one spin direction, while the other spin direction shows a clear gap). It has a ground-state magnetic moment of M = 2 μ_B per f.u. Its measured Neel temperature is 720 K [Ouardi 2013].
- CrVTiAl, a quaternary Heusler alloy, is also a spin gapless semiconductor. At the same time it is a fully compensated ferrimagnet (i.e., each sub-lattice shows a magnetic moment, either in the up or down direction, but their sum vanishes: M = 0). Its measured Neel temperature is at least 400 K [Stephen 2016].

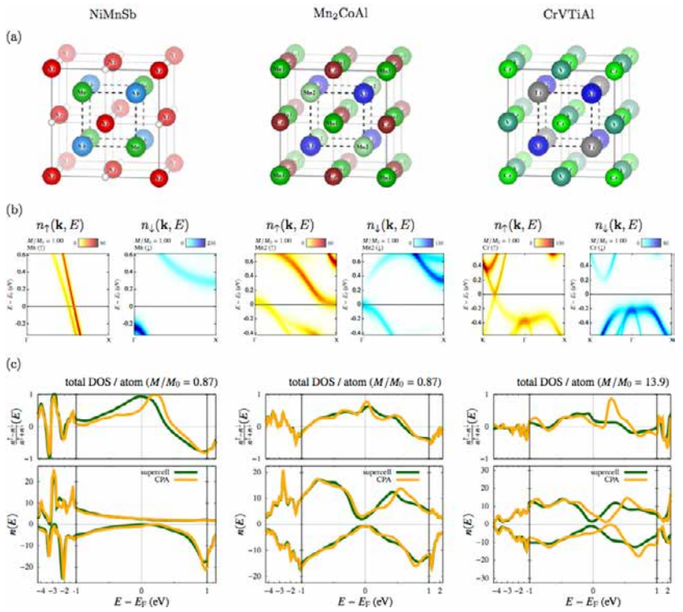

Fig. 1. (a) Crystal structure of Heusler alloys selected for this study. (b) **k**-resolved density of states in the vicinity of the Fermi energy (E_F) for up [n↑(**k**, E)] and down [n↓(**k**, E)] spin. (c) Density of states (bottom) and its polarization (top) at simulated temperature T ≈ 300 K calculated by the CPA and real space disorder in the supercell methods. n↓(E) is plotted in an inverted axis.

Fig. 1a shows the structure of the three materials and Fig. 1b shows the **k**-resolved density of states at zero temperature (band structure) for the two spin directions. Fig. 1c shows the **k**-integrated density of states per spin [n↑(E) and n↓(E)] and the spin polarization [n↑(E)-n↓(E)] / [n↑(E) + n↓(E)], focusing in the region around the Fermi level. Two calculations are presented for a temperature of 300 K: the calculation according to the supercell method with averaging of many spin configurations, and the Coherent Potential Approximation (CPA), in which the magnetic disorder is tuned in such a way that the total magnetization is equal to the calculated magnetization at 300 K by the Monte Carlo method.

The polarization at E_F is probably the most important quantity from the viewpoint of spintronics. We see that this quantity differs considerably in the two approximations for NiMnSb and CrVTiAl, even if the qualitative trend is similar. Since the CPA is an approximation to the supercell method, we conclude that, indeed, a supercell method may give quantitatively improved results, with respect to the CPA, for the spin polarization in the case of magnetic disorder.

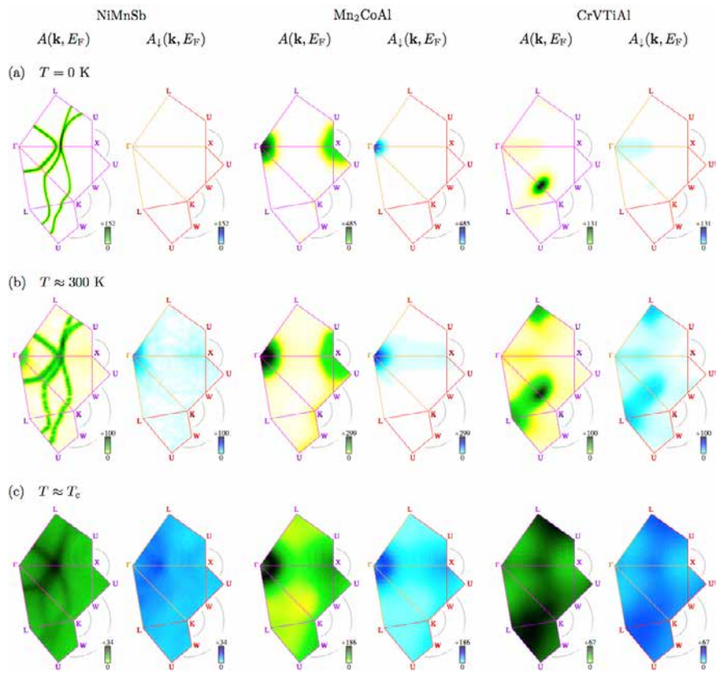

Fig.2. (a) The Bloch spectral function $A(\mathbf{k},E_F)$ as a function of k on the surface of the irreducible wedge of the Brillouin zone calculated at the Fermi energy. The spin sum A = A↑ + A↓ and A↓ are shown left and right, respectively, for the individual alloys.

Fig. 2 shows the spectral function summed for both spin directions, A = A↑ + A↓, and the spectral function just for spin down, A↓, at EF and at different temperatures, on the surface of the irreducible wedge of the Brillouin zone, for the same compounds as in Fig. 1. Evidently, at higher temperatures (stronger disorder) the bands are blurred out.

Particularly NiMnSb and Mn_2CoAl show rather robust bands (there is a smearing due to the temperature, but they also show an easily recognizable shape) up to T_C. The spin-down band gap is well preserved throughout the Brillouin zone at RT. For CrVTiAl, the polarization is strongly reduced and the band gap is lost even at room temperature throughout the Brillouin zone.

Realization of the project

Our method follows, conceptually, the following sequence of steps [Kovacik 2014, Kovacik 2015]:

1. Using the Korringa-Kohn-Rostoker Green function method [JuDFT, Ebert 2011], and based on density-functional theory, we calculate the ground-state electronic and magnetic structure of the ferromagnetic system.
2. Based on the ferromagnetic solution, and using the Green-function-based method of infinitesimal rotations [Liechtenstein 1987], we calculate the exchange parameters that correspond to a Heisenberg model for the excited magnetic state.
3. Applying a Monte Carlo method to solve the Heisenberg model, we calculate the magnetization as a function of temperature. At each temperature of interest, we save a number of system “snapshots” that correspond to thermal equilibrium. A snapshot consists of the set of magnetic moment directions at each individual atom in the system in a Monte Carlo step.
4. Using the individual snapshots at each temperature, we calculate the electronic structure in a “one-shot” way, i.e., we substitute the ground-state magnetic moment directions with directions given by a snapshot, and solve the Schrödinger equation non-self-consistently. This is done in a large periodic supercell, in order to capture the correlation of magnetic moments up to a reasonable distance.
5. From the calculated electronic states of the previous step, we harvest the spectral density and the transport coefficients for each snapshot and we average over a number of snapshots at each temperature.

In this way, we are able to calculate the thermally averaged electronic and transport properties of ferromagnetic systems, as they are influenced by the fluctuating magnetic moments. The computationally most expensive part is step number 4, where the Green function must be calculated for many snapshots at a number of energies around the Fermi level. Without massively parallel calculations on supercomputers, this step would be an impossible task.

References

- [Ebert 2011] EBERT H, KÖDDERITZSCH D, MINAR J. Rep. Prog. Phys. 2011;74:096501.
- [Faulkner 1980] FAULKNER JS, STOCKS GM. Phys. Rev. B. 1980;21:3222.
- [JuDFT] www.judft.de
- [Liechtenstein 1987] LIECHTENSTEIN AI, KATSNELSON MI, ANTROPOV VP, GUBANOV VA. J. Magn. Magn. Mater. 1987;67:65.
- [Kovacik 2014] KOVÁCIK R, MAVROPOULOS P, WORTMANN D, BLÜGEL S. Phys. Rev. B. 2014;89:134417.
- [Kovacik 2015] KOVÁCIK R, MAVROPOULOS P, BLÜGEL S. Phys. Rev. B. 2015;91:014421.
- [Ouardi 2013] OUARDI S, et al. Phys. Rev. Lett. 2013;110:100401.
- [Soven 1966] SOVEN P. Phys. Rev. 1966;151:539.
- [Stephen 2016] STEPHEN GM, et al. Appl. Phys. Lett. 2016;109:242401.
- [Webster 1984] WEBSTER PJ, MANKIKAR RM. J. Mag. Mag. Mater. 1984;42:300.

Publications related to the full period of the project

- KOVÁCIK R, MAVROPOULOS P, WORTMANN D, BLÜGEL S. Spin-caloric transport properties of cobalt nanostructures: Spin disorder effects from first principles. Phys. Rev. B. 2014;89:134417. DOI: 10.1103/PhysRevB.89.134417.
- KOVÁCIK R, MAVROPOULOS P, BLÜGEL S. Spin transport and spin-caloric effects in (Cr,Zn)Te half-metallic nanostructures: Effect of spin disorder at elevated temperatures from first principles. Phys. Rev. B. 2015;91:014421. DOI: 10.1103/PhysRevB.91.014421.
- POPESCU V, KRATZER P, ENTEL P, HEILIGER C, CZERNER M, TAUBER K, TÖPLER F, HERSCHBACH C, FEDOROV DV, GRADHAND M, MERTIG I, KOVÁCIK R, MAVROPOULOS P, WORTMANN D, BLÜGEL S, FREIMUTH F, MOKROUSOV Y, WIMMER S, KÖDDERITZSCH D, SEEMANN M, CHADOVA K, EBERT H. Spin caloric transport from density-functional theory. J. Phys. D: Appl. Phys. 2019;52:073001. DOI: 10.1088/1361-6463/aae8c5.

Ab initio study of interfacial phase-change materials and thin chalcogenides

Project ID: jara0150
RICCARDO MAZZARELLO
Institute for Theoretical Solid State Physics, Theoretical Nanoelectronics, RWTH Aachen University

MATTHIAS WUTTIG
I. Institute of Physics (IA), RWTH Aachen University

VALENTIN EVANG
IDER RONNEBERGER
PETER CHRISTIAN SCHMITZ
MATHIAS SCHUMACHER
Institute for Theoretical Solid State Physics, RWTH Aachen University

Several projects were carried out and completed using the computational resources from JARA0150. In the following the main achievements of each project are discussed.

Project 1: Design of a novel phase-change material.
This project was carried out in close collaboration with the Chinese Academy of Sciences, Shenzhen University, and Xi'an Jiaotong University (China). In this project, a new, ultrafast phase-change material (PCM) – $Sc_{0.2}Sb_2Te_3$ – capable of crystallizing in less than 1 nanosecond was discovered using computational materials design [1]. Subsequently, our colleagues at Chinese Academy of Sciences and Shenzhen University built prototypes of phase-change random-access memories containing $Sc_{0.2}Sb_2Te_3$ with subnanosecond switching time. The resulting write speed is comparable to that of SRAM and, thus, paves the way for the development of cache-type phase-change memories to boost the working efficiency of computing systems. Current products based on the PCM $Ge_2Sb_2Te_5$ are limited by the tens of nanoseconds writing speed, which stems from the stochastic crystal nucleation that occurs in this material during crystallization. In our work, we considered the binary compound Sb_2Te_3, which forms a rocksalt phase upon fast crystallization (similarly to $Ge_2Sb_2Te_5$), and we carried out a computational materials screening of transition-metal alloys to speed up its crystallization kinetics. Two criteria were used to select the alloy that best promotes the crystalline precursors in the amorphous state, namely the 4-membered primitive rings: geometric matching to the rocksalt phase of Sb_2Te_3 and strong chemical bonds between the transition metal and Te. Our density-functional-theory (DFT) simulations indicated that Scandium is the best candidate (Figure 1). Indeed, the subsequent experiments confirmed that the scandium antimony telluride ($Sc_{0.2}Sb_2Te_3$) compound allows a writing speed of only 700 picoseconds without preprogramming in a large conventional memory device. Besides the computational materials screening, ab initio molecular dynamics simulations of models of $Sc_{0.2}Sb_2Te_3$ containing 400-500 atoms were also performed to study the crystallization kinetics at high temperature of the order of 600 K. The simulations showed that the ultrafast crystallization originates from the reduced stochasticity of nucleation through geometrically matched and robust scandium telluride (ScTe) chemical bonds. Our combined computational and experimental work has been recently published in Science [1].

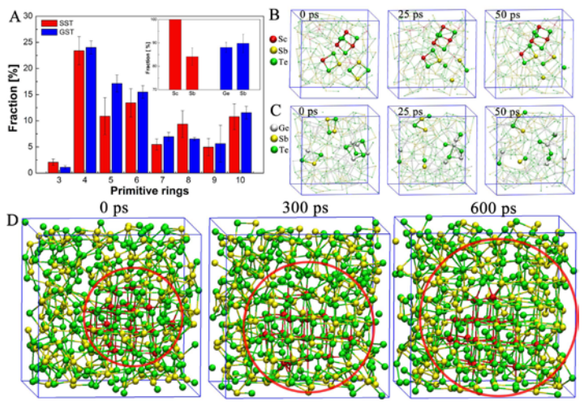

Figure 1. A) Primitive rings analysis of amorphous $Sc_{0.2}Sb_2Te_3$ and $Ge_2Sb_2Te_5$. (Inset) Fraction of Sc and Sb atoms (respectively, Ge and Sb atoms) involved in at least one ABAB (A=Sc/Sb resp. Ge/Sb and B=Te) ring. (B and C) The stability of ABAB rings in $Sc_{0.2}Sb_2Te_3$ and $Ge_2Sb_2Te_5$ at ~600 K. (D) Crystallization process of $Sc_{0.2}Sb_2Te_3$ with a crystalline embryo in the middle at ~600 K.

Project 2: Monatomic phase-change memories.
This project was also carried out in close collaboration with experimental groups (Martin Salinga, RWTH Aachen University; Abu Sebastian, IBM Zurich). The main goal of the project was to design ultrasmall phase-change memory cells made of a single element (antimony). Using monatomic cells eliminates problems related to unwanted deviations from the optimized stoichiometry in the switching volume. Such problems become severe when devices are confined in extremely small volumes. It is known Sb crystallizes very rapidly, and it is thus very challenging to retain Sb in its amorphous state at room temperature. We performed ab initio molecular dynamics simulations of quenching of small models of antimony (containing between 360 and 720 atoms) using different cooling rates (see Figure 2). Our results showed that the stability of amorphous Sb against crystallization at room temperature depends on the rate at which it is cooled from the melt [2]. These simulations suggest that very high cooling rates and suitable confinements at the nanoscale could increase the stability of the amorphous state dramatically. Our experimental colleagues managed to reach fast cooling rates of 10^{10} Kelvin per second in an ultrascaled real device setting consisting of Sb films with thickness ranging between 3 and 10 nm confined inside SiO_2 layers. In this setup, fast and reversible switching was observed between the amorphous and crystalline state. Remarkably, amorphous Sb survived up to 50.8 hours at 20°C and about 100 seconds at 60-70°C. Such retention times are already adequate for some "quasi-non-volatile" applications, including memory-mapped storage class memory, in-memory computing and brain-inspired neuromorphic computing. Our joint computational and experimental work has been published very recently in Nature Materials [2].

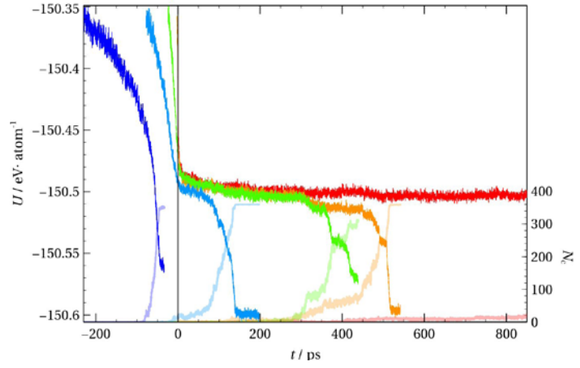

Figure 2: Quenching from the melt of an AIMD model Sb containing 360 atoms. Different colors correspond to different quenching rates (3 K ps^{-1}, purple; 9.5 K ps^{-1}, blue; 30 K ps^{-1}, green; 300 K ps^{-1}, orange; abrupt quenching in a single simulation step, red). For all the models, the target temperature of 300 K is reached at time t = 0 ps. The degree of crystallization is monitored by the number of crystalline-like particles Nc (right axis). Crystallization is accompanied by a drop in potential energy (left axis) below around –150.5 eV per atom. The data clearly show that an increase in the quenching rate hinders crystallization. The simulation with the slowest quenching rate (purple) was aborted before reaching the target temperature as crystallization occurred during quenching.

Project 3: Investigation of ultrathin phase-change materials.
Ultrathin layers of GeTe, SnTe and similar compounds provide information about the structure and chemical bonding of PCMs near the two-dimensional limit. We performed DFT simulations of ultrathin films of GeTe and SnTe in the buckled phase, corresponding to the growth along the [111] direction [3]. The goal was twofold: understand the bonding mechanisms as a function of thickness and shed light on a highly unconventional growth scenario observed upon layer-by-layer deposition of GeTe films on the hydrogen passivated Si(111) surface. In such experiments, an amorphous film formed for growth parameters that should yield a crystalline material. The amorphous film crystallized only once a critical thickness of four GeTe bilayer is reached. Hence, an improvement in atomic order was observed above a critical film thickness, in contrast to conventional lattice-matched epitaxial

systems. Experimental Raman spectra also showed a pronounced shift of the vibrational modes above the critical thickness that was attributed to a change in the nature of the bonds. Indeed, our calculations of relevant bond indicators including dielectric constants and Born effective charges by DFT showed that ordinary covalent bonding is found in ultrathin films, whereas resonant bonding prevails in thick films (Figure 3). We have also investigated the properties of ultrathin films of GeTe, SnTe, GeSe and SnSe in the puckered phase, corresponding to the growth along the [100] direction. A paper about these results is in preparation [4]. Finally, we have studied the structural and vibrational properties of crystalline two-dimensional $GeTe_2$, a metastable compound observed in GeSbTe samples grown by sputtering [5].

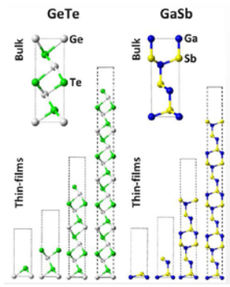

	GeTe		
	1 BL	2BL	Bulk
ε^{∞}	16.7	24.9	57.6
Z^*	1.6	1.8	6.9

	GaSb		
	1 BL	2BL	Bulk
ε^{∞}	22.5	34.9	18.2
Z^*	2.7	2.2	1.7

	SnTe		
	1 BL	2BL	Bulk
ε^{∞}	14.4	21.3	50.1
Z^*	2.1	2.1	6.7

Figure 3: Bulk and thin-layer models of GeTe and GaSb. All structures are fully relaxed with respect to cell parameters and atomic positions. The corresponding values for the dielectric constant ε∞ and Born effective charges Z* are reported. The data for thin layers of SnTe are also included. For GeTe and SnTe, ultrathin films show very low values of ε∞ and Z*, incompatible with resonant bonding, while the bulk samples possess this characteristic fingerprint.

Project 4: Study of the structural, electronic and kinetic properties of superlattices of Sb_2Te_3 and selected GeSbTe compounds.

We carried out a thorough investigation of the properties of superlattices consisting of Sb_2Te_3 blocks and GeSbTe blocks, including $GeSb_2Te_4$, $Ge_2Sb_2Te_5$, $Ge_3Sb_2Te_6$, and $Ge_4Sb_2Te_7$. Such superlattices form a new family of PCMs called interfacial phase-change materials [i]. We performed geometry relaxations and electronic structure calculations with spin-orbit coupling. Besides investigating the equilibrium structure, we also considered the effects of strain on the electronic structure. This is relevant to experiments since, in a multi-compound superlattice, the building blocks may be subject to considerable pressure/strain. Our most important finding is that some of these superlattices, including the prototypical $Ge_2Sb_2Te_5$, undergo topological phase transitions between a) normal insulating (NI) phases, b) topological insulators (TI) [ii] and c) topological Dirac semimetals (TQDSM) [iii]. A paper about these results is in preparation [6].

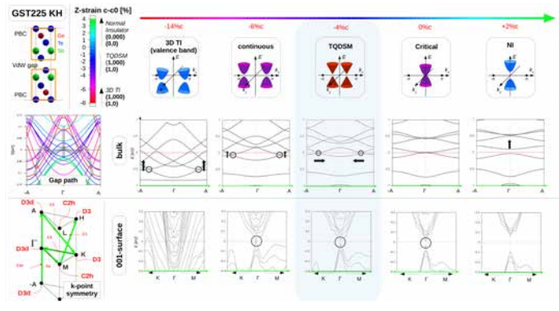

Figure 4: Evolution of bulk- and (001) surface band structures for z-strained $Ge_2Sb_2Te_5$ (denoted as GST225-KH), whose atomic structure is shown in the upper left part. For z-strain equal to -4%c (where c denotes the cell parameter along z), the bulk band structure along the path –A-Γ -A exhibits two "quasi" Dirac points at the Fermi energy. In contrast to the topological Dirac semimetal phase predicted in [iii], however, a small gap of the order of 15 meV is present. This gap stems from the fact that the two relevant bands belong to the same irreducible representation of the k-point symmetry-group (C_{3v} along Γ A). The lower-left part shows the irreducible Brillouin zone and the k-point symmetry groups.

We have also performed ab initio molecular dynamics simulations of Sb_2Te_3-GeSbTe superlattices at temperatures below and above the melting temperature of bulk GeSbTe and Sb_2Te_3, followed by fast quenching, to determine if the melting temperature of quasi two-dimensional GeSbTe and/or Sb_2Te_3 is lower than the bulk value and the amorphization of GeSbTe is facilitated due to interfacial or strain effects, as hypothesized in Ref. [iv]. We have carried out AIMD simulations of amorphous GeSbTe and crystalline Sb_2Te_3 superlattices at different temperatures as well to determine whether crystallization of the GeSbTe layer is enhanced due to template growth within the crystalline Sb_2Te_3 matrix. Finally, we have performed metadynamics simulations [v] to accelerate the transition from the crystalline state to a partially amorphous state by means of a bias potential.
Our simulations indicate that the melting temperatures of GeSbTe and Sb_2Te_3 are indeed affected by the superlattice structure and that, by a proper tuning of the quenching rates, partial amorphization of GeSbTe occurs. Further simulations are however needed to assess if this phenomenon is relevant to real devices based on chalcogenide superlattices.

Project 5: An initio investigation of liquid GeTe.

This project was done in collaboration with the experimental group of I. Kaban (IFF Dresden). We investigated the structural and kinetic properties of the stable and supercooled liquid state of GeTe by ab initio molecular dynamics simulations, in combination with diffraction experiments and oscillating cup measurements [7]. The study of the liquid phase is important to elucidate the amorphization and crystallization processes of this prototypical phase-change material. We showed that the structural properties of the models obtained from molecular dynamics simulations and reverse Monte Carlo simulations are in good agreement with neutron and X-ray diffraction experiments. We also extracted the kinetic coefficients from the molecular dynamics trajectories and determined the activation energy for viscosity. The obtained values are compatible with the viscosity measurements.

Usage of the RWTH compute cluster

Ab initio molecular dynamics simulations based on DFT were carried out using the Quickstep code included in the CP2K package (projects 1, 2, 4, 5) [vi]. The performance and scalability of CP2K on the CLAIX2016-MPI cluster (and on the Bull cluster) was good up to 192 cores (8 nodes) for the models we studied, which contained about ~400-700 atoms (see Figure 5). The total amount of memory needed for each model was of the order of 100-200 Gb, corresponding to up to 25 Gb per node if 8 nodes were used. We used a time step of 2 fs.

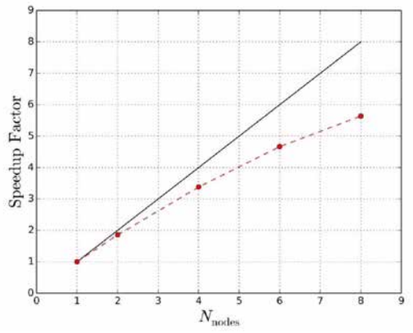

Figure 5: Scaling behavior of Quickstep on the CLAIX2016-MPI cluster. This test was performed on a model of GeTe with 512 atoms (256 Ge and 256 Te atoms, 2560 valence electrons). The density cutoff is set to 300 Ry. The relative speedup normalized to 4 nodes is shown (1 node = 24 cores).

The Quantum Espresso DFT package [vii] was extensively used for project 3 and for the part of project 4 focused on the electronic and topological properties of GeSbTe. Since the models employed were relatively small, these simulations were not extremely demanding in terms of cpu requirement and memory usage.

Own publications that appeared in peer-reviewed journals within the computing time period

[1] RAO F, DING K, ZHOU Y, ZHENG Y, XIA M, LV S, SONG Z, FENG S, RONNEBERGER I, MAZZARELLO R, ZHANG W, MA E.
Science 358. 2017;1423.

[2] SALINGA M, KERSTING B, RONNEBERGER I, JONNALAGADDA P, VU XT, LE GALLO M, GIANNOPOULOS I, COJOCARU-MIREDIN O, MAZZARELLO R, ELEFTHERIOU E, SEBASTIAN A.
Monatomic phase change memory. Nat. Mater. 17. 2018;681.

[3] WANG R, ZHANG W, MOMAND J, RONNEBERGER I, BOSCHKER JE, MAZZARELLO R, KOOI BJ, RIECHERT H, WUTTIG M, CALARCO R.
Formation of Resonant Bonding during Growth of Ultrathin GeTe Films.
NPG Asia Mater. 2017;9:e396.

[4] RONNEBERGER I, ZANOLLI Z, WUTTIG M, MAZZARELLO R.
Paper in preparation.

[5] WANG JJ, RONNEBERGER I, ZHOU L, LU L, DERINGER VL, TIAN L, DU H, JIA C, WUTTIG M, QIAN X, MAZZARELLO R, ZHANG W.
Unconventional two-dimensional germanium dichalcogenides. Nanoscale.
2018;10:7363.

[6] SCHMITZ PC, ZANOLLI Z, ZHANG W, MOKROUSOV Y, MAZZARELLO R.
Paper in preparation.

[7] WEBER H, SCHUMACHER M, JÓVÁRI P, TSUCHIYA Y, SKROTZKI W, MAZZARELLO R, KABAN I.
Experimental and ab-initio molecular dynamics study of the structure and physical properties of liquid GeTe. Phys. Rev. B. 2017;96:054204.

Bibliography

[I] SIMPSON RE, ET AL. Nat. Nanotechnol. 2011;6:501.

[II] HASAN MZ, KANE CL. Rev. Mod. Phys. 2010;82:3045.

[III] YANG BJ, NAGAOSA N. Nat. Comm. 2014;5:4898.

[IV] MOMAND J, ET AL. Nanoscale. 2015;7:19136.

[V] LAIO A, PARRINELLO M. Proc. Natl. Acad. Sci. USA. 2002;99:12562.

[VI] KRACK M, PARRINELLO. In High Performance Computing in Chemistry. Edited by Grotendorst J (NIC, Jülich, 2004). Vol.25:29-51. http://cp2k.berlios.de.

[VII] GIANNOZZI P, BARONI S, BONINI N, CALANDRA M, CAR R, CAVAZZONI C, CERESOLI D, CHIAROTTI GL, COCOCCIONI M, DABO I, DAL CORSO A, FABRIS S, FRATESI G, DE GIRONCOLI S, GEBAUER R, GERSTMANN U, GOUGOUSSIS C, KOKALJ A, LAZZERI M, MARTIN-SAMOS L, MARZARI N, MAURI F, MAZZARELLO R, PAOLINI S, PASQUARELLO A, PAULATTO L, SBRACCIA C, SCANDOLO S, SCLAUZERO G, SEITSONEN AP, SMOGUNOV A, UMARI P, WENTZCOVITCH RM. J. Phys.: Condens. Matter. 2009;21:395502.

Selected conference participations

- Ab initio simulations of phase-change materials, invited talk given at the 2018 Glass and Optical Materials Division (GOMD) Meeting, San Antonio, USA, May 20-24, 2018
- Monatomic phase change memory, 2018, invited talk given at the 2nd Sino-German Workshop on Electronic and Memory Materials, Xi'an, China, September 5-8
- Ab initio guided design of an ultrafast phase-change material, invited talk given at the 9th International Workshop on Characterization and Modeling of Memory devices, Milan, Italy, September 27-28, 2018

Selected National and international cooperations

- Peter Zalden, European XFEL, Schenefeld, Germany
- Ivan Kaban, IFW Dresden, Institute for Complex Materials, Dresden, Germany
- Raffaella Calarco, Paul Drude Institute, Berlin, Germany
- Wei Zhang, Xi'an Jiaotong University, Xi'an, China
- Abu Sebastian, IBM Zurich, Switzerland

Topological transport in real materials from ab initio

Spin currents and spin torques in bulk and interfacial transition-metals.
Spin-orbit torque (SOT) recently became a phenomenon of great interest in spintronics since the possibility of switching the magnetization in several systems was experimentally demonstrated. The SOT, in combination with the Dzyaloshinskii-Moriya interaction (DMI) and SHE is believed to serve as a foundation for future generation of memory devices based on domain wall motion. The main ingredients of the SOT are the ferromagnetic magnetization, spin-orbit interaction, and (locally) broken inversion symmetry. The interplay between the SOT, spin pumping, spin currents and SHE is one of the most intensively researched topics in metallic spintronics these days, and these effects are at the core of our research these days as well.

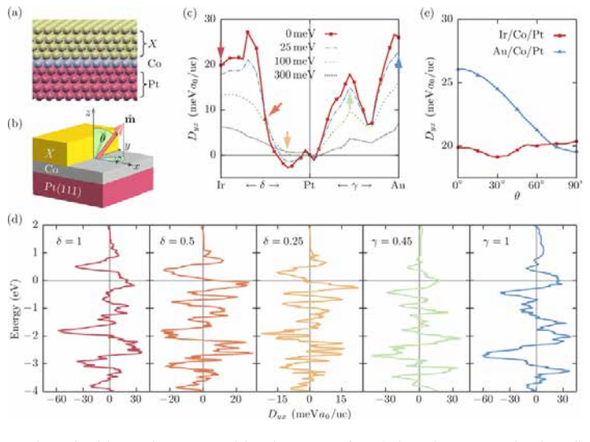

Figure 1: (a) Crystal structure of the heterostructure, which comprises in total nine atomic layers, including the Pt(111) substrate, the ferromagnetic Co monolayer, and the overlayers X. (b) The magnetization direction **m** of the Co atoms is represented by the polar angle θ and the azimuthal angle φ. In this work, we consider the case of φ=0, i.e., the magnetization direction is specified by the single angle θ. (c) Dzyaloshinskii–Moriya spiralization D_{yx} as a function of the overlayer composition in $Ir_\delta Pt_{1-\delta}$/Co/Pt and $Au_\gamma Pt_{1-\gamma}$/Co/Pt, respectively, where the magnetization is oriented perpendicular to the film plane. While the solid red curve corresponds to the clean limit, the thinner lines include the effect of disorder due to a finite band broadening Γ of 25, 100, and 300 meV. The spiralization is given in the units $meVa_0/uc$, where a_0 is Bohr's radius and "uc" stands for the in-plane unit cell. (d) Energy dependence of D_{yx} in the clean limit for the various alloy concentrations that are marked in (c) by arrows. The energy scale is relative to the corresponding Fermi level. (e) Anisotropy of D_{yx} with the polar angle θ in the inversion-asymmetric heterostructures Ir/Co/Pt and Au/Co/Pt. For more details see [Han18].

(i) Embedding the basic ideas of spintronics into future information technologies relies crucially on our ability to control and manipulate efficiently the magnetic state of nanomagnets, for example, by utilizing relativistic effects. In this context, the Dzyaloshinskii–Moriya interaction experiences revived prominence as it can stabilize chiral magnetic textures in inversion-asymmetric crystals with spin–orbit coupling. The DMI facilitates in particular the formation of topologically non-trivial magnetic skyrmions, and assists the current-induced ultrafast motion of domain walls. Recently, the magnitude of the interfacial DMI was shown to be tunable in multilayers of Co in between heavy metals such as Pt and Ir, which holds bright prospects for the observation of small skyrmions at room temperature. In our recent work we promoted our advanced first-principles scheme that is ideally suited to describe efficiently the DMI in the modern theory based on the ferromagnetic state with magnetization direction **m**. This advanced higher-dimensional Wannier interpolation first-principles technique can be used to evaluate not only the DMI in its modern theory but also the Berry curvatures in the mixed space of crystal momentum and magnetization direction. This generic method can be used to study the Hamiltonian evolution

Project ID: jara0062

YURIY MOKROUSOV
Peter Grünberg Insitute, Quantum Theory of Materials (PGI-1 / IAS-1), FZ Jülich

CHENGWANG NIU
FRANK FREIMUTH
BERND ZIMMERMANN
PATRICK BUHL
JAN-PHILIPP HANKE
FABIAN LUX
MATTHIAS REDIES
MAXIMILIAN MERTE
Peter Grünberg Insitute, Quantum Theory of Materials (PGI-1 / IAS-1), FZ Jülich

under slowly varying parameters in various fields of physics. We demonstrated that our method facilitates the accurate prediction of DMI and the intimately related spin–orbit torques for a wide community of researchers that work routinely with the Wannier interpolation. As an example, we applied our method to the Co-based trilayers $Ir_{\delta}Pt_{1-\delta}$/Co/Pt and $Au_{\gamma}Pt_{1-\gamma}$/Co/Pt, where we uncovered an intricate interplay between the overlayer composition and the chiral interaction. By emphasizing the correlations with the electronic structure of these systems, we analyzed the microscopic origin of the DMI and identify its anisotropy with the magnetization direction. In particular, by studying the dependence on the overlayer composition, we demonstrate that both magnitude and sign of the DMI in these ferromagnetic heterostructures can be tuned by means of electronic-structure engineering, see Fig. 1. Generally, we anticipate characteristic sign changes of the spiralization to manifest in systems with moderate Ir concentrations, which we proclaim as promising materials for experiments to investigate in more detail [Han18].

(ii) Only recently, the research on electrically-controlled magnetization switching started to reach out to topological condensed matter – for example, very efficient magnetization switching has been achieved lately in metallic systems incorporating topological insulators. And although in latter cases a strong SOT can be generated, the resulting electric-field response does not rely on the global topological properties of these trivial systems. The discovery of a quantized version of the anomalous Hall effect in magnetic insulators with non-trivial topology in momentum space led to a revolution in forging new spintronic device concepts that utilize topology. On the other hand, moving the field of magnetization controlby SOTs into the realm of topological spintronics would open bright avenues in exploiting universal arguments of topology for designing magneto-electric coupling phenomena in magnetic insulators. With our latest work [Han17b], we firmly put the phenomenon of SOT on the topological ground. In this work, using model arguments and first-principles calculations, we investigate the origin and size of anti-damping SOTs and DMI in representative topologically non-trivial magnetic insulators: (i) magnetically doped graphene, and (ii) a functionalized bismuth film. We demonstrate that these systems can be naturally interpreted as realizations of mixed Weyl semimetals in the composite phase space of **k** and **m**, see Fig. 2. Remarkably, we find that the magnitude of SOTs and DMI in the considered family of insulators can reach gigantic values exceeding by far that of conventional metallic ferromagnets. We show that emergent magnetic monopoles arising within the context of mixed Weyl semimetallic states in the electronic structure of corresponding materials act as sources of a large mixed Berry curvature in the composite phase space. We also point out intriguing perspectives for the electric-field control of magnetization in absence of longitudinal charge currents in these systems, which may ultimately lead to an ultralow power consumption of future spintronic devices exploiting SOTs. In the examples that we considered in this work, the non-trivial topology of mixed Weyl semimetals also leads to DMI changes over a wide range of values throughout the bulk band gap, implying that proper electronic-structure engineering enables us to tailor both strength and sign of the DMI in a given system, for instance, by doping or applying strain. Such versatility could be particularly valuable for the stabilization of chiral magnetic structures such as skyrmions in insulating ferromagnets. In the latter case, very large values of the anti-damping SOT arising in these systems would open exciting perspectives in manipulation and dynamical properties of chiral objects associated with minimal energy consumption by magneto-electric coupling effects. Generally, we would like to remark that magnetic monopoles in the composite phase space, which we discuss here, do not only govern the electric-field response in insulating magnets but are also relevant in metals, where they appear on the background of metallic bands [Han17b].

(iii) In the past year we have significantly advanced also in our understanding of the direct interaction of the laser light and the magnetization. In our recent work [Fre16b], we combined ab initio electronic structure calculations with the developed Keldysh nonequilibrium formalism in order to study laser- induced torques and nonequilibrium spin polarization in bcc Fe, hcp Co, and $L1_0$ FePt. Another effect triggered by fs laser pulses is ultrafast demagnetization. Several experiments and theories suggest that ultrafast demagnetization is accompanied by a breakdown of the local magnetic moments and by a collapse of the exchange splitting. Since the electric conductivity tensor is affected by such electronic structure changes one can use measurements of the electric conductivity tensor in order to assess to which extent ultrafast demagnetization is accompanied by a reduction of the exchange splitting. In our recent study [Fre17b] we explored the idea that if a dynamical exchange splitting drives charge currents, this effect can be employed in experiments in order to investigate the question whether ultrafast demagnetization is dominated by transverse spin fluctuations or a reduction of the local magnetic moments depending on the magnetic material, the laser pulse characteristics, and the geometry. Namely, we demonstrated that a dynamical exchange splitting induces measurable electric currents in magnetic bilayer systems with inversion asymmetry and spin-orbit interaction. Using an ab initio approach, we studied this effect in Mn/W(001) and Co/Pt(111) magnetic bilayers. The strong disorder dependence that we find is reminiscent of the odd component of the spin-orbit torque in these magnetic bilayers pointing at the interfacial spin-orbit interaction as common mechanism. The dependence on magnetization direction suggests we view electric currents driven by a dynamical exchange splitting as a ferromagnetic variant of the inverse Edelstein effect. We compare our theoretical results to experiments measuring the THz emission from magnetic bilayer systems under laser illumination. This leads us to the conclusion that when ultrafast demagnetization in Co is triggered by 800 nm 50 fs laser pulses this ultrafast demagnetization is not dominated by a reduction of the local magnetic moments, suggesting an important role of transverse spin fluctuations.

Quota consumed so far by this sub-project constitutes about 35% of the total quota on CLAIX.

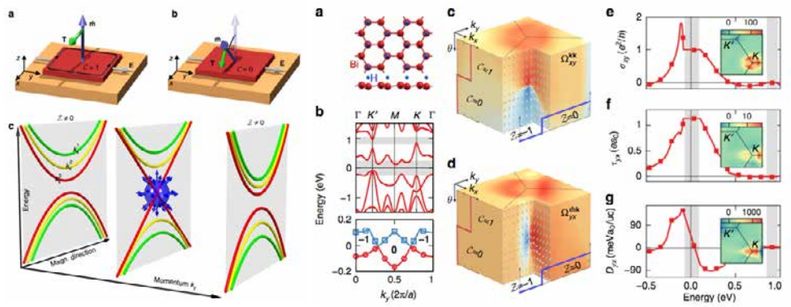

Figure 2: Left: Emergence of mixed Weyl points. (a) The magnetization m = (sin θ, 0, cos θ) of a topologically non-trivial insulator is subject to the anti-damping torque T if an electric field E is applied. (b) The resulting reorientation of the magnetization by θ can trigger a topological phase transition to the trivial insulator. (c) Schematic evolution of two energy bands in the complex phase space of crystal momentum and magnetization direction, where the colors of the bands indicate different k_x. If k_y is tuned, the electronic structure displays a monopole, which is correlated with a change in the mixed Chern number Z. Right: Magnetoelectric properties of a mixed Weyl semimetal. (a) Crystal structure of the semi-hydrogenated Bi(111) bilayer. (b) First-principles band structure for an out-of-plane magnetization, where the region of the topologically complex band gap and the trivial one above are highlighted. In addition, the evolution of valence band maximum (red circles) and conduction band minimum (blue squares) with k_y is shown. Bold integers denote the mixed Chern number Z, and a is the in-plane lattice constant. (c, d) Monopole-like field of momentum space and mixed Berry curvatures near one of the mixed Weyl points. Arrows indicate the direction of the curvature field, and a logarithmic color scale is used to display two of its components, where dark red (dark blue) denotes large positive (negative) values. (e, g) Energy dependence of the anomalous Hall conductivity, the

torkance, and the DMI or magnetization perpendicular to the film plane. Insets show the microscopic distributions in momentum space near K and K′. For more details see [Han17b].

Spin torques, Hall effects and topological characterization of chiral magnets
Here, we continued our research in the direction of novel properties of chiral magnets, their ground state magnetic properties as well as response characteristics which root in the non-trivial topology of chiral magnets in real (spin) and reciprocal (k) spaces. In the past year, in addition to continuous effort in the direction of topological Hall effect of skyrmions, our research took a deeper direction towards the orbital magnetizatism (OM) of chiral magnets.

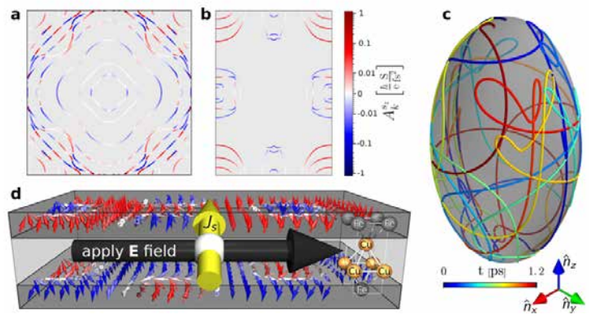

Figure 3: Fermi surface resolved contributions to the topological spin Hall conductivity for a) Fe/Cu_6/Fe trilayer and b) bcc Cr(110) thin film. c) Example spin trajectory of an electron propagating through the AFM skyrmionic texture under the influence of the electric field in the local frame restricted to a prolate spheroid with couplling parameter between two spin sublattices of the order of 0.53 for the case of a). d) Schematic picture of a Fe/Cu_n/Fe trilayer system with imprinted synthetic AFM skyrmion lattice exhibiting the topological spin Hall effect, where J_s stands for the transverse spin current generated by an applied electric field. For more details see [Buh17].

(i) Antiferromagnetic skyrmions, owing to a multitude of their remarkable properties are coming into the focus of intensive attention of skyrmionics community. One of the key manifestations of non-trivial topology of locally ferromagnetic skyrmions is the so-called topological Hall effect (THE). Unlike the ordinary and anomalous Hall effects, the THE within the adiabatic picture originates in the skyrmion's spin structure giving rise to an "emergent" magnetic field which exerts a spin-dependent Lorentz force on electrons propagating through the texture. The observation of the THE in the skyrmion phase of B20 compounds such as MnSi and FeGe has been pivotal in triggering the intensive research on skyrmionic systems. Remarkably, alongside its experimental observation, consistent theoretical description of the THE based on semiclassical arguments has been achieved recently by us based on ab-initio description of $Mn_{1-x}Fe_xSi$ and $Mn_{1-x}Fe_xGe$ alloys [Franz PRL 2014, Gayles PRL 2015]. Given that the locally antiferromagnetic order is more challenging to image experimentally, the analogue of the THE for AFM skyrmions would serve as an ideal tool for their detection. The formulation of such an effect for AFM skyrmions in analogy to the THE for ferromagnetic skyrmions is, however, by far more difficult, owing to more complicated dynamics of electrons in AFM textures even in the adiabatic limit, as well as different gauge symmetry of the Berry phase description of Bloch states in antiferromagnets. In our recent work [Buh17], based on the SU(2) semiclassical framework in combination with density functional theory (DFT) description of the electronic structure, we considered the adiabatic transport in AFM skyrmionic textures. Taking as an example synthetic AFMs, we predict that, while the transverse charge current is vanishing in AFM skyrmionic lattices subject to an external electric field, a strong response in terms of a transverse spin current could be used to detect the emergence of chiral lattices in AFM systems. We demonstrated the emergence of the corresponding topological spin Hall effect (TSHE) taking Fe/Cu/Fe trilayer as a representative example for a synthetic AFM system. We uncovered the physics of this new phenomenon, proved the importance of SU(2) gauge symmetry for its magnitude, and demonstrated the sensitivity of its microscopics with respect to various parameters which determine the electronic structure of complex materials with the utter motivation of triggering the experimental observation of AFM skyrmions, see Fig. 3. We speculate that the prominent TSHE marks the AFM skyrmions as promising objects for pure spin current generation, which, as opposed to the spin Hall effect in paramagnets, is not relying on relativistic effects in the electronic structure. We suggest that such spin currents can be detected with standard techniques, i.e. by detecting the spin- torque that topological spin Hall currents would exert on a ferromagnet brought in contact with the AFM skyrmionic system, or by magneto-optical means in terms of corresponding spin accumulation at the edges of the sample [Buh17].

(ii) In 2015, we have discovered the emergence of the topological orbital magnetization (TOM) in a (3x3) lattice of an Fe monolayer on Ir(001) [Hof15], which is the contribution to the orbital magnetization without spin-orbit coupling purely due to the effect of non-collinearity. From the picture of the TOM that we have developed since then, it became clear that the intrinsic non-locality of the wavefunctions due to the non-collinearity gives rise to local ring currents which are responsible for the magnitude of TOM. Such "non-local" contributions to the OM are, however, not properly accounted for in the commonly used (including ourselves by now) approximations to the OM. To overcome these limitations we have implemented the rigorous expressions for the OM, which are based on linear response and Berry phase theory. Our calculations based on this new implementation revealed the utter role that the modern theory for OM plays for our understanding of the orbital physics in thin films and at surfaces [Han16, Go17], thus calling for its re-evaluation. Recently, we also introduced a notion of so-called topological orbital ferromagnets (TOFs), i.e., ferromagnets for which the macroscopic magnetization is solely dominated by the OM, with the latter originating from the non-trivial topology of spin distribution in real space, rather than SOI [Han16]. In one of the recent works [Han17a], we predicted from first principles an entirely topological orbital magnetization in a well-known noncoplanar bulk antiferromagnet γ-FeMn originating in the nontrivial topology of the underlying spin structure [Han17a]. Studying the influence of strain, composition ratio, and spin texture on the topological orbital magnetization and the accompanying topological Hall effect in γ-FeMn, we reveal the scalar spin chirality as key mechanism lifting the orbital degeneracy and giving rise to TOM in this material. One of the remarkable features of γ-FeMn is the possibility for pronounced orbital magnetostriction mediated by the complex spin topology in real space. Generally, we claim that TOM opens a path to new physics and new vistas in manipulating the magnetization in chiral magnets, since orbital magnetization couples to external magnetic fields, optical perturbations, and orbital currents [Han16, Han17a].

At the current stage, the physics of the TOM is very poorly understood and the rigorous framework for accessing orbital magnetism in chiral spin textures, imperative for our ability to engineer and utilize the orbital degree of freedom of chiral systems for the purposes of orbitronics, has been missing so far. In our most recent study [Lux17] we decided to rigorously address the question of OM in chiral systems with slowly varying magnetization. Namely, by refering to the Green's function perturbation theory, we put the orbital magnetism in chiral systems on firm quantum-mechanical ground. By systematically tracing the orders of perturbation theory for chiral magnetic textures we distinguish corrections to the out-of-plane orbital magnetization of a locally ferromagnetic system, appearing in higher orders of the gradients of the magnetization. In addition to recovering the exact Greens functions expressions for the effect of TOM, appearing at the second order (i.e. relevant in particular for chiral skyrmions), we thereby proposed a novel contribution to the orbital magnetization, which is linear in the chirality of the underlying texture, and which we thus call the chiral orbital magnetization (COM). By explicitly referring to the 2D Rashba model, we numerically

evaluated the magnitude and real-space behavior of the TOM and COM (see Fig. 4), finding that by tuning the parameters of surface and interfacial systems the orbital magnetism of domain walls and chiral skyrmions can be engineered in a desired way. Our findings open new vistas for exploiting the orbital magnetism in chiral magnetic systems. We concluded that the phenomenon of chiral and topological orbital magnetism marks outstanding prospects for "chiral" spintronics and orbitronics. While the magnitude and details of the "local" TOM and COM can be tuned by electronic structure engineering, the topological orbital moment of skyrmions, defined as an integral of TOM density over the skyrmion, is a new type of property in the physics of skyrmions. This observable, in analogy to the topological charge, exhibits either a quantization or a strong protection against deformations of the underlying spin structure, and thus provides unique means for skyrmion detection, manipulation and utilization. In particular, the topological orbital moment can be envisaged to mediate the interaction between skyrmions and circularly-polarized light, giving an opportunity for optical detection and control of the skyrmion topological charge. On the other hand, since the topological orbital moment is directly proportional to the topological charge of the skyrmions, we suggest that the interaction of TOM with external magnetic fields could be used to trigger the formation of skyrmions with large topological charge. Ultimately, the currents of skyrmions can be employed for "lossless" transport of the associated topological orbital momenta over large distances in skyrmionic devices, opening new perspectives in orbitronics [Lux17]. Our next challenge is the ab-initio implementation of the expressions for COM and TOM and their study in realistic systems.

Quota consumed so far by this sub-project constitutes about 45% of the total quota on CLAIX.

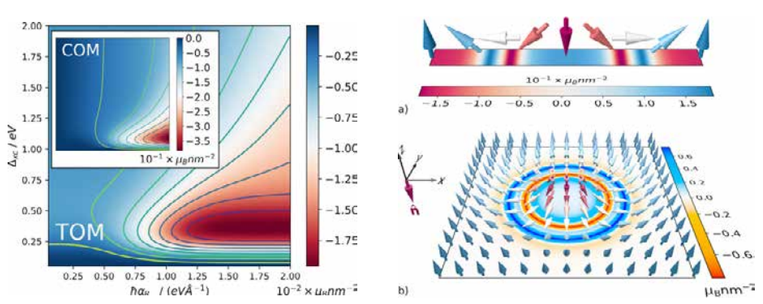

Figure 4: Left: Phase diagram of TOM evaluated at the core of a Neel-type skyrmion as a function of the exchange splitting Δ_{xc} and the Rashba constant α_R of the Rashba Hamiltonian. Inset: phase diagram of COM, evaluated at the position of a spin-spiral (q = 2.86nm^{-1}) with an out-of-plane magnetization as a function of Δ_{xc} and α_R. For more details see [Lux17]. Right: In one-dimensional and two-dimensional chiral topological spin textures, such as spin-spirals (a) or skyrmions (b), the non-trivial distribution of the magnetization n gives rise to (a) chiralorbital magnetization (COM), linear in the gradients of n, and to (b) topological orbital magnetization (TOM), which is second order in the gradients of n. Both COM and TOM can exhibit a complex distribution in real space, as illustrated in (a) and (b). For more details see [Lux17].

Nano-structured topologically non-trivial materials

Past year, our primary focus was on prediction of dual topological character in a thin film of a Dirac semimetal, as well as a prediction of a quantum spin Hall effect in hexagonal AFM materials [Niu17a, Niu17b, Niu17c].

(i) Topological materials with both insulating and semimetallic phases can be protected by crystalline (e.g. mirror) symmetry. The insulating phase, called topological crystalline insulator (TCI), has been intensively investigated and observed i n three-dimensional materials. However, the predicted two-dimensional (2D) materials with TCI phase are explored much less than 3D TCIs and 2D topological insulators, while so far considered 2D TCIs almost exclusively possess a square lattice structure with the mirror Chern number C_M =–2. For both 2D TIs and 2D TCIs, the spin-orbit coupling (SOC) is known to play a vital role. In addition, the SOC together with inversion symmetry breaking can lead to coupled spin and valley physics, in which the new degree of freedom offers a promising route to the eventual realization of valleytronic devices. The spin-valley polarization has been observed experimentally in MoS_2 monolayer, which is a topologically trivial insulator. Therefore, a natural question arises as to whether the spin-valley polarization in non-trivial insulators, such as 2D TIs and 2D TCIs, is possible. Recently, thin films of the Dirac semimetal Na_3Bi have been fabricated by molecular beam epitaxy, motivating us to focus on the topological properties of the Na_3Bi monolayer. In our study [Niu17b] we predict theoretically that hexagonal monolayer of Dirac semimetal Na_3Bi is a 2D TCI with a mirror Chern number C_M = –1. We found that the large nontrivial gap of 0.31 eV in this material is tunable and can be made much larger via strain engineering while the topological phases are robust against strain, indicating a high possibility for room-temperature observation of quantized conductance. In addition, we discovered for this compound a nonzero spin Chern number C_S = –1, which indicates the coexistence of 2D topological insulator and 2D TCI in the same material, i.e., we found that Na_3Bi monolayer exhibits the so-called dual topological character. The materials with dual topological character are believed to exhibit a number of fascinating properties. Remarkably, we also revealed a spin-valley polarization in Na_3Bi monolayer due to the breaking of crystal inversion symmetry, which marks this material as a promising candidate for realizing the concepts of topological valleytronics.

(ii) Understanding and utilizing the correlation between magnetism and topology is a key to further advances in topological antiferromagnetic spintronics [Sme17]. This particularly concerns the design and exploitation of magnetic phase transitions for the purpose of shaping global topological properties. However, so far not even the simplest magnetic phase transition from AFM to FM order has been addressed in the context of accompanying changes of the non-trivial bulk topology. Moreover, the realization of diverse magnetic topological phases on a square lattice is very challenging, which obstructs the observation of topological phase transitions driven by the changes in the respective magnetic structure of topologically non-trivial AFM systems considered so far. In sharp contrast to the case of the square lattice, the two-dimensional honeycomb structure as realized in graphene or silicene is known to naturally host a rich spectrum of quantum Hall effects, constituting thus the most favorable platform to uncover the complex interplay between global band topology and magnetic order. In our recent work, based on tight-binding arguments and density functional theory calculations, we predict the emergence of the QSH effect in two-dimensional collinear antiferromagnets with honeycomb lattice structure. Using functionalized tin films X-Sn (where X = H, F, Cl, Br, and I) as prototypical examples, we demonstrate that strain-induced magnetic phase transitions in these systems are accompanied by topological phase transitions from the quantum spin Hall to the QAH insulator, as evidenced by the calculations of the spin and anomalous Hall conductivities, as well as by the analysis of the corresponding gapless edge states. Our findings are crucial for the realization of advanced concepts in topological antiferromagnetic spintronics, and their implementation within "conventional" topological schemes associated up to date exclusively with ferromagnets and non-magnetic materials [Niu17c].

Quota consumed so far by this sub-project constitutes about 20% of the total quota on CLAIX

References

[Han18] HANKE JP, FREIMUTH F, BLÜGEL S, MOKROUSOV Y.
Higher-dimensional Wannier Interpolation for the Modern Theory of the Dzyaloshinskii–Moriya Interaction: Application to Co-based Trilayers. Journal of Physical Society of Japan. 2018;87:041010.

[Han17b] HANKE JP, FREIMUTH F, NIU C, BLÜGEL S, MOKROUSOV Y.
Mixed Weyl semimetals and dissipationless magnetization control in insulators by spin-orbit torques. Nature Communications. 2017;8:1479.

[Fre16b] FREIMUTH F, BLÜGEL S, MOKROUSOV Y.
Laser-induced torques in metallic ferromagnets. Phys. Rev. B. 2016;94:144432.

[Fre17b] FREIMUTH F, BLÜGEL S, MOKROUSOV Y.
Charge pumping driven by the laser-induced dynamics of exchange splitting. Phys. Rev. B. 2017;95:094434.

[Buh17] BUHL PM, FREIMUTH F, BLÜGEL S, MOKROUSOV Y.
Topological Spin Hall effect in Antiferromagnetic Skyrmions. Physica Status Solidi RRL. 2017;11:1700007. (Part of special issue on antiferromagnetic spintronics)

[Hof15] HOFFMANN M, WEISCHENBERG J, DÚPE B, et al.
Phys. Rev. B. 2015;92:020401(R).

[Han16] HANKE JP, FREIMUTH F, NANDY AK, ZHANG H, BLÜGEL S, MOKROUSOV Y.
Role of the Berry phase theory for describing orbital magnetism: from magnetic heterostructures to topological orbital ferromagnets. Phys. Rev. B. 2016;94:121114(R).

[Go17] GO D, HANKE J, BUHL PM, FREIMUTH F, BIHLMAYER G, LEE H, MOKROUSOV Y, BLÜGEL S.
Towards surface orbitronics: giant orbital magnetism from the orbital Rashba effect at the surface of sp-metals. Scientific Reports. 2017;7:46742.

[Han17a] HANKE JP, FREIMUTH F, BLÜGEL S, MOKROUSOV Y.
Prototypical topological orbital ferromagnet γ-FeMn. Sci. Rep. 2017;7:41078.

[Lux17] LUX F, FREIMUTH F, BLÜGEL S, MOKROUSOV Y.
Chiral and Topological Orbital Magnetism of Spin textures.
Under review in Physical Review X. 2018. Attached separately.

[Niu17a] NIU C, BUHL PM, BIHLMAYER G, WORTMANN D, DAI Y, BLÜGEL S, MOKROUSOV Y.
Two-dimensional topological nodal line semimetal in layered X2Y (X = Ca, Sr, and Ba; Y = As, Sb, and Bi). Physical Review B. 2017;95:235138.

[Niu17b] NIU C, BUHL PM, BIHLMAYER G, WORTMANN D, DAI Y, BLÜGEL S, MOKROUSOV Y.
Robust Dual Topological Character with Spin-Valley Polarization in a Monolayer of the Dirac Semimetal Na3Bi. Physical Review B. 2017;95:075404.

[Niu17c] NIU C, HANKE JP, BUHL PM, BIHLMAYER G, WORTMANN D, BLÜGEL S, MOKROUSOV Y.
Quantum Spin Hall Effect and Topological Phase Transitions in Honeycomb Antiferromagnets.
Under review in Physical Review Letters. 2017. Attached separately.

[Sme17] SMEJKAL L, MOKROUSOV Y, YAN B, MACDONALD AH.
Topological Antiferromagnetic Spintronics.
Nature Physics in press. 2018. arXiv: 1706.00670. Attached separately.

Publications:

- ZANOLLI Z, NIU C, BIHLMAYER G, MOKROUSOV Y, MAVROPOULOS P, VERSTRAETE M, BLÜGEL,
  S. Hybrid quantum anomalous Hall effect at graphene-oxide interfaces.
  Physical Review B. 2018;98:155404.
- LUX F, FREIMUTH F, BLÜGEL S, MOKROUSOV Y.
  Engineering Chiral and Topological Orbital Magnetism of Domain Walls and Skyrmions. Communications Physics. 2018;1:60.
- KARNAD G, FREIMUTH F, MARTINEZ E, LO CONTE R, GUBIOTTI G, SCHULZ T, SENZ S, OCKER B, MOKROUSOV Y, KLÄUI M.
  Modification of Dzyaloshinskii-Moriya interaction-stabilized domain wall chirality by driving currents. Physical Review Letters. 2018;121:147203.
- FREIMUTH F, BLÜGEL S, MOKROUSOV Y.
  Spin-orbit torques and tunable Dzyaloshinskii-Moriya interaction in Co/Cu/Co trilayers. Physical Review B. 2018;98:024419.
- SPENCER CS, GAYLES J, PORTER NA, SUGIMOTO S, ASLAM Z, KINANE CJ, CHARLTON TR, FREIMUTH F, CHADOV S, LANGRIDGE S, SINOVA J, FELSER C, BLÜGEL S, MOKROUSOV Y, MARROWS CH.
  Helical magnetic structure and the anomalous and topological Hall effects in epitaxial B20 FeCoGe films. Physical Review B. 2018;97:214406.
- HANKE JP, FREIMUTH F, BLÜGEL S, MOKROUSOV Y.
  Higher-dimensional Wannier Interpolation for the Modern Theory of the Dzyaloshinskii-Moriya Interaction: Application to Co-based Trilayers.
  Journal of Physical Society of Japan. 2018;87:041010.
- FREIMUTH F, BLÜGEL S, MOKROUSOV Y.
  Dynamical and current-induced Dzyaloshinskii-Moriya interaction: Role for damping, gyromagnetism, and current-induced torques in noncollinear magnets. 2018. arXiv:1806.04782
- FENG W, ZHOU Z, HANKE JP, GUO GY, BLÜGEL S, MOKROUSOV Y, YAO Y.
  Topological Magneto-optical effect and its quantization in noncoplanar antiferromagnets. 2018. arXiv:1811.05803

Selected honors

- Master Thesis of supervised master student Fabian R. Lux Topological and Chiral Orbital Magnetism in Two-Dimensional Electronic Solids receives the “INNOMAG Materpreis 2018” for the best master thesis of the year in the field of magnetism at the annual meeting of German Physical Society 2018 in Berlin. The results of this thesis also constitute part of the Abschlussbericht.

Conference Participations

- Mixed semimetals for magnetization and momentum space topology control,
  Y. Mokrousov, Invited Talk at INTERMAG 2018, Singapore, April 2018
- A microscopic perspective at THz spinorbitronics,
  Y. Mokrousov, Invited Talk at International Conference on Magnetism ICM-2018, San Francisco, USA, July 2018
- Shaping skyrmion properties via materials design,
  Y. Mokrousov, Invited Talk at the MRS Fall Meeting, Boston, USA, November 2018

National and international cooperations

- M. KLÄUI, Institute of Physics, Johannes-Gutenberg Universitaet Mainz, Germany
- C. MARROWS, School of Physics and Astronomy, University of Leeds, Leeds, UK
- H. ZHANG, Institute of Materials Science, Technical University of Darmstadt, Germany
- Z. ZANOLLI, Catalan Institute of Nanoscience and Nanotechnology, Barcelona, Spain

Multiplet effects in strongly correlated materials

Project ID: jara0050
EVA PAVARINI
Institute for Theoretical Nanoelectronics (PGI-2) and Institute for Advanced Simulations (IAS-3), FZ Jülich

Electron-electron correlations in real materials are very difficult to describe. The state-of-the-art approach is the DFT+DMFT method, which combines ab-initio approaches based on density-functional theory (DFT) with the dynamical mean-field theory (DMFT), a non-perturbative many-body technique. Although very successful, this method is still limited to specific type of problems and/or few spin-orbital degrees of freedom, and specific type of experiments. The aim of the present proposal was to overcome some of these limitations, with the final goal of making the DFT+DMFT technique as powerful for strongly-correlated systems as DFT already is for weakly-correlated compounds.

We designed an efficient and general DFT+DMFT code, which works for system of any symmetry, general coulomb vertex, general on-site Hamiltonian and which scales almost ideally on massively parallel architectures. It uses several flavors of quantum Monte Carlo as solvers for the DMFT auxiliary quantum impurity problem. With this we could study representative strongly-correlated oxide in a realistic setting, and calculate system-specific properties ranging from photoemission and inverse photoemission spectra, to optical conductivity to magnetic and orbital linear responses.

Representative project-related publications in the years 2016-2018:

[1] SIMS H, PAVARINI E, KOCH E. Phys. Rev. B. 2017;96:054107.
[2] BAUMGAERTEL M, GHANEM K, KIANI A, KOCH E, PAVARINI E, SIMS H, ZHANG G. European Physical Journal Special Topics. 2017;226:252.
[3] ZHANG G, PAVARINI E. Phys. Rev. B. 2017;95:075145.
[4] ZHANG G, GORELOV E, SARVESTANI E, PAVARINI E. Phys. Rev. Lett. 2016;116:106402.
[5] KIANI A, PAVARINI E. Phys. Rev. B. 2016;94:075112.

Visiting scientists at your institute

Our institute, together with the GRS hosts the Autumn School on Correlated Electrons
Local organizers: E. Pavarini (IAS/PGI) and E. Koch (GRS)
You can find the list of lecturers and photos of the school here:
http://www.cond-mat.de/events/correl.html

This school every year attracts internationally very well-known scientists at the FZJ, highly increasing the visibility of the FZJ in the field of strongly correlated materials.

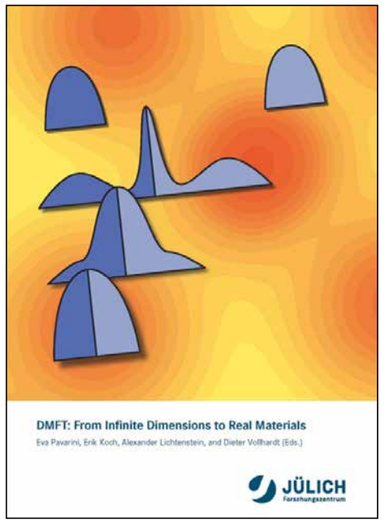

Lecture notes:
Eva Pavarini, Erik Koch, Alexander Lichtenstein, and Dieter Vollhardt (eds.)

DMFT: From Infinite Dimensions to Real Materials Modeling and Simulation, Vol. 8,

Verlag des FZ Jülich, 2018
ISBN 978-3-95806-313-6

DMFT self-consistency loop.

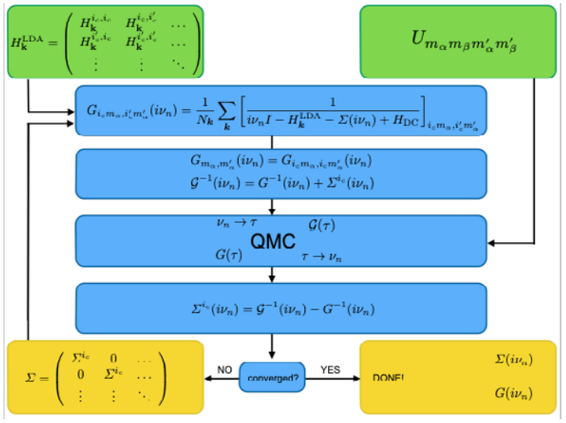

National and international cooperations

- DFG Research Unit Dynamical Mean-Field Approach with Predictive Power for Strongly Correlated Materials (completed)
  http://www.physik.uni-augsburg.de/for1346/
- DFG Research Training Group Quantum many-body methods in condensed matter systems (running)
  http://www.physik.rwth-aachen.de/institute/institut-fuer-theorie-der-statistischen-physik/rtg1995/
- Apart from this we collaborate with several groups in Germany and the rest of the world and we are part of the ICAM/I2CAM international virtual institute.

Ab initio study of amorphous Sb

Project ID: rwth0208
MARTIN SALINGA
I. Institute of Physics (IA),
RWTH Aachen University

IDER RONNEBERGER
Institute for Theoretical
Solid State Physics,
RWTH Aachen University

RICCARDO MAZZARELLO
Institute for Theoretical
Solid State Physics,
Theoretical Nanoelectronics,
RWTH Aachen University

MATTHIAS WUTTIG
I. Institute of Physics (IA),
RWTH Aachen University

Scientific work accomplished and results obtained

Scientific work accomplished and results obtained
The project was divided into 6 work packages (WP's) which address different questions. In the following, we group the WP's according to their specific questions.

WP 1 – System Size Effects: In order to estimate finite size effects, we generated amorphous models of Sb using different system sizes, namely 360, 540 and 720 atoms. We found a significant increase in the crystallization times with larger models (see Figure 1). Therefore, absolute crystallization times cannot be drawn from our simulations. As crystallization occurs in all of our models, we can confidently make qualitative statements about crystallization for models of the same size, e.g. qualitative trends observed in WP3. Further increase of the model size together with improved statistics (averaging over independent samples) would allow for more quantitative statements.

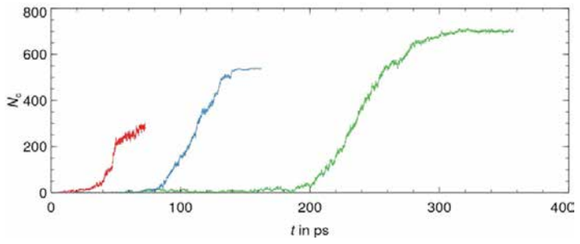

Figure 1: The time evolution of the number of crystalline-like particles of amorphous Sb at 500 K for 360 (red), 540 (blue) and 720 (green) atoms.

WP 2 – Atomic Density: We performed simulations of amorphization and crystallization at two different densities for 360-atom systems. The model with the lower density did not crystallize at room temperature on the simulation time scales and therefore we explored the crystallization behavior at a higher temperature of 500 K. This model crystallized then on a time scale of 400 ps and thus indicates a significant increase in stability (Figure 2).

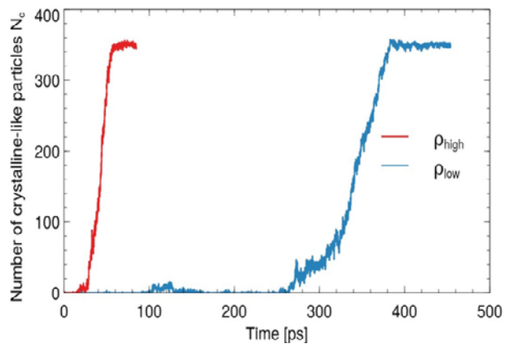

Figure 2: The time evolution of crystallization of a high-density (red) and a low-density (blue) model of 360 Sb atoms at 500 K.

WP 3 – Quenching Rate Effects: We generated amorphous models of Sb with five different quenching rates, namely 3 K ps^{-1}, 9.5 K ps^{-1}, 30 K ps^{-1}, 300 K ps^{-1} and abrupt quenching. The results of the crystallization for this set of models are shown in Figure 3. A clear trend of longer crystallization times with higher quenching rates is observed. This result is remarkable and far from obvious. An in-depth study with more samples would of course improve the statistics and allow for quantitative results. However, the simulation times for this set of simulation were found to be much longer than expected, since the waiting time for the stochastic event of crystallization was unknown. Hence, a larger amount of compute time than originally requested in the project application was needed to finalize this work package.

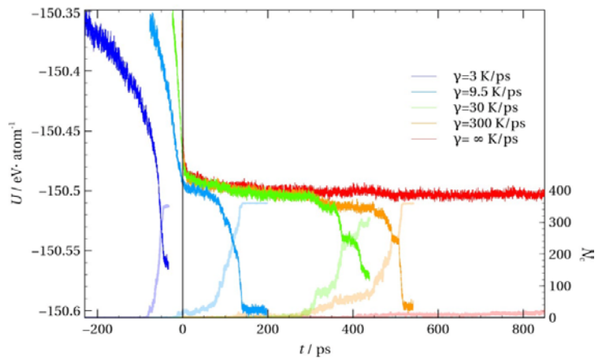

Figure 3: Quenching from the melt of an AIMD model Sb containing 360 atoms. Different colors correspond to different quenching rates (3 K ps^{-1}, purple; 9.5 K ps^{-1}, blue; 30 K ps^{-1}, green; 300 K ps^{-1}, orange; abrupt quenching in a single simulation step, red). For all the models, the target temperature of 300 K is reached at time t = 0 ps. The degree of crystallization is monitored by the number of crystalline-like particles N_c (right axis). Crystallization is accompanied by a drop in potential energy (left axis) below around –150.5 eV per atom. The data clearly show that an increase in the quenching rate hinders crystallization. The simulation with the slowest quenching rate (purple) was aborted before reaching the target temperature as crystallization occurred during quenching.

WP 4 – Crystallization and Aging: We performed some test simulations of crystallization using metadynamics. The crystallization can be accelerated as expected. However, the poor statistics does not allow for conclusive statements at the current stage. The intended set of simulations studying the aging (i.e. long time relaxation) of the amorphous phase has not been carried out yet. It is planned to perform those in the course of a project extension.

WP 5 – Interface effects: We successfully generated an interface model of liquid Sb and amorphous SiO_2 containing 648 atoms. Building such a large and heterogeneous model posed quite a challenge and technical issues. We needed to tweak the numerical parameters in order to get a working thermostat. These preliminary simulations resulted in a significantly higher computational cost. Therefore, we were only able to construct one interface model (other substrate materials or thicker models were not considered). Nevertheless, simulations at high temperatures between 1000 and 4000 K were performed. These showed that on time scales of 50 ps intermixing of Sb and SiO_2 can be excluded at 1000 K and 2000 K whereas intermixing does occur at 3000 K and 4000 K.

WP 6 – Electronic Properties: We relaxed selected configurations from amorphous trajectories at room temperature. Investigation of the electronic properties have not been completed within the duration of this project.

Realization of the project

For the main project on amorphous Sb, we used the simulation package CP2K and used from 72 up to 144 cores depending on the system size.

The realization of the project required extensive preliminary work, in particular for building an interface model which was completely a new ground. We faced a problem related to the thermostat which was solved by increasing the number of self-consistent steps in Kühne's methods [10]. Eventually, we managed to find numerical parameters for building a working model.

No code modifications/improvements have been done.
The granted computing time has been used completely.

Publications in peer-reviewed journals based on results from this project

- SALINGA M, KERSTING B, RONNEBERGER I, JONNALAGADDA VP, VU XT, GALLO ML, GIANNOPOULOS I, COJOCARU-MIRÉDIN O, MAZZARELLO R, SEBASTIAN A. Monatomic phase change memory. Nature Materials. 2018;17:681–685.

Additional references

Website about the EU-funded collaboration between RWTH Aachen University and IBM Zurich Research Laboratory: http://www.iapp-diaspora.eu/index.html

Conference participations

- Invited talk given by M. Salinga at the International Memory Workshop, Monterey, CA, USA, May 13, 2018
- Invited talk given by M. Salinga at the 14th International Conference on Modern Materials and Technologies, Perugia, Italy, June 13, 2018
- Invited talk given by R. Mazzarello at the 2nd Sino-German Workshop on Electronic and Memory Materials, Xi'an, China, September 05, 2018
- Invited talk given by M. Salinga at the 9th International Workshop on Characterization and Modeling of Memory devices, Milano, Italy, September 27, 2018
- Active participation of M. Salinga in the Faraday Discussions of the Royal Society of Chemistry on "New memory paradigms: memristive phenomena and neuromorphic applications", Aachen, Germany, October 16, 2018

Quantum Monte Carlo Studies of Quantum Magnetic Phenomena

Project ID: jara0171

STEFAN WESSEL
Institute for Theoretical Solid State Physics, RWTH Aachen University

In this project we will employ quantum Monte Carlo simulations to study a range of phenomena in quantum magnetism, which are of recent interest in condensed matter physics. As an example, in Phys. Rev. Lett. 122, 127201 (2019), we report from large-scale quantum Monte Carlo simulations to study the Higgs amplitude mode in a planar array of coupled spin ladders, motivated by a recent experimental observation of this Higgs mode in the compound $C_9H_{18}N_2CuBr_4$ (DLCB), which resides close to a quantum critical point. We provided a systematic analysis of the spectroscopy of the magnetic excitations upon tuning the easy-axis anisotropy in the quantum spin system, tuning this way between the classical Ising limit and the full quantum Heisenberg limit. This allowed us to directly identify the nature of the low-energy Higgs mode as a two-magnon bound state that is stabilized in DLCB from decay into the many-magnon continuum. Furthermore, our results allowed for a quantitative theoretical modeling of the neutron scattering data on DLCB. The resulting neutron scattering spectra, transformed to the experimentally relevant scattering setup, is shown in the figure. Further studies of this system under applied pressure, narrowing in onto the quantum critical point, are currently underway, and we extended the quantum Monte Carlo approach to also access this parameter regime.

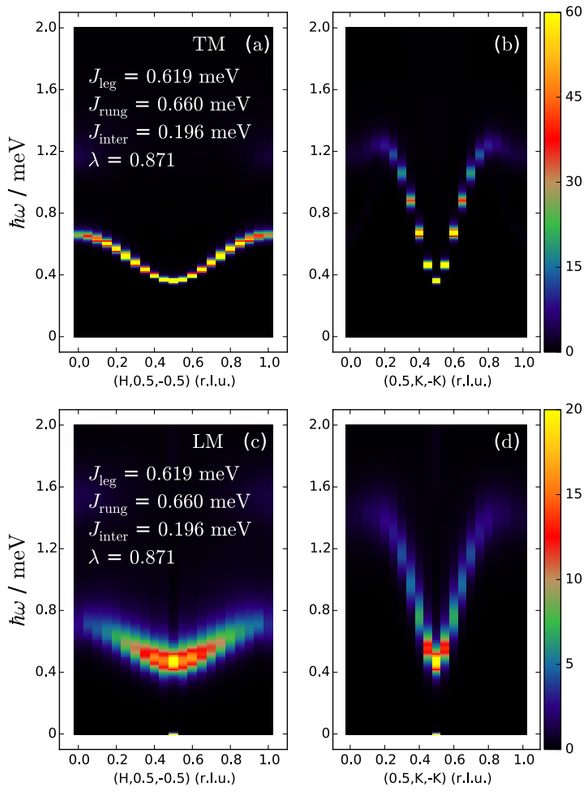

Scattering spectra for DLCB as a function of energy and wave-vector transfer in the transverse (a, b) and longitudinal (c, d) configurations, exhibiting the transverse mode (TM) and longitudinal mode (LM), respectively. The later contains the low-energy gapped Higgs mode excitation. Data based on quantum Monte Carlo simulations for a two-dimensional coupled ladder model with the displayed parameters.

Publications

- YING T, SCHMIDT KP, WESSEL S.
  Higgs mode of Planar Coupled Spin Ladders and its Observation in C9H18N2CuBr4.
  Phys. Rev. Lett. 2019;122:127201.
- EMONTS P, WESSEL S.
  Monte Carlo study of the discontinuous quantum phase transition in the transverse-field Ising model on the pyrochlore lattice.
  Phys. Rev. B. 2018;98:174433.
- WESSEL S, NIESEN I, STAPMANNS J, NORMAND B, MILA F, CORBOZ P, HONECKER A.
  Thermodynamic properties of the Shastry-Sutherland model from quantum Monte Carlo simulations.
  Phys. Rev. B. 2018;98:174432.
- MCDOUGAL D, GIBBS AS, YING T, WESSEL S, WALKER HC, VONESHEN D, MILA F, Takagi H, Coldea R. Spin dynamics of coupled spin ladders near quantum criticality in Ba2CuTe06.
  Phys. Rev. B. 2018;98:174410.
- STAPMANNS J, CORBOZ P, MILA F, HONECKER A, NORMAND B, WESSEL S.
  Thermal Critical Points and Quantum Critical End Point in the Frustrated Bilayer Heisenberg Antiferromagnet.
  Phys. Rev. Lett. 2018;121:127201.
- WEBER L, PARSEN TOLDIN F, WESSEL S.
  Critical Edge States of Two-Dimensional Quantum Critical Magnets.
  Phys. Rev. B. 2018;98:140403(R).
- HESSELMANN S, SCHERER DD, SCHERER MM, WESSEL S.
  Bond-ordered states and f-wave pairing of spinless fermions on the honeycomb lattice.
  Phys. Rev. B. 2018;98:045142.
- BECKER J, WESSEL S.
  Diagnosing Fractionalization from the Spin Dynamics of Z2 Spin Liquids on the Kagome Lattice by Quantum Monte Carlo.
  Phys. Rev. Lett. 2018;121:077202.

Conference participation

- S. WESSEL,
  "Quantum Monte Carlo in the spin-dimer basis", 673.
  Wilhelm und Else Heraeus-Seminar "Trends in Quantum Magnetism",
  June 4-8, 2018, Physikzentrum Bad Honnef, Germany

National and international cooperations

- P. CORBOZ, University of Amsterdam, The Netherlands
- F. MILA, EPFL Lausanne, Switzerland
- A. HONECKER, Université de Cergy-Pontoise, France

Particles, Nuclei & Fields | DFG 309

Massive current–current correlators in thermal QCD

Summary

During the project period we finalized a set of simulations permitting to carry out a continuum extrapolation of massive current-current correlators at finite temperature in quenched QCD. Four different lattice spacings, for each of them several temperatures, for each of them six different bare quark masses were simulated, in order to permit for an analysis at a fixed physical quark mass. A successful continuum extrapolation was subsequently carried out. This project extends the previous study in the pseudo-scalar channel to the vector channel of charmonium and bottomonium spectral functions and transport coefficients.
The project period represents the culmination of a multiyear effort aimed at carrying out a continuum extrapolation for massive current-current correlators in thermal quenched QCD. The main steps have been demonstrated to be realizable in practice and lead to systematic errors on a ≲ 5% level. This turns out to be sufficient for drawing highly non-trivial physics conclusions on the quark-gluon plasma that is being generated in the current generation of heavy ion collision experiments, with the heavy quarks serving as both a theoretically and experimentally well-controlled probe of the thermodynamic and transport properties of this system.
Based on the knowledge obtained in the quenched approximation over the past years, in the project period we have performed first calculations using gauge field configurations from 2+1-flavor simulations with physical dynamical quarks as a first step to extend the studies of spectral and transport properties to the realistic full QCD set-up. Although these studies are still limited to rather small lattices, the results will allow for a first analysis of the effect of dynamical light quark degrees of freedom.

Project ID: bund0001
OLAF KACZMAREK
Faculty of Physics,
Universität Bielefeld

Publications

[1] SANDMEYER H.
Hadronic correlators from heavy to very to very light quarks.
PhD-thesis 2019 at University of Bielefeld. doi:10.4119/unibi/2936264.

[2] DING HT, KRUSE AL, DING HT, KACZMAREK O, OHNO H, SANDMEYER H.
Insight into Thermal Modifications of Quarkonia From a Comparison of Continuum-Extrapolated Lattice Results to Perturbative QCD.
MDPI Proc. 2019;10,no.1:45. doi:10.3390/proceedings2019010045. arXiv:1901.04226.

[3] DING HT, ET AL.
Charmonium and bottomonium spectral functions in the vector channel. Nucl. Phys. A. 2019;982:715. doi:10.1016/j.nuclphysa.2018.09.075. arXiv:1807.06315.

[4] RAPP R, ET AL.
Extraction of Heavy-Flavor Transport Coefficients in QCD Matter.
Nucl. Phys. A. 2018;979:21. doi:10.1016/j.nuclphysa.2018.09.002. arXiv:1803.03824.

[5] DING HT, KACZMAREK O, MUKHERJEE S, OHNO H, SHU HT.
Stochastic reconstructions of spectral functions: Application to lattice QCD.
Phys. Rev. D. 2018;97,no.9:094503. doi:10.1103/PhysRevD.97.094503. arXiv:1712.03341.

[6] DING HT, KACZMAREK O, KRUSE AL, OHNO H, SANDMEYER H.
Continuum extrapolation of quarkonium correlators at non-zero temperature.
EPJ Web Conf. 2018;175:07010. doi:10.1051/epjconf/201817507010. arXiv:1710.08858.

[7] DING HT, KACZMAREK O, KRUSE AL, MUKHERJEE S, OHNO H, SANDMEYER H, SHU HT.
Thermal modifications of charmonia and bottomonia from spatial correlation functions. EPJ Web Conf. 2018;175:07021. doi:10.1051/epjconf/201817507021. arXiv:1710.08587.

[8] BURNIER Y, DING HT, KACZMAREK O, KRUSE AL, LAINE M, OHNO H, SANDMEYER H.
Thermal quarkonium physics in the pseudoscalar channel.
JHEP. 2017;1711:206. doi:10.1007/JHEP11(2017)206. arXiv:1709.07612.
[9] AARTS G, ET AL.
Heavy-flavor production and medium properties in high-energy nuclear collisions - What next?.
Eur. Phys. J. 2017;A53:93. 1612.08032.
[10] KACZMAREK O.
Lattice QCD results on soft and hard probes of strongly interacting matter.
Nucl. Phys. 2017;A967:137. doi:10.1016/j.nuclphysa.2017.05.106. arXiv:1705.10682.

Conference participations

- The 27th International Conference on Ultrarelativistic Nucleus-Nucleus Collisions (Quark Matter 2018), Venice, Italy, May 13-19, 2018
- QCD in eXtreme conditions (XQCD2018), Frankfurt, Germany, May 21-23, 2018
- The 36th Annual International Symposium on Lattice Field Theory (Lattice 2018), East Lansing, MI, USA, July 22-28, 2018
- XIIIth Conference on Quark Confinement and the Hadron Spectrum Invited Talk on Spectral and transport properties from Lattice QCD, Maynooth, Ireland, July 31 - August 2, 2018
- Hot Quarks, Texel, Netherlands, September 2018
- International workshop on High Performance Computing in High Energy Physics Co-organizer and talk on Heavy Quarks in a Quark Gluon Plasma, CCNU Wuhan, China, September 19-21, 2018

National and International cooperations

- Heng-Tong Ding, CCNU Wuhan, China
- Mikko Laine, University of Bern, Switzerland
- Hiroshi Ohno, University of Tsukuba, Japan
- Swagato Mukherjee, Brookhaven National Lab, USA

Nuclear Lattice Simulations

Project ID: hfz02 - project #11684, jara0015 - project #11784

ULF-G. MEISSNER
Institute for Nuclear Physics, Theory of the strong interactions (IKP-3 / IAS-4), FZ Jülich

SERDAR ELHATISARI
Helmholtz-Institut für Strahlen- und Kernphysik (Theorie) and Bethe Center for Theoretical Physics, Rheinische Friedrich-Whilhelms University Bonn

EVGENY EPELBAUM
Hermann Krebs, Institute of Theoretical Physics II, Ruhr-Universität Bochum

TIMO A. LÄHDE
THOMAS LUU
Institut für Kernphysik, Institute for Advanced Simulation, and Jülich Center for Hadron Physics, FZ Jülich

DEAN LEE
NING LI, BINGNAN LU
Facility for Rare Isotope Beams and Department of Physics and Astronomy, Michigan State University

GAUTAM RUPAK
Department of Physics & Astronomy, Mississippi State University

Scientific work accomplished and results obtained

N3LO interactions for nuclear structure and scattering

We have constructed and fitted to available low-energy data, chiral two-nucleon and three-nucleon interactions on the lattice up to next-to-next-to-next-to-leading order (N3LO). We have obtained results for the two-nucleon interactions up to N3LO, for a spatial lattice spacing of a = 1.97 fm. At such low cutoff momentum (π/a = 314 MeV), the structure of the two-pion exchange interaction is not resolved, and it can be reduced to a contact interaction. Due to the underlying symmetries, no new two-nucleon terms appear at order N2LO in this simplified scheme. We show the neutron-proton phase shifts versus relative momentum for one choice of local and non-local smearing parameters. In Fig. 1, we present the results at LO, NLO, N2LO, and N3LO, and the comparison with the Nijmegen partial wave analysis (NPWA) of experimental data [1]. The coupled-channel phase shifts are computed on the lattice using the properties of spherical standing waves, as described in Ref. [2]. The extension to smaller lattice spacings that requires inclusion of the unexpanded two-pion exchange, is in progress.

We are in the process of benchmarking these interactions using projection Monte Carlo simulations of the helium, beryllium, carbon, and oxygen isotopes. At the same time, we are also performing adiabatic projection calculations [3, 4] of the α-^{12}C scattering phase shifts, and computing the asymptotic normalization coefficients of ^{16}O bound states. We expect this work to be completed within the next month.

Eigenvector continuation

A common challenge faced in many branches of quantum physics is finding the extremal eigenvalues and eigenvectors of a Hamiltonian matrix, which is too large to store in computer memory. There are numerous efficient methods developed for this task, but they generally fail when

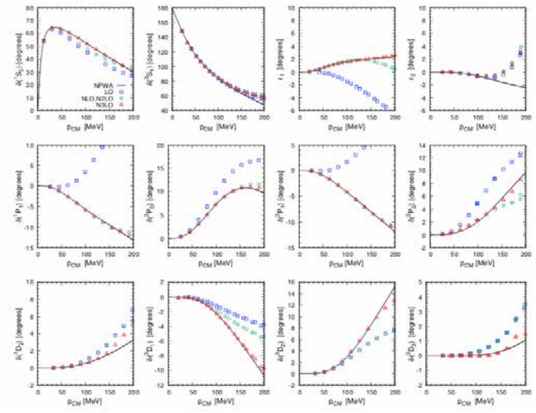

Figure 1: Neutron-proton scattering phase shifts and mixing angles in NLEFT, as a function of relative center-of-mass momentum at LO, NLO, N2LO, and N3LO. For comparison, we show the Nijmegen partial wave analysis (NPWA) of experimental data. First row: S-wave phase shifts $^1S_0$ and $^3S_1$ and mixing angles ε_1 and ε_2. Second row: Phase shifts for the P-wave channels $^1P_1$, $^3P_0$, $^3P_1$, and $^3P_2$. Third row: Phase shifts for the D-wave channels $^1D_2$, $^3D_1$, $^3D_2$, and $^3D_3$.

some control parameter in the Hamiltonian matrix (such as interaction coupling) exceeds some threshold value. In Ref. [5], we present a new technique called “eigenvector continuation”, that can extend the reach of these methods in such problematic cases. The key insight is that while an eigenvector may reside in a linear space of enormous dimension, the effective dimensionality of the eigenvector trajectory traced out by the one-parameter family of Hamiltonian matrices is much smaller. This statement is proven using analytic

function theory, and the eigenvector continuation method is introduced to solve for the extremal eigenvectors.

We used eigenvector continuation to calculate the ground state energy of neutron matter for a computationally difficult LO lattice action. In this lattice action, the repulsive part of the one-pion exchange interaction at short distances produces severe Monte Carlo sign oscillations that render accurate simulations impossible. We considered the ground state energies for 6 and 14 neutrons on a 4 × 4 × 4 lattice with spatial lattice spacing 1.97 fm. We used projection Monte Carlo with auxiliary fields to calculate the ground state energy.

At first, we attempted to compute the ground state energies directly, but the errors were quite large due to sign oscillations. For 6 neutrons, the ground state energy is $E_0=12(^{+3}_{-4})$ MeV, and for 14 neutrons $E_0=42(^{+7}_{-15})$ MeV. Next, we used eigenvector continuation (EC) for the same systems where the square of the axial vector coupling is reduced in magnitude, $g_A^2=\{c_1, c_2, c_3\}$, where $c_1 = 0.25$, $c_2 = 0.60$, and $c_3 = 0.95$. We used projection Monte Carlo simulations to calculate the ground state eigenvectors for $\{c_1, c_2, c_3\}$. The schematic drawing in Fig. 2 shows the overall setup of the calculations. Starting with an initial state $|\psi_{int}\rangle$, we projected forward in Euclidean time using a lattice Hamiltonian $H(c_k)$, where $g_A^2=c_K$. For large Euclidean time, this produces a state proportional to the ground state of $H(c_k)$. Starting from a final state $|\psi_{int}\rangle$, we projected backward in Euclidean time using a lattice Hamiltonian $H(c_{k'})$ with $g_A^2=c_{k'}$. For large Euclidean time, this produces a state proportional to the ground state of $H(c_{k'})$. The matrix of amplitudes $N_{k',k}$ is the inner product between these ground state projections for $H(c'_k)$ and $H(c_k)$. The matrix of amplitudes $H_{k',k}$ is the same as $N_{k',k}$, except that the Hamiltonian $H(c_\odot)$ is inserted in the middle time step, where $c_\odot$ is the physical value of g_A^2. We then solved the generalized eigenvalue problem by calculating the ground state of $N^{-1/2}HN^{-1/2}$.

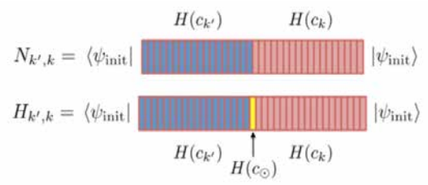

Figure 2: The matrix of amplitudes $N_{k',k}$ is the inner product between ground state projections for H ($c_{k'}$) and H (c_k). The matrix of amplitudes $H_{k',k}$ is the same as $N_{k',k}$ except that the Hamiltonian $H(c_\odot)$ is inserted in the middle time step, where $c_\odot$ is the physical value of g_A^2.

In Table 1, we show the EC results using just one of the three vectors, two of the three vectors, or all three vectors. The errors given are estimates of the stochastic and extrapolation errors when taking the limit of infinite projection time. For comparison, we also show the results of a direct calculation. We see that EC converges quite rapidly with the number of vectors included. The EC results are also consistent with the direct calculation, though the error of the EC method is smaller by an order of magnitude.

g_A^2 values	E_0, 6 neutrons (MeV)	E_0, 14 neutrons (MeV)
c_1	13.8(1)	48.9(4)
c_2	13.6(2)	48.4(5)
c_3	13.6(2)	48.9(6)
c_2, c_3	13.6(2)	48.1(6)
c_3, c_1	13.6(2)	48.9(6)
c_1, c_2	13.6(2)	48.0(6)
c_1, c_2, c_3	13.6(2)	48.0(6)
direct calculation	$12(^{+3}_{-4})$	$42(^{+7}_{-15})$

Table 1: Eigenvector continuation (EC) results for the ground state energy for 6 and 14 neutrons using sampling data $g_A^2=c_1$, c_2, c_3, where $c_1 = 0.25$, $c_2 = 0.60$, and $c_3 = 0.95$. For comparison, we also show the results of a direct calculation.

Pinhole trace algorithm

In order to simulate many-body systems at non-zero temperature, one must compute the partition function Z=Tr exp(-ßH), where ß is the inverse of the temperature T. Standard approaches to computing the partition function use the grand canonical ensemble [6]. Unfortunately, the standard approach requires calculating the determinants of matrices of size (4V) × (4V), where V is the number of spatial lattice points in the spatial volume. Since the determinants must be calculated for every configuration of the auxiliary fields, the computational cost may become prohibitively high.

We have developed a new approach called the “pinhole trace algorithm” that solves this computational cost issue. We simply work in the canonical ensemble and compute the trace of A-nucleon states in position space,

$$\mathrm{Tr}\mathcal{O} = \frac{1}{A!}\sum_{i_1\ldots i_A}\sum_{j_1\ldots j_A}\sum_{n_1\ldots n_A}\langle 0|a_{i_A,j_A}(n_A))\ldots a_{i_1,j_1}(n_1)\,\mathcal{O}\,a^\dagger_{i_1,j_1}(n_1)\ldots a^\dagger_{i_A,j_A}(n_A)|0\rangle, \quad (1)$$

where $a_{I_K,j_K}(n_K)$ is the annihilation operator for a nucleon with spin i_k, isospin j_k, and position n_k. This approach reduces the matrices to size A × A, and the resulting computational cost savings are very significant. We find a computation cost reduction factor ranging from ~ 10^3 to ~ 10^6. Furthermore, sign oscillations remain under control even at low T, due to pairing interactions between nucleons.

In Fig. 3, we show the ^{12}C matter density versus radial distance from center of mass several values of T, for simulations in a cubic periodic box of length 8 fm. We see that as T > 2.0 MeV, ^{12}C starts to develop an extended tail in the density distribution. This is most likely due to the “boiling” of alpha particles from the ^{12}C nucleus.

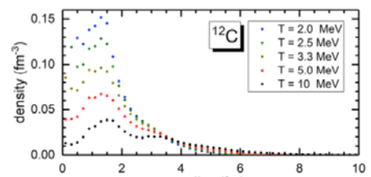

Figure 3: The matter density of ^{12}C as a function of radial distance from the center of mass, for various temperatures T.

In Fig. 4, we show the average energy of ^{12}C as a function of T in the top panel, and the heat capacity of ^{12}C as a function of T in the bottom panel. We find a peak in the heat capacity near T = 2.5 MeV, which we again interpret as being associated with the boiling of alpha particles from the nucleus. These simulations were performed in a periodic box of length 12 fm.

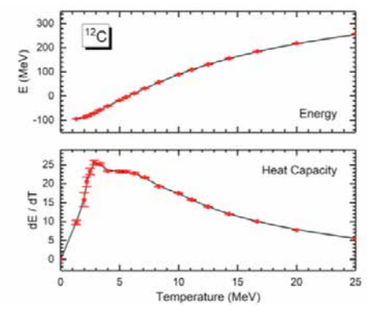

Figure 4: Top panel: Average energy of ^{12}C as a function of T. Bottom panel: Heat capacity of ^{12}C as a function of T.

References

[1] STOKS VGJ, KOMPL RAM, RENTMEESTER MCM, DE SWART JJ.
Partial wave analysis of all nucleon-nucleon scattering data below 350-MeV. Phys. Rev. 1993;C48:792–815.

[2] LU BN, LÄHDE TA, LEE D, MEISSNER UG.
Precise determination of lattice phase shifts and mixing angles. Phys. Lett. 2016;B760:309–313.

[3] ELHATISARI S, LEE D, RUPAK G, EPELBAUM E, KREBS H, LÄHDE TA, LUU T, MEISSNER UG.
Ab initio alpha-alpha scattering. Nature. 2015;528:111.

[4] ELHATISARI S, LEE D, MEISSNER UG, RUPAK G.
Nucleon-deuteron scattering using the adiabatic projection method. Eur. Phys. J. 2016;A52,no.6:174.

[5] FRAME D, HE R, IPSEN I, LEE D, LEE D, RRAPAJ E.
Eigenvector continuation with subspace learning. 2017.

[6] LEE D, BORASOY B, SCHÄFER T.
Nuclear lattice simulations with chiral effective field theory. Phys. Rev. 2004;C70:014007.

Publications with the appropriate acknowledgement

Below, we list some of the relevant publications and preprints related to the work performed during this funding period.

- FRAME D, HE R, IPSEN I, LEE D, RRAPAJ E.
  Eigenvector continuation with subspace learning.
  arXiv:1711.07090. Submitted for publication.
- FREER M, HORIUCHI H, KANDA-EN'YO Y, LEE D, MEISSNER UG.
  Microscopic Clustering in Light Nuclei. arXiv:1705.06192. Submitted for publication.
- KÖNIG S, LEE D.
  Volume Dependence of N-body Bound States. Phys. Lett. B. 2018;779:9.
- ELHATISARI S, EPELBAUM E, KREBS H, LÄHDE TA, LEE D, LI N, LU BN, MEISSNER UG, RUPAK G.
  Ab initio calculations of the iso-topic dependence of nuclear clustering.
  Phys. Rev. Lett. 2017;119:222505.
- ALARCON JM, DU D, KLEIN N, LÄHDE TA, LEE D, LI N, LU BN, LUU T, MEISSNER UG.
  Neutron-proton scattering at next-to-next-to-leading order in Nuclear Lattice Effective Field Theory. Eur. Phys. J. 2017;A53:83.
- LÄHDE TA, MEISSNER UG.
  Nuclear Lattice Effective Field Theory. Lecture Notes in Physics. Springer Verlag. 2019;vol.957:1-396. https://link.springer.com/book/10.1007%2F978-3-030-14189-9.

Ab initio calculations of the isotopic dependence of nuclear clustering

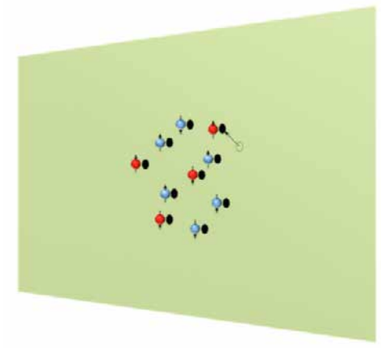

Figure 5: An opaque sheet allowing particles to pass only at chosen pinhole locations. The pinhole locations are sampled by the Metropolis algorithm, in order to obtain the particle distribution.

Selected honors

- ULF-G. MEISSNER, Distinguished Scientist Award from the Chinese Academy of Sciences within the CAS President's International Fellowship Program, 2018
- Ulf-G. Meißner, Honorary Doctorate from the Ivane Javakhishvili Tbilisi State University, Tiflis, Georgien

Selected conference participations

- ULF-G. MEISSNER, ``Another walk through the world of chiral dynmaics,'' opening talk, Ninth International Workshop on Chiral Dynamics, Duke University, Durham, USA, August 2018

National and international cooperations

- DEAN LEE, Facility for Rare Isotope Beams (FRIB), Michigan, USA
- SERDAR ELHATISARI, Karamanoglu Mehetbey Univ., Karaman, Türkey
- BING-NAN LU, Graduate School of China Academy of Engineering Physics, Beijing, China

Astrophysics & Astronomy | DFG 311

Absolute Energy Calibration of the Pierre Auger Observatory using Radio Emission of Extensive Air Showers

Project ID: rwth0203
MARTIN ERDMANN
Experimental Physics (High Energy Physics), Physics Institute III A, RWTH Aachen University

Ultra-high energy cosmic rays hitting the Earth atmosphere can be measured through the detection of radio-frequency radiation from air showers. The radio-frequency emission originates from deflections of the air-shower particles in the geomagnetic field and from a time-varying negative charge excess in the shower front. The distribution of the radio signal on the ground contains information on crucial cosmic-ray properties, such as energy and mass. We used the HPC resources to produce high-precision simulations of the radio emission of air showers that were used to derive the relation between the measurable energy in the radio signal and the energy of the primary cosmic ray.

Furthermore, we addressed the long-standing challenge to access this information experimentally with a sparse grid of antennas. We present a new analytic model of the radio signal distribution that depends only on the definition of the shower axis and on the parameters energy and distance to the emission region. This new analytic model describes the different polarizations of the radiation and therefore allows the use of independently measured signals in different polarization, thereby doubling the amount of information that is available in current radio arrays, compared to what has been used thus far. We show with the use of simulations that fitting the measurements with our model does not result in significant contributions in both systematic bias and in resolution for the extracted parameters energy and distance to emission region, when compared to the expected experimental measurement uncertainties. This parametrization also enables fast simulation of radio signal patterns for cosmic rays, without the need to simulate the air shower.

Publications

[1] GLASER C, DE JONG S, ERDMANN M, HÖRANDEL J.
An analytic description of the radio emission of air showers based on its emission mechanisms. Astroparticle Physics. 2018;08:004. arXiv:1806.03620.

Selected honors

- Dissertation Price of the Friedrich Wilhelm Stiftung 2018: Christian Glaser, Absolute Energy Calibration of the Pierre Auger Observatory using Radio Emission of Extensive Air Showers, RWTH library https://publications.rwth-aachen.de/record/686745 .
- Christian Glaser, Nomination for the dissertation award of the German Physical Society (DPG), one out of four final candidates, invited plenary talk at spring meeting DPG 2018 in Würzburg

Selected national and international cooperations

- The Pierre Auger Observatory: the international collaboration on ultra-high energy cosmic rays prepares for a journal publication on the absolute energy measurement of cosmic rays using radio emission of air showers. This work relies on the results obtained with the RWTH HPC cluster published in the journal publication below. Publication: C. GLASER, S. DE JONG, M. ERDMANN, J. HÖRANDEL, An analytic description of the radio emission of air showers based on its emission mechanisms, Astroparticle Physics 08 (2018) 004, arXiv:1806.03620

Cosmic-Ray physics with the AMS experiment on the international space station

Project ID: jara0052
HENNING GAST
STEFAN SCHAEL
I. Physics Institute B,
RWTH Aachen University

© NASA

AMS is a detector designed for precision spectroscopy of cosmic rays that was installed on the International Space Station in May 2011 (Fig. 1). With dimensions of 5x4x3 m^3 and a weight of 7.5 tons, AMS is the largest cosmic-ray spectrometer ever built. Its construction began in 1995, and a successful prototype flight aboard the Space Shuttle Discovery proved the feasibility of the detector concept in 1998. Led by Nobel laureate Professor Samuel Ting from MIT, AMS has been constructed and is now operated by an international collaboration of more than 200 scientists and engineers, from Europe, America and Asia. The overall construction costs, including the flight of AMS to the Space Station aboard Space Shuttle Endeavour, have amounted to 1.5 billion US dollars. In Germany, RWTH Aachen University has been strongly involved in the AMS project since its inception. One of the main components of AMS, the transition radiation detector (TRD), has been designed and constructed by the I. Physikalisches Institut B under the direction of Professor Stefan Schael. Today, the Aachen group, comprising 20 scientists and students, plays a major role in the analysis of the data gathered by AMS and in the operation and calibration of the instrument.

Since their discovery in 1912, cosmic rays have held many surprises in stock for us, from the discovery of new elementary particles to the most violent processes taking place in the Universe and accelerating cosmic rays to enormous energies. As a multi-purpose instrument for the precision spectroscopy of cosmic rays, AMS was conceived to answer fundamental questions about our Universe: What is the nature of Dark Matter? What happened to the antimatter that must have been produced in the Big Bang? Where are cosmic rays accelerated and how do they propagate through the Milky Way? Answers to these questions will have a profound impact on our understanding about the inner workings of our Universe and help advance fundamental science. In particular, the search for dark matter complements the endeavour to search for new elementary particles at the Large Hadron Collider (LHC) at CERN, Geneva.

AMS so far has recorded more than 125 billion individual particle crossings (so called “events“). The raw data volume collected is on the order of 40 TB per year. AMS employs three different sub-detectors for particle identification (the TRD, an electromagnetic calorimeter and a ring-imaging Cherenkov counter) and two sub-detectors for energy or momentum measurements (a silicon tracker and a time-of-flight system). Before any physics analysis of the data can be performed, the information from all these subdetectors has to be pieced together and complicated reconstruction algorithms have to be run for each of them. The resulting high-level data serves as the input for physics analyses and occupies a volume of 160 TB per year of AMS flight on disk. Several processing runs of AMS data have already been conducted successfully on the JUROPA and JUAMS clusters at JSC as the result of the cooperation within JARA.

So far, fourteen publications from the AMS collaboration have appeared in the renowned Physical Review Letters. The findings have received considerable attention among astrophysicists and triggered an enormous amount of theoretical work.

In 2018, the Aachen group has led the publication on the discovery of complex time structure in the fluxes of cosmic-ray positrons and electrons in Physical Review Letters. The paper was chosen as an “Editor’s Suggestion” for its outstanding quality and relevance. The data cover the time range from May 2011 to May 2017 and the energy range from 1 to 50 GeV. Results for five characteristic energy bins are shown in Fig. 2. They show a rich time structure of the fluxes. The ratio of the positron flux to the electron flux, shown in Fig. 3, reveals a long-term trend, namely a smooth transition from one constant value to another, roughly one year after the polarity reversal of the heliospheric magnetic field that took place in the year 2013. This behaviour is caused by charge-sign dependent solar modulation effects.

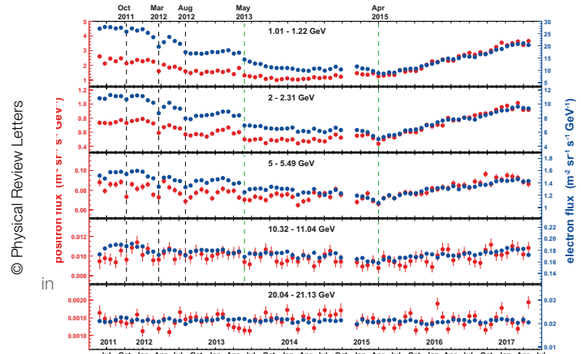

© Physical Review Letters

Figure 2: Fluxes of cosmic-ray positrons (red, left axis) and electrons (blue, right axis) as functions of time, for five selected energy ranges. Prominent and distinct time structures visible both the positron spectrum and the electron spectrum and

in

at

different energies are marked by dashed vertical lines.

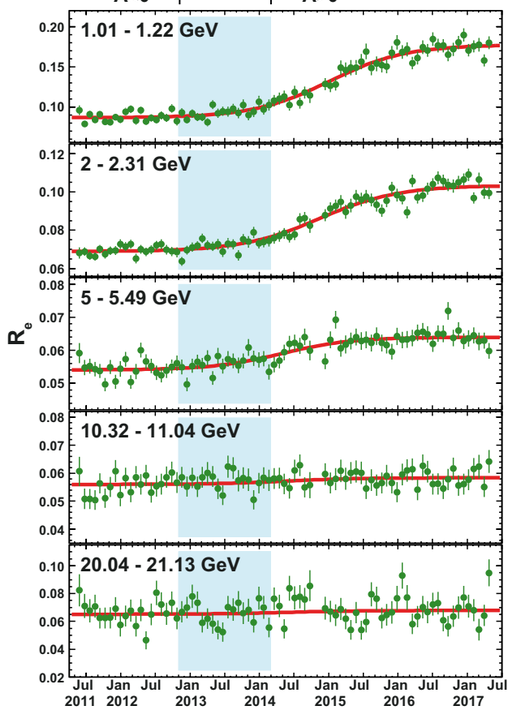

© Physical Review Letters

Figure 3: The ratio of the positron flux to the electron flux as a function of time. The data are parameterized by smooth red curves. The polarity of the heliospheric magnetic field changed from negative (A < 0) to positive (A > 0) during the year 2013. The period without well-defined polarity is marked by the shaded area. The observed behaviour is caused by charge-sign dependent solar modulation effects.

Publications

- AGUILAR M, ET AL.
  Observation of New Properties of Secondary Cosmic Rays Lithium, Beryllium, and Boron by the Alpha Magnetic Spectrometer on the International Space Station.
  Physical Review Letters. 2018;120:021101.
- AGUILAR M, ET AL.
  Observation of Complex Time Structures in the Cosmic-Ray Electron and Positron Fluxes with the Alpha Magnetic Spectrometer on the International Space Station.
  Physical Review Letters. 2018;121:051102.
- AGUILAR M, ET AL.
  Observation of Fine Time Structures in the Cosmic Proton and Helium Fluxes with the Alpha Magnetic Spectrometer on the International Space Station.
  Physical Review Letters. 2018;121:051101.
- AGUILAR M, ET AL.
  Precision Measurement of Cosmic-Ray Nitrogen and its Primary and Secondary Components with the Alpha Magnetic Spectrometer on the International Space Station. Physical Review Letters. 2018;121:051103.

Conference participations

- S. SCHAEL,"The first six years of AMS on the International Space Station", Colloquium, GSI, Darmstadt, Germany, January 09, 2018
- S. SCHAEL, "AMS Positron and Electron Results I", AMS Days, La Palma, Spain, April 09-12, 2018
- S. SCHAEL, "The next generation AMS experiment", AMS Days, La Palma, Spain, April 09-12, 2018
- H. GAST, "Observation of complex time structures in the cosmic-ray electron and positron fluxes", AMS Days, La Palma, Spain, April 09-12, 2018
- S. SCHAEL, "The First Six years of AMS on the International Space Station", Colloquium MPI für Physik, München, Germany, April 24, 2018
- H. GAST, "Latest results from the AMS Experiment on the International Space Station",ECAP, Erlangen, Germany, May 23, 2018
- S. SCHAEL, "Latest Results from the AMS Experiment", COSPAR 2018, Invited Plenary talk, Pasadena, California, USA, July 14-22, 2018
- S. SCHAEL, "Observation of complex time structures in the cosmic ray electron and positron fluxes with the Alpha Magnetic Spectrometer on the ISS", COSPAR 2018, Invited talk, Pasadena, California, USA, July 14-22, 2018
- S. SCHAEL, "New Results from the AMS Experiment on the ISS", WE-Heraeus Symposium, Physikzentrum Bad Honnef, Germany, October 29-31, 2018

National and international cooperations

- SAMUEL C. C. TING, Massachusetts Institute of Technology, USA
- BRUNA BERTUCCI, INFN and University of Perugia, Italy
- BERND HEBER, Christian-Albrechts-Universität zu Kiel, Germany
- IRIS GEBAUER, Karlsruhe Insitute of Technology, Germany

Data analysis and simulations for future and current cosmological experiments

Planck satellite

The ESA Planck satellite has given its final results for the map of Cosmic Microwave Background (CMB) anisotropies in 2018. To interpret the data, we have run millions of simulations of the Universe, for various cosmological models and for different values of their physical parameters. A comparison of the simulations with real data has shown which models and parameters are compatible with the Planck picture of our baby Universe. Our result have played an important role for the writing of two very important papers that condense the current knowledge of the physics community on the Universe in which we leave. These two official Planck collaboration papers, [5] and [6], already gathered over 1500 citations combined. Among the most important results derived from runs performed at RWTH we can mention our detailed reconstruction of the dynamics of inflation, a mechanism that occurred 13.8 billion years ago when our whole observable universe was as small as a foot ball, or our new bounds on the annihilation rate of Dark Matter particles, or also some new consistency checks between two types of crucial cosmological observations: primordial element abundances and CMB maps.

Forecasts for future cosmological experiments

Our technology for generating millions of cosmological simulations and fitting them to observations can be applied to mock data, i.e. fake data sharing the characteristics of future experiments. This allows to predict the sensitivity of future experiments to various parameters and effects. Such information is crucial in order to design and optimize these experiments. In [3] we used the RWTH cluster to test and improve the numerical tools that simulate the sensitivity of two future experiments in which Germany will actively participate: the Euclid ESA satellite, and the Square Kilometer Array (SKA) telescope. In [4] we presented a massive grid of sensitivity forecasts for 35 different combinations of future cosmological experiments. Our most striking result is a detailed and robust proof that even under the most pessimistic assumptions, future cosmological experiments will detect the mass of neutrinos, with a confidence level that will gradually rise up to 98%. A more specialized paper [2] showed that these conclusions are true even when one models the effect of neutrino masses on the cosmological evolution at a higher degree of realism than before.

Markov Chain Monte Carlo for cosmology

The work mentioned in the previous two paragraphs relies on a Markov Chain Monte Carlo (MCMC) exploration of the parameter space of cosmological models. We perform this exploration using a numerical pipeline that we developed ourselves over the years and distribute to the community. This pipeline is used on hundreds of other HPC clusters across the world. New ideas to boost its efficiency are continuously required. In [1] we used the RWTH cluster to develop and test a new method – an adaptive Metropolis-Hastings algorithm – that allowed us to increase the performance of our MCMC sampler by one order of magnitude.

Project ID: rwth0113

JULIEN LESGOURGUES
Institute for Theoretical Particle Physics Cosmology, RWTH Aachen University

SEBASTIEN CLESSE
Department of Mathematics, University of Namur, Belgium

MARIA ARCHIDIACONO
Department of Physics and Astronomy, University of Bologna, Italy

ALESSANDRO CUOCO
Department of Physics and Astronomy, Aarhus University, Denmark

DEANNA HOOPER
Institute for Theoretical Particle Physics and Cosmology, RWTH Aachen University

THEJS BRINCKMANN
TIM SPRENGER
SEBASTIAN BOHR

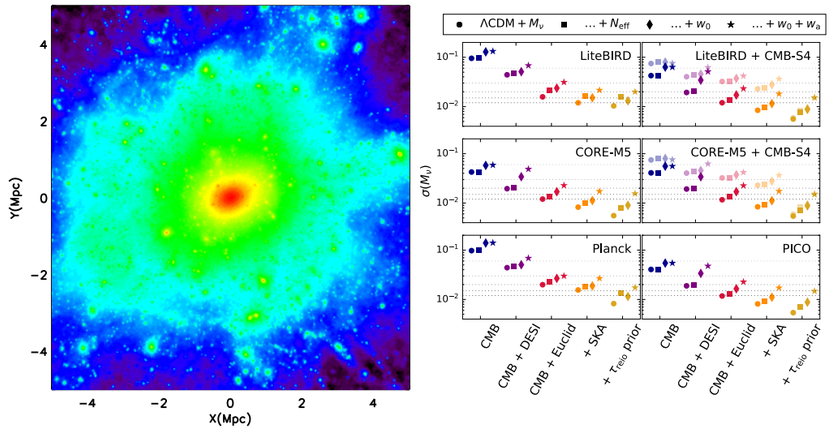

Figure 1: (Left) Typical halo of a galaxy if Dark Matter is made of self-interacting particles, derived from our N-body simulations [7]. (Right) Sensitivity of future cosmological experiments to the neutrino mass, in electron-volts, derived from Markov chains of simulations of the Universe [4]. Each point refers to one combination of experimental data sets and one assumption on the cosmological model.

N-body simulations

We also used the RWTH cluster for massive N-body simulations of the formation of galactic Dark Matter haloes in the Universe, starting from the unusual assumption that Dark Matter is made up of self-interacting component [7]. We found that the shape of Dark Matter haloes are influenced by the self interaction, but not in the way that was expected before on the basis of incorrect analytical estimates.

Publications:

[1] BRINCKMANN T, LESGOURGUES J.
MontePython 3: boosted MCMC sampler and other features. 2018.

[2] VAGNOZZI S, BRINCKMANN T, ARCHIDIACONO M, FREESE K, GERBINO M, LESGOURGUES J, SPRENGER T.
Bias due to neutrinos must not uncorrected go. JCAP. 2018;1809,no.09:001.

[3] SPRENGER T, ARCHIDIACONO M, BRINCKMANN T, CLESSE S, LESGOURGUES J.
Cosmology in the era of Euclid and the Square Kilometre Array.
JCAP. 2019;1902:047.

[4] BRINCKMANN T, HOOPER DC, ARCHIDIACONO M, LESGOURGUES J, SPRENGER T.
The promising future of a robust cosmological neutrino mass measurement.
JCAP. 2019;1901:059.

[5] AGHANIM N, ET AL.
Planck 2018 results. VI. Cosmological parameters. 2018.

[6] AKRAMI Y, ET AL.
Planck 2018 results. X. Constraints on inflation. 2018.

[7] SOKOLENKO A, BONDARENKO K, BRINCKMANN T, ZAVALA J, VOGELSBERGER M, BRINGMANN T, BOYARSKY A.
Towards an improved model of self- interacting dark matter haloes.
JCAP. 2018;1812,no.12:038.

Selected honors

- Our work on the RWTH cluster has contributed to the results of the Planck collaboration, which has been granted several prizes and awards: the 2018 Cosmology Gruber Prize 2018 (USA) and the 2018 Group Achievement Award of the Royal Astronomical Society (UK).

Conference participations

- Our work has been presented in many places and conferences including the University of Zurich (Hot Topics in Particle Cosmology, September 21, 2018), of Heidelberg (NEUTRINO 2018, June 08, 2018), the ETHZ in Zurich (PPC2018: XIIth International Workshop on the Interconnection between Particle Physics and Cosmology, August 20-24, 2018), the LAPTh in Annecy (Dark Side of the Universe 2018, June 25-29, 2018).

Engineering Sciences

Mechanics and Constructive Mechanical Engineering | DFG 402
Heat Energy Technology,
Thermal Machines, Fluid Mechanics | DFG 404
Materials Engineering | DFG 405
Materials Science | DFG 406
Electrical Engineering and Information Technology | DFG 408

Picture: Freepik

Mechanics and Constructive Mechanical Engineering | DFG 402

Analysis of Aerodynamic Noise Generation and Propagation in a Centrifugal

Scientific work accomplished and results obtained

Aeroacoustic phenomena in turbomachinery have now been investigated for more than five decades. However, most research projects were focused on noise emissions of aircraft engines and very few projects focused on aerodynamic noise generation and propagation in centrifugal compressors. Heretofore most experimental efforts focused on the compressor inlet domain with comparatively modest measuring conditions. At the compressor outlet, measurements have been both difficult and expensive due to the high pressures and temperatures. Numerical studies on the other hand are very challenging, since the highly unsteady nature of the aeroacoustic phenomena combined with the complex geometry of the impeller and the unsymmetrical volute require an extraordinary high spatial and temporal resolution. The necessary computing resources can only be provided by state-of-the-art high performance clusters, why research in this field is burdensome and expensive. Therefore, with the universities great access to computational resources, the ongoing project has a great relevance in this field of research.

The final goal of this project lies in developing a measurement technique to determine the in-duct sound power in the discharge pipe of a centrifugal compressor stage. For this, the analyses of aerodynamic noise generation mechanisms in a centrifugal compressor and the propagation of sound through the volute into the pressure pipe are crucial. Therefore, extensive numerical simulations are performed, yielding insights into the aeroacoustic behaviour of the stage. The noise generation is captured with unsteady full annulus 360° CFD-simulations, for which computing time in the upcoming period is asked for. The noise propagation through the pressure pipe, on the other hand, is then investigated by the project partners at the Technische Universität Berlin (TUB) with CAA-simulations. Subsequently, based on the numerical results, different measurement techniques to estimate the radiated sound power are derived, validated and compared. Finally an innovative measuring concept to measure the radiated sound power in the pressure pipe is developed. For this project an existing test rig with a highly loaded transonic centrifugal compressor and a vaneless diffusor is used and will be utilised to obtain first experimental data [1].

In the following, the scientific work accomplished within the previous grating period is presented. The project is divided into three sub-projects. In the first sub-project, the numerical simulations are performed and analysed. The second sub-project focuses on the development of different measurement techniques and the selection of appropriate pressure transducers. In the third sub-project, the test-rig modifications are conducted and first experimental investigations on the measurement conditions are done. The experimental application of the newly developed measurement technique is planned for a second project phase, which is still in the application process.

Project ID: jara0137

PETER JESCHKE
Institute of Jet Propulsion and Turbomachinery, RWTH Aachen University

LARS ENGHARDT
Institute of Fluid Dynamics and Technical Acoustics, TU Berlin Department for Propulsion Technology and Engine Acoustics

ARMIN FASSBENDER
Institute of Jet Propulsion and Turbomachinery, RWTH Aachen University

JAKOB HURST
Institute of Fluid Dynamics and Technical Acoustics, TU Berlin Department for Propulsion Technology and Engine Acoustics

Sub-project 1

The first sub-project contains the numerical investigations of the noise generation and propagation mechanisms and is the only one requiring high computer performance. At the beginning of the project, the mesh generation of the impeller, diffuser, volute and its outlet was conducted. For the meshing process a general understanding of the sound generation mechanisms is crucial to determine the maximum cell size, which was found, as described in the project application, to be 0.7mm. The impeller and diffuser were first meshed to perform RANS-simulations capturing the aerodynamic behaviour, resulting in a fine mesh in regions with strong flow gradients and a comparatively coarse mesh in the remainder. In a second step the mesh was refined in coarse regions to maintain the limiting cell size of 0.7mm. During the meshing process of the volute geometry, severe problems occurred, and due to this, the projects time plan was delayed. Since there were no automated meshing procedures available, the meshing had to be done manually, requiring a sophisticated block arrangement. At the outlet of the volute, a short test section and a numerical sound damper were installed to avoid reflections at the outlet boundary. For numerical stability reasons a nozzle accelerates the flow upstream of the outlet. The configuration is shown with a shortened silencer in Figure 1.

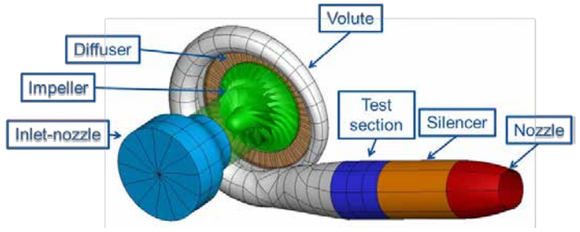

Figure 1: Meshed components for 360° simulation (shortened silencer)

In the next step, single passage RANS-simulations containing impeller, diffuser and volute were conducted on the fairshare partition. In order to evaluate the aerodynamic behaviour of the stage the static pressure at the nozzle outlet was varied, and therefore different operating points were simulated. Finally one operating point close to the best efficiency point was chosen for the first full annulus 360° URANS-simulations. The initialisation was obtained from a frozen rotor simulation, where the relative position of the impeller is held constant and unsteady effects are neglected. This frozen rotor simulations was the first task conducted on the JARA partition, due to the increased mesh size. With this initialisation the unsteady 360° URANS-simulations could be started. In total two operating points were simulated until convergence since the beginning of the project and a third operating point was started.

Part of this project is the investigation of aerodynamic noise generation mechanisms in centrifugal compressors coupled with a vaneless diffuser and a volute. In order to identify the dominant sound sources, the pressure fluctuations have to be analysed. TRACE allows for storing the Fourier coefficients for various harmonics of the blade passing frequency (BPF) while performing unsteady simulations. This way the relevant frequencies can be extracted and analysed efficiently. Figure 2 shows the pressure fluctuations on the impeller blades at shaft speed. Due to its geometry the volute induces asymmetries upstream in the flow region of the impeller. Considering all of the 13 impeller passages provides the possibility to capture these asymmetries and therefore obtain a different pressure pattern for each of the blades. The fluctuations are very large in the impeller outflow region, where large gradients dominate the flow regime. Due to the large gradients, small distortions lead to large fluctuations in the rotating frame of reference. The same occurs on the blade suction side at the leading edge. Even though the compressor operates at reduced shaft speed, shock waves form at the compressor leading edges, resulting in large gradients.

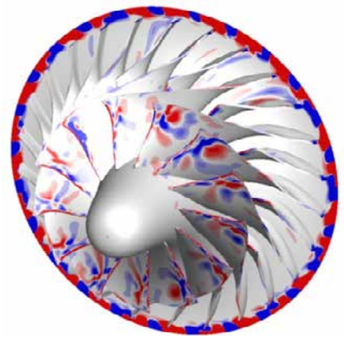

Figure 2: Instantaneous pressure fluctuations on impeller blades at shaft speed

However, with the first unsteady 360° URANS-simulation it was found out that the so called rotor-alone noise is the dominant sound source mechanism in the given compressor configuration. This mechanism can be explained by Figure 3, which shows the pressure fluctuations at BPF1 (left) and BPF2 (right) in the diffuser as well as the static pressure distribution at the impeller exit for a cut-plane at 50% channel width. The outflow of centrifugal compressors is inhomogeneous in circumferential direction due to a well- known jet-wake fluid structure. Since this inhomogeneous field is rotating with shaft speed, pressure fluctuations are induced in the diffuser. Because the induced fluctuations cannot be described by a single sine-wave, a Fourier-decomposition yields peaks at the blade passing frequency and its harmonics. It was found, that the first two BPFs dominate the frequency spectrum and therefore these two frequencies were used for further analyses. As can be seen in Figure 3, the pressure fluctuations form distinctive mode patterns in the diffuser. The BPF1 shows a circumferential mode order of m=13, which corresponds to the 13 main and 13 splitter blades of the impeller. The BPF2, on the other hand, shows a circumferential mode order of m=26, which corresponds to the total number of blades.

Downstream, the pressure waves excited in the diffuser propagate through the volute. Due to its asymmetric and complex geometry, the propagation of sound waves through the volute cannot be described in terms of analytic expressions. The pressure fluctuations at BPF1 on the volute casing are shown for the same operating conditions. Note the change in the colour scale, which lets the mode pattern appear differently. In Figure 4 it can be seen, that the pressure fluctuations form patterns with distinctive numbers of minima and maxima in circumferential and radial direction. The fluctuations are rotating with impeller speed in the same direction and are emitted into the pressure pipe at volute outlet. Comparing the pressure amplitude, it can be seen that the pressure fluctuations are attenuated towards the volute exit, which is due to a change in cross section.

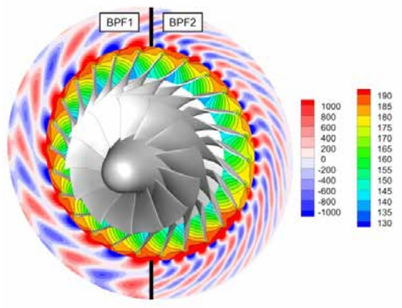

Figure 3: Pressure fluctuations in the diffuser at BPF1 and BPF2 arising from inhomogeneous distribution of static pressure at impeller outlet

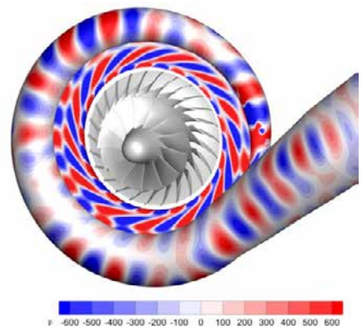

Figure 4: Pressure fluctuations propagating through diffuser and volute

Despite the sound source mechanisms in the compressor and the volute, the sound pressure field at the volute outlet is of great interest in order to develop a suited measurement technique to determine the radiated sound power in the pressure pipe. The acoustic field at the volute outlet can be decomposed into different modes. This can be achieved by conducting a radial mode analysis (RMA) explained in sub-project 2. These acoustic modes show a symmetric flow pattern each, an example given by the (3,1) - mode shown in Figure 5.

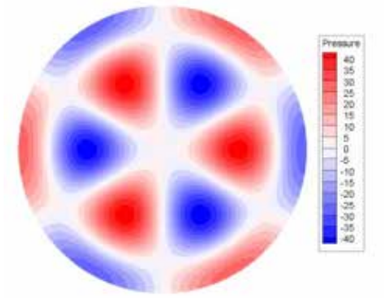

Figure 5: (3,1) - mode in a circular duct

The sound pressure field can fully be described by the modes and their corresponding amplitudes. Since only a limited number of modes are capable of propagation, the number of analysis points required is predefined. Given the flow simulation results, the pressure fluctuations can easily be obtained at any point in the flow region and the mode analysis thus be conducted. When measurements are conducted, however, the number of sensors is crucial for financial and practical reasons. Hence different approaches are investigated to develop feasible measurement techniques. The simulations conducted on the JARA partition form the foundation of these investigations. The development of these approaches is part of the second sub-project and is described in the following chapter.

Sub-project 2

In the second sub-project different measurement techniques are developed to estimate the radiated sound power based on data measured in the acoustic test section. In this sub-project the project partners at the TU Berlin with their great experience in the field of turbomachinery acoustics ([2]-[7]) play a key role. The work is mainly based on analytical work and therefore no extensive computer performance is required. According to the presented work schedule in the application, the work packages contained in this sub- project are still carried out and so only interim results are presented. In the first work package a model is developed to describe the sound emissions by the compressor stage. This is done analytically with a field of monopole- and dipole-sources, the amplitudes and phase shifts being optimised with the sound pressure field data obtained from the simulations. The aim is, to find complex amplitudes, which yield a similar mode distribution like the one extracted from the unsteady simulations. Based on this model, a measurement technique is developed. With the measured pressure amplitudes obtained from pressure transducers, the amplitudes in the analytic source model are determined and from this, the acoustic field can be reconstructed and the sound power determined.

In addition to the model-based approach, a second measurement technique based on “compressed sensing” is developed [8]. To determine the amplitudes of all cut-on modes, too many sensors would be needed. Compressed sensing is an often used method, to reconstruct sparse signals with far fewer samples than required by the Shannon-Nyquist sampling theorem. In simple words, it is possible to detect the acoustic field with a low sensor-count if only a few modes are dominant.

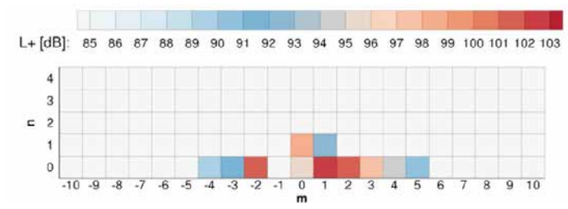

Figure 6 - Modal sound power level at volute outlet for BPF1

Figure 6 shows the result of a radial mode analysis (RMA) conducted on the sound field from the first unsteady HPC-simulation. As it can be seen, the field is dominated by few modes and, therefore, the before mentioned assumption of sparsity is legitimate. Besides sparsity, the quality of the reconstructed signal is also strongly dependant on the measurement positions. Therefore, different measurement positions are tested on realistic sound fields, which are extracted from the simulations.

A key point for the measurements planed at the end of this project is the sensor alignment in the test section. With respect to the measurement technique, different sensor alignments are specified and, from this, acoustic test sections are designed.

Sub-project 3

In the third sub-project, the measurement concept for the centrifugal compressor test rig is specified. For the acoustic measurements the test rig has to be modified. On one hand, parts of the pressure pipe have to be removed in order to implement the acoustic test sections. On the other hand, unwanted noise sources must be avoided. For this, pipe components have been identified as potential noise sources and will be changed for the measurements. At the end of the first project phase, the measurement conditions are investigated with first test measurements. For this, suited sensors, amplifiers and a data acquisition system are chosen. Since this project phase is not completed yet, no further details are given at this point.

Realization of the project

For the flow simulations carried out in this project the unsteady 3D Reynolds-Averaged Navier-Stokes Code TRACE developed by the German Aerospace Center (DLR) was used, as originally planned. No code modifications were necessary. However, adaptions on the MPI environment were necessary to run the simulations.

The URANS-simulations were conducted on the RWTH compute cluster CLAIX. For the parallelisation, different numbers of nodes were tested as reported in the “code performance” chapter in the project application. The simulations were finally performed using 600 cores and an average of 1.1TB memory. Since the beginning of the project, two operating points were simulated until convergence. A third operating point was started but will not reach convergence in this project phase.

Of the granted computing time of the last period around 75% will be used till October. This is due to two reasons. First, the resources could not be used at the beginning of the granting period because of technical problems related to the new cluster hardware of CLAIX and the filesystem lustre. With the great help of the ITC, adaptions on the MPI-environment could be made and the simulations be started. The second reason is related to the cluster usage during the summer period. Combined with the problem size, requesting 600 cores, this lead to pending times of weeks and during this time the resources could not be used.

Publications with project results

- ENGHARDT L, FASSBENDER A, HURST J, JESCHKE P.
  Sound Sources of Radial Compressors—A Numerical Study on the Outlet Side. In book: Flinovia—Flow Induced Noise and Vibration Issues and Aspects-II:71-84. 2017.
- HURST J, BEHN M, TAPKEN U, ENGHARDT L.
  Detection of the dominant acoustic modes emitted by turbomachinery using compressed sensing. Inter-noise. 2016.
- HURST JD, TAPKEN U, FASSBENDER A, JESCHKE P, ENGHARDT L.
  Scattering of high order modes in diffuser and 90 degree bend ducts.
  23rd AIAA/CEAS Aeroacoustics Conference. Denver, Colorado, USA. June 2017. AIAA-2017-4039.

· ENGHARDT L, FASSBENDER A, HURST J.
Sound sources of radial compressors – a numerical study on the outlet side.
Flinovia II – Flow Induced Noise and Vibration Issues and Aspects. 2017.

Theses completed within the project

The results obtained in this project will be used in the thesis of Armin Faßbender. However, the thesis is not completed yet.

Additional references

[1] Department Press and Communication, RWTH Aachen University. New Testing Bench for Centrifugal Compressor. http://www.rwth-aachen.de/cms/root/Die- RWTH/Aktuell/Pressemitteilungen/April/~kwuy/Drei-Millionen-teurer- Pruefstand-fuer-Ra/?lidx=1. Accessed at 18.08.2016.

[2] ENGHARDT L, TAPKEN U, NEISE W, KENNEPOHL F, HEINIG L. Turbine Blade/Vane Interaction Noise: Acoustic Mode Analysis Using In-Duct Sensor Rakes. 7th AIAA/CEAS Aeroacoustics Conference. May 28-30 2001. Maastricht, Netherlands. 2001;No.2001-2153.

[3] MOSER M, TAPKEN U, ENGHARDT L, NEUHAUS L. An Investigation of low-pressure turbine blade-vane interaction noise: measurements in a 1.5 stage rig. Journal of Power and Energy. 2009;Part A,Vol.223 (No. 6).

[4] BROSZAT D, TAPKEN U, ENGHARDT L, LENGANI D, MARN A. Validation of an integrated acoustic absorber in a turbine exit guide vane. 17th AIAA / CEAS Aeroacoustics Conference. June 05-08 2011. Portland, USA.

[5] ENGHARDT L, HOLEWA A, TAPKEN U. Comparison of Different Analysis Techniques to Decompose a Broadband Ducted Sound Field in its Mode Constituents. 13th AIAA/CEAS Aeroacoustics Conference. 21-23 May 2007. Rome, Italy. 2007;No.AIAA-2007-3520.

[6] JÜRGENS W, PARDOWITZ B, ENGHARDT L, TAPKEN U. Separation of broadband noise sources in aeroengine ducts with respect to modal decomposition. 17th AIAA / CEAS Aeroacoustics Conference (32nd AIAA Aeroacoustics Conference). 05-08 June 2011. Portland, USA. 2011;No.AIAA-2011-2879.

[7] LEMKE O, NEISE W, ENGHARDT L, MÖSER M. Control of tonal fan noise using flow induced secondary sound sources generated by air jet actuation. International Journal of Aeroacoustics. 2011;Vol.10 (Nummer 5 - 6).

[8] HURST J, BEHN M, TAPKEN U, ENGHARDT L. Detection of the dominant acoustic modes emitted by turbomachinery using compressed sensing. Inter-noise, Hamburg, August 2016. 2016;12 pages.

National and international cooperations

· Technische Universität Berlin (TUB)

Penny-Cavity Secondary Flow in Variable Stator Vanes

Project ID: jara0162

PETER JESCHKE
Institute of Jet Propulsion and Turbomachinery
RWTH Aachen University

SIMON STUMMANN
JOHANNES JANSSEN
Institute of Jet Propulsion and Turbomachinery,
RWTH Aachen University

Scientific work accomplished and results obtained

Sub-project 1: Meshing and numerical studies

Since meshing has great importance in DES calculations, meshing obtained major attention. Several mesh studies have been performed in this sub-project, resulting in usage of three different meshes with about 10, 43 and 62 million cells.

The meshing was validated using Pope's criterion which emphasizes that more than 80% of the turbulent kinetic energy should be computed directly and less than 20% modeled with a turbulence model. As it turned out, the coarse grid was not able to satisfy this criterion so that the results obtained on this mesh has only limited trustworthiness.

Further validation is made by inspection of the forming vortex structures. It has been found that on the one hand only with the 62 million cell mesh the entire fine vortex architecture is resolved. On the other hand, the flow effects are also reproduced qualitatively correctly by usage of the 43 million cell mesh which in turn has performance advantages.

Furthermore, a time step study has been performed in order to minimize its influence. It has been revealed that a time step of T = 1e–6 sec which results in a CFL number of CFL = 1 is adequate. In the LES regions, the grid density is much higher so that the CFD number is much smaller in these regions of interest. Finally, the averaging of the flow field was performed over 45000 time steps which is equivalent to a simulated time of t = 0.045 sec. In this space of time, the fluid runs ten times from inlet to outlet, so that a sufficient overall time is reached. For RANS and SBES simulations, the same numerical grids have been used.

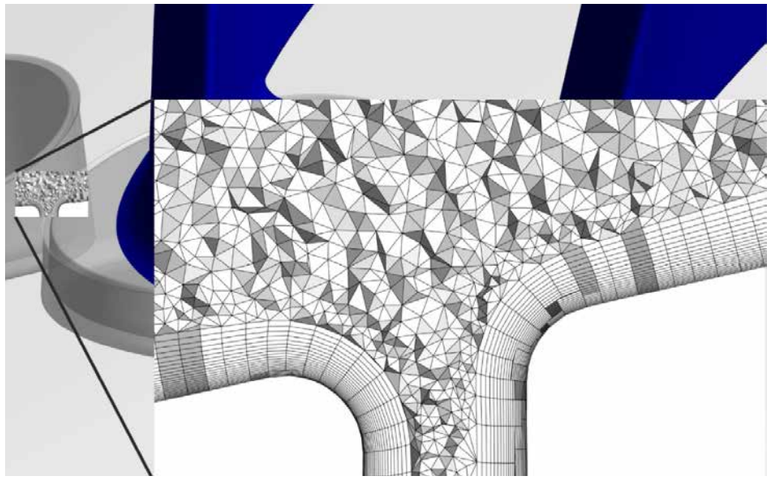

Figure 1: Numerical grid in the outflow of the penny cavity

Sub-project 2 and 3: DES-Simulations and Evaluation

In sub-project 2, the DES Simulations have been performed with several geometries. The basic stator without a penny cavity was simulated first. This provides an essential data basis to compare all other variants with. The other variants include the same stator with a standard penny cavity and a penny cavity with a geometrical feature.

The penny cavity flow is driven by the hub pressure distribution. Basically, fluid enters the cavity in the high-pressure regions and leaving the cavity at low-pressure ones. The inflow

regions can therefore be found at the leading edge and the rear side of the cavity. The two outflow regions are located on the suction side and the pressure side of the vane. In Figure 2 the inflow and outflow regions can be identified. Also shown is the velocity in radial direction. From this velocity distribution, it is apparent that the outflow on the suction side is bigger in size and higher in velocity than the outflow on the pressure side.

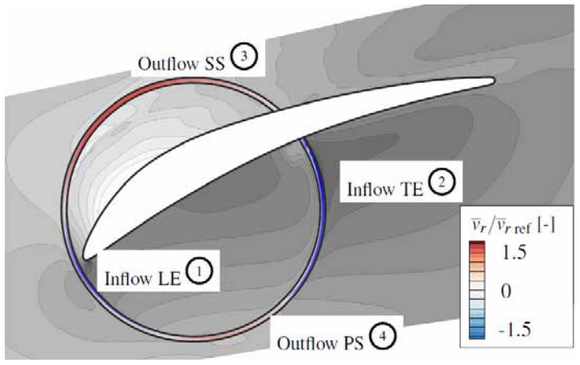

Figure 2: Inflow and outflow regions of the penny cavity

Great importance for the mixing behavior has the momentum ratio between momentum of the free stream and leakage momentum which is below 1 in this case. The outflow on the pressure side of the penny cavity has a low momentum ratio of R = 0.3 and only 16% of cavity mass flow. The jet enters the passage and, due to the low momentum ratio, the jet is immediately diverted into the direction of the main flow. The outflow height is also very low as a result of this low momentum ratio. As such, the jet veers in the direction of the cross flow inside the hub boundary layer. The folding mechanism of the jet causes a counter-rotating vortex pair. The low mass flow is also the reason why no further significant secondary flow interaction can be identified.

The suction-sided outflow of the cavity has a momentum ratio of 0.6. Furthermore, 84% of the cavity fluid enters the passage at this outflow region. This outflow therefore causes a significant secondary flow pattern, which will be discussed. The outflow is a ring segment of 120°, the upstream part which is overflown from the right side at the front regions. The rear part is overflown from the left side, resulting in an asymmetrically occurring counter-rotating vortex pair.

The carried out scale resolving simulations also give proof that these secondary flow phenomena occur similarly to the jet in crossflow test case. At the leakage mixing zone, a steady counter-rotating vortex pair develops as well as highly unsteady shear layer vortices. Figure 3 shows the development of turbulent structures in the emerging leakage's mixing zone. By comparison with experimental data, it is shown that the flow prediction in variable stator vanes is successful, particularly by means of scale resolving simulations.

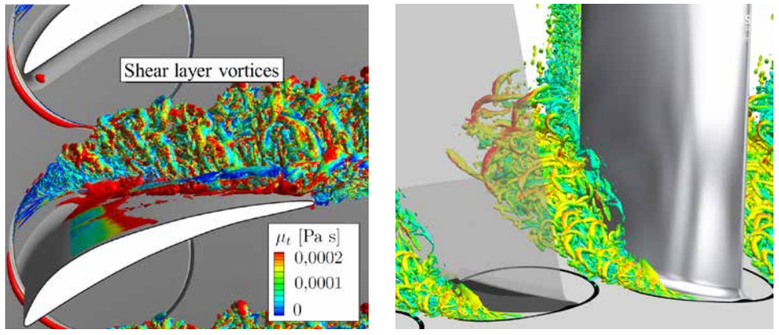

Figure 3: Unsteady secondary flow in the stator passage

Finally, the additional losses due to the penny cavity are quantified and found to arise primarily in the turbulent mixing zone. The entropy production in the shear layer vortices has a turbulent character. The vortices break up into smaller three-dimensional vortices and finally dissipate. The penny-cavity flow produces 5.8% additional flow losses. 99% of these losses are produced in the secondary flow region. Using Denton's loss correlation the losses can be broken up into the two outflow regions. 88% of the flow losses are produced by the outflow from the suction side.

Realization of the project

Corresponding with the Jet in Crossflow test case, highly unsteady turbulent vortices are expected in the leakage mixing zone. Since RANS calculations show lack of resolving these turbulent structures, extensive scale resolving simulations have been performed. For the purpose of high resolution turbulence modelling, DES simulations which combine LES and RANS approach are used within the commercial solver ANSYS CFX. The switching model used within ANSYS CFX code is Stress-blended Eddy Simulation (SBES) which uses an improved shielding function to switch between RANS and LES zones.

For the flow simulations carried out in this project the unsteady 3D Navier-Stokes Code ANSYS CFX 17.0 is used. CFX uses a hybrid parallelization approach. On the highest level, MPI parallelization is used with intelligent block partitioning for equal work load of the MPI-processes.

In prior projects ANSYS CFX was successfully employed for high performance computing purposes. A scalability test was performed using the 62 million cells mesh with the used DES-model SBES in CFX. The scalability test was carried out on the RWTH CLAIX partition. As expected, increasing the number of nodes leads to more time steps performed. In an ideal scaling test the simulation speed would double if using twice as many nodes. The achieved speedup and the ideal speedup are compared in figure 4. For the final SBES simulations, 480 Cores on 20 nodes have been used.

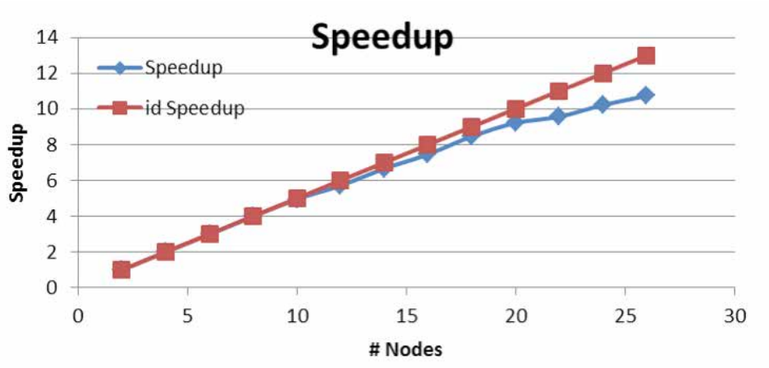

Figure 4: Scaling behavior of ANSYS CFX with the SBES-Model on the CLAIX-Partition

The granted computing time of 2.5 million core hours has not been used completely. A large part of the simulations had to be done at the beginning of the project. For this purpose, some of the resources of a previous project were used to provide the results in a timely manner. In addition, over time, the focus of the project has increasingly been put on the upcoming experimental work packages. As a result, the numerical part of the project has been scaled down and instead of the originally planned five DES simulations only three have been performed.

Publications with project results

- STUMMANN S, POHL D, JESCHKE P, WOLF H, HALCOUSSIS A, FRANKE F. Secondary flow in variable stator vanes with penny-cavities. Proceedings of ASME Turbo Expo 2017: Turbine Technical Conference and Exposition. June 26-30, 2017. Charlotte, North Carolina, USA (GT2017-63771).

Theses completed within the project

- STUMMANN S: Sekundärströmung und Verluste in Verstellleitschaufeln mit Penny-Kavitäten. PhD thesis. Rwth Aachen University.
- JANSSEN J. Analyse der Sekundärströmung in Verstellstatoren mit Penny-Kavitäten mithilfe eines skalenauflösenden Verfahrens. Master‘s thesis. RWTH Aachen Universtiy.
- WOLF H. Aerodynamische Bewertung von Pennykavitäten bei Verstellstatoren in Hochdruck-verdichtern. PhD thesis. Ruhr-Universität Bochum.

National and international cooperations

- Cooperation with MTU Aero Engines AG, Munich, Germany

Heat Energy Technology, Thermal Machines, Fluid Mechanics | DFG 404

CFD simulations of models of a solar central receiver system to study the convective heat loss caused by wind

Project ID: rwth0251
BERNHARD HOFFSCHMIDT
DLR – Institute of Solar Research, Chair of Solar Components, Cologne

Technical contact:
SILVAN SIEGRIST,
DLR – Institute of Solar Research, Jülich

Project Description
During the operation of multi-megawatt receivers of concentrated solar power (CSP) tower systems, heat is lost mainly due to (a) the partial reflection of the incoming solar radiation on the receiver surface, (b) the radiation from the hot receiver surfaces to the surroundings, (c) the conduction to support structures and (d) the mixed convection from the hot receiver surfaces to the surroundings.

Previous research showed that the wind speed may have significant influence on the convective heat loss from concentrated solar power (CSP) cavity receivers. So far, this effect has not been studied for very large receivers. Thus, the project focused on the mixed convective heat loss from cavities of large solar central receiver (SCR) systems with a receiver thermal output power of around 100 MW.

During this project we addressed the following scientific questions:

1. How large is the mixed convective heat loss from multi-MW cavity SCR systems?
2. How large are the shares of the forced and of the free convection in such a system, respectively?
3. How does the mixed convective heat loss from such a system vary with varying magnitude and direction of the incoming wind?
4. How do the results of the numerical simulations relate to the experiment done in the wind tunnel?
5. What are the flow patterns or flow effects that affect the convective heat loss substantially?
6. What could be the most effective ways to reduce convective heat loss from such systems?

By addressing the above questions we reached the following three scientific goals:

A. We estimated the heat loss contributions by the forced and by the free convection.
B. We compared the forced convective heat loss to the experiment and validated the CFD code for applications in convective heat loss from large SCR systems.
C. We analyzed the flow characteristics inside and around the cavity and identified patterns or effects which substantially affect the convective heat loss.

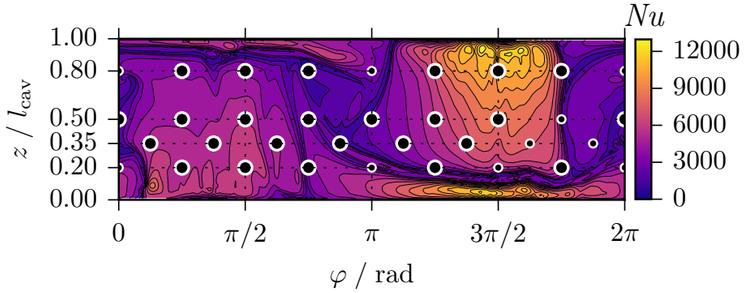

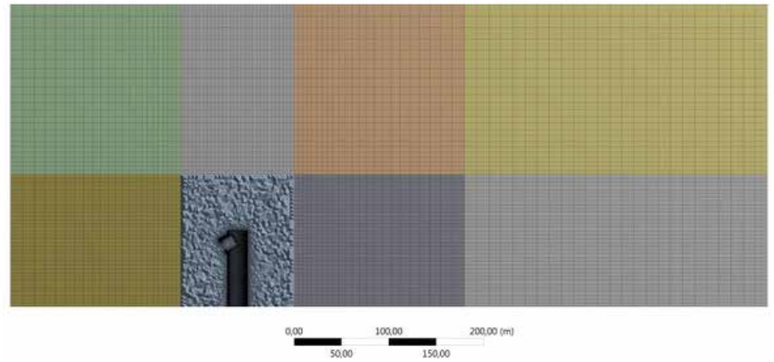

Publications:

Siegrist S. Forced convective heat loss from cavities of multi-megawatt scale solar receivers. Doctoral thesis. 2018. DOI:https://doi.org/10.18154/rwth-2018-231862.

Selected honors

- Silvan Siegrist received for his PhD the Borchers Badge of the RWTH Aachen.

Soot Model Development in Multi-dimensional Flames

Project ID: rwth019
AGNES JOCHER
Institute for Combustion Technology,
RWTH Aachen University

Non-premixed laminar ethylene-air coflow flames have been used to assess soot model performance with increasing flame length and soot content. This setup allows for studying soot formation at a rather fundamental level under well-controlled laboratory conditions. The possibility of using a 2D computational domain for this configuration makes the use of detailed chemistry feasible. At the same time, the flame is complex enough to account for effects such as curvature, which is not the case in simplified 1D configurations that have been used before to evaluate the soot model.

Here, four test cases have been computed, with an increasing ethylene content of 32%, 40%, 60%, and 80% in volume. The peak soot volume fraction shifts from the centerline to the wing with decreasing nitrogen dilution. In addition, the flames extend further downstream, which enhances the importance of multi-dimensional convection, diffusion, and heat radiation processes. For all flames, the gas-phase structure is found to reasonably match the measurements, while for the two flames with lower ethylene content also a well-predicted soot distribution is observed. The error associated with HMOM as statistical framework is assessed by comparison to Monte Carlo simulation and found to be negligible for the 80% flame, see Fig. 1.

To improve the model predictions, an enhanced description of soot particles by an additional independent parameter, the number of hydrogenated sites on the surface of a soot particle, is tested by Monte Carlo simulations. The input conditions for the Monte Carlo simulations are obtained from the initial DNS study. It is shown that in the flames with dominant surface growth, the enhanced soot model description is closer to the experimental soot volume fraction results. In the 60% flame, the enhanced model description with hydrogenated sides is further away from the measurements compared to the volume-surface description and for the 80% case, hardly any difference between the two descriptions could be observed, see Fig. 1. Assessing the responsible source terms for soot formation along several streamlines within the flames identifies a change in the dominant process from surface growth to condensation with increasing ethylene content. At higher temperatures, surface growth is more important, while at decreasing temperatures, condensation becomes the dominant process.

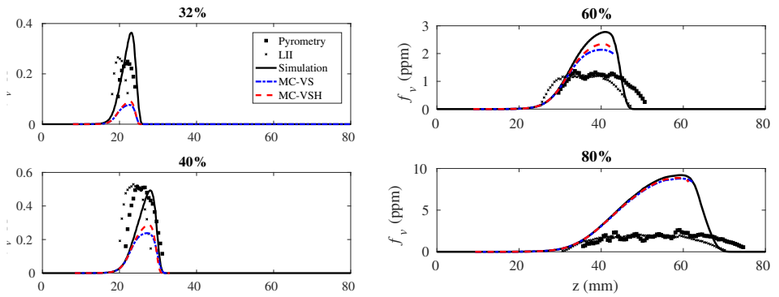

National and international cooperations

- Institut Jean le Rond d'Alembert, Sorbonne Université, UPMC Univ Paris06, CNRS UMR 7190, Paris, France

Direct Numerical Simulation (DNS) of hypersonic flows over compression ramps

Project ID: rwth0221
IGOR KLIOUTCHNIKOV
Shock Wave Laboratory,
High temperature gas dynamics,
RWTH Aachen University

Scientific work accomplished and results obtained

The Görtler vortices induced by shock wave-boundary layer interaction on the compression ramp are investigated by using direct numerical simulation (DNS) for three ramp angles of 15, 20, and 25 deg. The freestream Mach number and the Reynolds number based on the flat-plate length are 7.7 and $8.6{\cdot}10^5$, respectively. The mesh consists of 151 million grid points. The results have been proved to be grid-independent. Several validation tests are performed and good agreement is achieved by comparing with experiments.

Görtler vortices occur over the ramp for all three ramp angles and are well captured by DNS. For the considered ramp flows, both the flow inside the separation bubble and the Görtler vortices downstream of reattachment show unsteady behaviors. A spanwise variation of the heat flux is observed on the ramp surface both downstream and upstream of reattachment. The Görtler vortices visualized by streamlines in the wall-normal plane indicate wavelengths of 3.1, 2.7, and 2.5 mm for ramp angles of 15, 20, and 25 deg, respectively. Three-dimensional structures are found in the separation bubble, leading to a corrugated reattachment with a series of singularities (nodes and saddle points) distributed in spanwise direction. The flow reattachment enhances the downstream evolution of Görtler vortices.

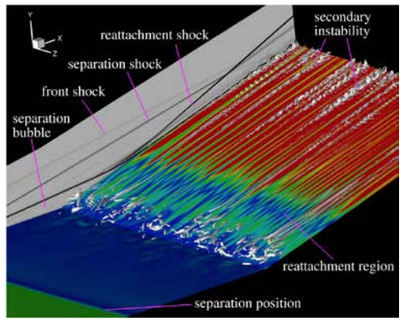

Figure 1 Hypersonic compression ramp flow with Görtler vortices.

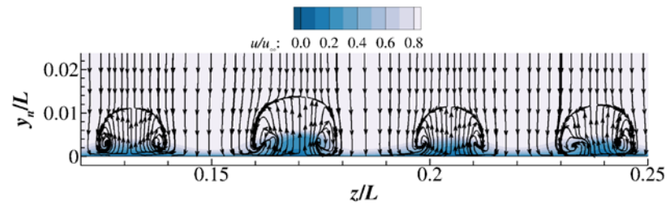

Figure 2 Görtler vortices visualized by in-plane streamlines

Publications

[1] CAO S, KLIOUTCHNIKOV I, OLIVIER H. GÖRTLER
Vortices in Hypersonic Flow on Compression Ramps.
AIAA Journal. 2019. Accessed June 2019.
doi: http://arc.aiaa.org/doi/abs/10.2514/1.J057975.

Conference participations

· S. CAO, I. KLIOUTCHNIKOV, H. OLIVIER,
"Görtler number prediction for hypersonic compression ramp flows,"
67. Deutscher Luft- und Raumfahrtkongress, Friedrichshafen, September 2018.

Flexible Simulation of Fuel Cells with OpenFOAM

Project ID: jara0070
WERNER LEHNERT
JARA-HPC,
Institute of Energy and Climate Research,
Electrochemical Process Engineering (IEK-3),
FZ Jülich

DIETER FRONING
SHIDONG ZHANG
STEVEN BEALE
MARTIN ANDERSSON
UWE REIMER

Scientific work accomplished and results obtained

Results were attained within the following sub-projects:

- Electrochemical models
- Volume of fluid (VOF) models
- Electrochemical hydrogen purification

Electrochemical models

Heat and mass transfer are the dominant issues in polymer electrolyte fuel cell design. In the past year, the focus of Mr. S. Zhang (PhD student) has been on high temperature polymer electrolyte fuel cells (HT-PEFCs), which operate in the range 140-180°C, meaning that the reactants and products are in a vapor state, with the emphasis going forward on low temperature polymer electrolyte fuel cells (LT-PEFCs). Computational fluid dynamics (CFD) [A1, A2] is addressing transport and electrochemical phenomena at the continuum scale. The open source platform OpenFOAM [A3, A4] has been employed to perform large-scale calculations for single cells and stacks of cells using the JARA-HPC facilities.

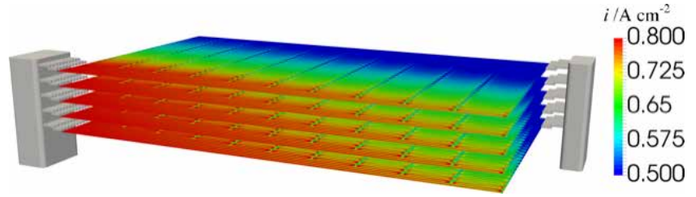

Figure 1. Current density distribution in a 5-cell HT-PEFC stack.

During the past year, Mr. Zhang performed detailed simulations of a 5-cell PEFC stack, with each cell having a nominal area of $200cm^2$. The stack geometry was tessellated with a body-fitted mesh, produced with the commercial package ICEM-CFD, the flow-field calculations being performed with OpenFOAM. [P1, P2]. The mesh size was $170x10^6$ compute cells, and the performance calculations were parallelized on 900 cores. Typical run times were of the order of 36-48 hours. The flux of fuel, air (and component species), cooling oil and charge were all considered along with the electric potential. Figure 1 shows the current density in the stack for a mean current density of $0.6\ A/cm^2$. Validation of the numerical results was achieved through comparison with experiments and with a simplified CFD stack model based on the distributed resistance analogy (DRA) [A5, A6]. Agreement was excellent; however, the fine-scale calculation displayed a resolution/fidelity that neither experiments nor DRA calculations can capture. This is important, as local extrema in current density, captured for the first time with the Juelich model, can affect the lifecycle performance and durability of a stack.

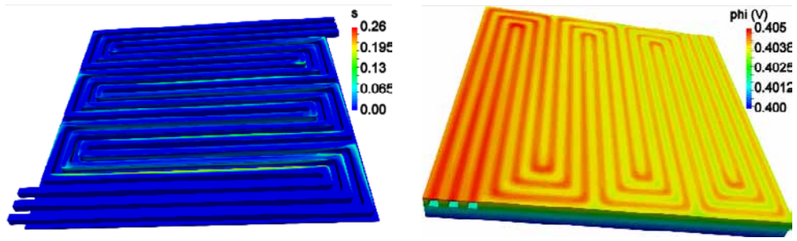

Figure 2. (a) Saturation and (b) potential distribution in an LT-PEFC.

Figure 2 shows some preliminary calculations for an LT-PEFC, which is a two-phase flow problem. The geometry follows that of the International Energy Agency Technology Collaboration Program on Advanced Fuel Cells, https://www.ieafuelcell.com/, benchmark PEFC, for round robin physical and numerical experiments. Figure 2(a) shows liquid water saturation, while Figure 2(b) exhibits the electric potential obtained from the solution of a detailed Poisson system of equations.

Substantial time and energy was successfully spent on making the basic fuel cell model more stable [P3]. The original motivation for the work was the realization that the basic algorithm did not provide stable solutions in the mass transfer limit at high current density. It was subsequently noted that there were also significant deficiencies at low current densities. Four specific remedies were proposed: (1) Relax the calculation for the local current density; (2) limit the minimum local ideal or Nernst potential; (3) linearize the mass transfer boundary condition in terms of the convection flux (coefficient) and transferred-substance state value as opposed to a Neumann condition (in a previous version of code); (4) apply a flux limiter to obviate negative values of mass fraction arising during the iterative procedure. Beale also developed 'simpleFuelCell', which is a simplified fuel cell model. This work was presented at the openFuelCell workshop held in Jülich in late October 2017. József Nagy has requested Beale put the case in the OpenFOAM tutorials, https://wiki.openfoam.com/ Tutorials. The basic idea is to modify the built-in incompressible solver, icoFoam, with an electrochemical reaction and mass transfer modules. The results of these calculations may then be compared to the analytical solution of Kulikovsky [A7]. At the workshop, Profs. Beale and Lehnert proposed a book of edited chapters entitled, "Electrochemical Cell Calculations with OpenFOAM", which now has 12 chapters under development by various authors worldwide.

Tim Cramer of the Aachen High Performance Computing Group, together with Beale, set up the Jülich-Aachen OpenFOAM users group, which was initially a mailing list of 16 persons, and held a face-to-face meeting in Aachen on 27 April 2018, with a second meeting proposed for the autumn. Following discussions between Beale and Paul Gibbon (Juelich Supercomputing Center), Metin Cakircali, from the Institute for Advanced Simulation in the Juelich Supercomputing Center conducted some preliminary scalability performance measures on an openFuelCell test case provided by Shidong Zhang. Some bottlenecks were identified and the HT-PEFC cell and stack codes will be spun-off to a Danish PEFC manufacturer, SerEnergy A/S.

Detailed two-phase flow in porous media

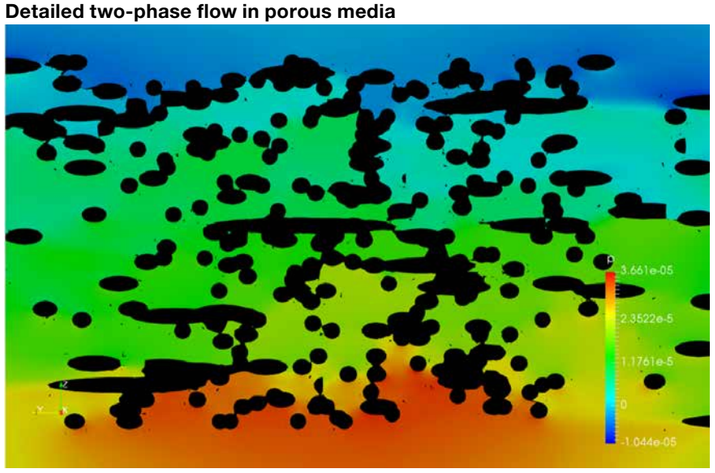

Figure 3. Pressure distribution in a porous structure.

Substantial effort was spent on meshing random cylindrical geometries using two open-source meshers, namely snappyHexMesh and cfMesh. In August 2018, Beale, together with Andersson and Mr. Zhang went to the University of Zagreb's School of Numerical Modelling of Coupled Problems in Applied Physics with OpenFOAM (NUMAP-FOAM). This is hosted by Hrvoje Jasak, one of the original developers of OpenFOAM [A8], with whom the IEK-3 are collaborating. At the same Messrs., Andersson, Zhang and Beale visited Franjo Juretić, Managing Director of Creative Fields Ltd. who produce cfMesh and work further on mesh refinement. Meshes produced by Engys (see https://engys.com/), developer of open source and enterprise versions of snappyHexMesh are being used to study single-phase transport in porous structures. This work is undertaken in collaboration with Martin Andersson (Lund University) and Pablo Garcia Salaberri (Universidad Carlos III de Madrid). This work will be used to consider both single- and two-phase flow in random porous structures in the coming months.

VOF models

Using OpenFoam (version 3.0.1), Andersson developed and solved a computational fluid dynamics (CFD) model for a single channel, which is of interest for the removal of liquid water inside a PEFC. The volume of fluid (VOF) approach (using the solver multiphaseInterFoam) was used to study the two-phase interface flow behavior, including the GDL/GC interface [P4-P8]. Note that our model is compared to synchrotron XTM measurements carried out at the Swiss Light Source at PSI (TOMCAT beamline). The model and the experiments share geometrical parameters. It was found in our last study that [P6]:

- The agreement between our model & the corresponding measurements is good considering droplet dynamics, for example the length from the liquid inlet to the first wall contact.
- We found that the two-phase flow inside the microchannel (illustrated in Figure 4) is connected to the liquid inlet size, gas flow velocity and contact angle, as well as the channel height. When the results from our recent work are compared to our previous effort [P5], it is clear that the influence of channel dimensions (width and height) is noteworthy.
- The model, as well as the experiments, present: detachment – flow in channel – wall attachment behavior when standard conditions apply. Exceptions include when the droplet is connected to the wall and GDL surface simultaneously: (1) from a decreased gas velocity; (2) from a decreased channel thickness; (3) from an increased liquid inlet area. Corner flow occurs at the wall on the side opposite to the GDL surface from: (1) a decreased gas velocity; (2) a decreased wall contact angle; or (3) an increased liquid inlet area.
- There is a strong dependence on the size of the droplet from the GDL surface liquid inlet area. A decreased liquid inlet area (with a constant liquid mass flow rate) yields noteworthy smaller droplets.
- The amount of droplets is increased from the higher gas velocity and consequently the droplets are smaller.
- The droplet moving behavior has a substantial impact on the channel height, with droplets attached to the wall (on the side opposite the GDL) and the GDL surface at the same time for the 150 µm case (thinnest channel), both for a constant mass flow rate (gas) and a constant velocity (gas).
- Smaller droplets can flow freely in the channel center for an increased period until the GC wall is attached.
- The hydrophilicity/hydrophobicity (e.g., the contact angle) has a strong impact on the droplet size (which may also be expressed as the time until detachment). A higher GDL contact angles yields a decreased droplet size. Note that a small (140° vs 153°) variance in the average contact angle has a significant influence on the droplet dynamics, determining if a (liquid) droplet remains connected to the GDL surface or if it detaches from the GDL surface, meaning that it later connects to the wall. It should be noted that the water droplet transport is somewhat stochastic.

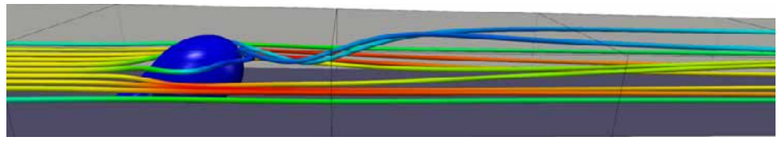

Figure 4. Gas flow around a droplet under detachment in a PEFC gas channel.

Electrochemical hydrogen purification

Within the European project, “MEMPHYS – membrane-based hydrogen purification system”, the main objective is to develop an electrochemical membrane reactor for the separation of hydrogen from industrial gas mixtures. The CFD model developed by Reimer was applied to the laboratory test cell of an industrial project partner.

The behavior of the cell for two different gas mixtures, one with 80% hydrogen and one with 50% hydrogen, was compared. It is assumed that both gas mixtures are also humidified at 295 K. In previous discussions, it was mentioned that a cell voltage of 0.2 V should not be exceeded. Based on the polarization curve model, this translates into a current density of 0.32 A cm^{-2}. For both cases, the amount of 80% of the initial hydrogen should be removed from the gas mixture. This means that the same equivalent current density and same stoichiometry are used, which are the important parameters for electrochemical conversion devices. In other words, the same amount of pure hydrogen is produced with different inlet gas mixtures. This is of importance because the final application should work with a range of different gas compositions.

For 80% hydrogen, the modeling results showed that there was no mass transport limitation present under these conditions and the cell should work fine. The situation changed for the gas mixture containing 50% hydrogen. It can be seen that the hydrogen mass fraction reaches almost zero at the last outlet channel. This means that the limiting current is only reached within the applied model. In reality, the current density distribution would not be homogeneous, and therefore it is expected that the real limitation from mass transport may be present at higher currents (maybe factor 2 or 3). Nevertheless, it becomes clear that if the cell approaches its limiting current, the main problem will arise in the dark blue region of Figure 5.

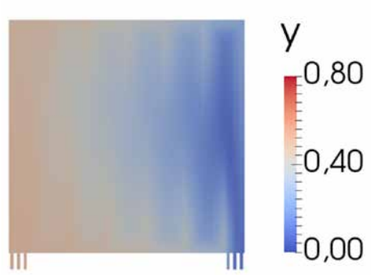

Figure 5. Hydrogen mass flow at the membrane for the 50% hydrogen gas mixture. The flow enters from the bottom left side.

Realization of this project

The simulations were run with OpenFOAM/3.0.1, as well as OpenFOAM/extend4.0. The communication via MPI is embedded, and only the application code must be developed. Several methods of domain decomposition are available with OpenFOAM.

Publications with project results

[P1] ZHANG S, REIMER U, BEALE SB, LEHNERT W, STOLTEN D.
Modeling polymer electrolyte fuel cells: A high precision analysis.
Applied Energy. 2019;233-234:1094-1103.

[P2] ZHANG S, REIMER U, RAHIM Y, BEALE SB, LEHNERT W.
Numerical Modeling of Polymer Electrolyte Fuel Cells With Analytical and Experimental Validation.
Journal of Electrochemical Energy Conversion and Storage. 2019;16:031002,1-12.

[P3] BEALE SB, REIMER U, FRONING D, JASAK H, ANDERSSON M, PHAROAH JG, LEHNERT W.
Stability Issues for Fuel Cell Models in the Activation and Concentration Regimes.
ASME Journal of Electrochemical Energy Conversion and Storage. 2018;15:041008,1-7.

[P4] ANDERSSON M, YU J, BEALE SB, FRONING D, LEHNERT W.
Multiscale Multiphase Simulations at the Gas Channel/Gas Diffusion Layer Interface inside Polymer Electrolyte Fuel Cells.
EFC-17 European Fuel Cell Conference and Exhibition. 2017. Naples, Italy.

[P5] ANDERSSON M, BEALE SB, REIMER U, LEHNERT W, STOLTEN D.
Interface resolving two-phase flow simulations in gas channels relevant for polymer electrolyte fuel cells using the volume of fluid approach. Int. J. Hydrogen Energy. 2018;43:2961-2976.

[P6] ANDERSSON M, MULARCZYK A, LAMIBRAC A, BEALE SB, ELLER J, LEHNERT W, BÜCHI F.
Modeling and synchrotron imaging of droplet detachment in gas channels of polymer electrolyte fuel cells. J. Power Sources. 2018;404:159-171.

[P7] ANDERSSON M, VUKČEVIĆ V, ZHANG S, BEALE SB, JASAK H, LEHNERT W.
Modeling of Droplet Detachment using Dynamic Contact Angles in Polymer Electrolyte Fuel Cell Gas Channels. J. Hydrogen Energy. 2019;44:11088-11096.

[P8] ANDERSSON M, BEALE SB, FRONING D, YU J, LEHNERT W.
Coupling of Lattice Boltzmann and Volume of Fluid Approaches to Study the Droplet Behavior at the Gas Diffusion Layer/Gas Channel Interface. ECS Transaction. 2019;86(13):329-336.

Additional references

[A1] FERZIGER JH, PERIC M.
Computational methods for fluid dynamics. 2012. Springer Science & Business Media.

[A2] PATANKAR SV.
Numerical Heat Transfer and Fluid Flow. 1980. New York, USA. Hemisphere Publishing Corporation.

[A3] MARIC T, HOPKEN J, MOONEY K.
The OpenFOAM technology primer. 2014. SourceFlux.

[A4] MOUKALLED F, MANGANI L, DARWISH M.
The Finite Volume Method in Computational Fluid Dynamics: An Advanced Introduction with OpenFOAM® and Matlab. 2016. Springer International Publishing Switzerland.

[A5] PATANKAR SV, SPALDING DB.
A Calculation Procedure for the Transient and Steady-state Behavior of Shell-and-tube Heat Exchangers, in Heat Exchangers: Design and Theory Sourcebook. N. Afgan and E.U. Schlünder, Editors. 1974, Scripta Book Company: Washington. D.C. 155-176.

[A6] BEALE SB, ZHUBRIN SV.
A distributed resistance analogy for solid oxide fuel cells. In CHT-04, ICHMT International symposium on advances in computational heat transfer. 2004. Norway.

[A7] KULIKOVSKY AA.
Analytical modelling of fuel cells. 2010. Elsevier.

[A8] WELLER HG, TABOR G, JASAK H, FUREBY C.
A tensorial approach to computational continuum mechanics using object-oriented techniques. Computers in Physics. 1998;Vol.12(6):620-631.

Improvement of Flamelet Models for the Prediction of Soot Emissions from Aero Engines using LES

Project ID: jara0173
HEINZ PITSCH
Institute for Combustion Technology (ITV),
RWTH Aachen University

To exploit the potential of computational modeling for the reduction of particulate emissions from aero engines, reliable modeling frameworks have to be developed and tested in system scale applications. Therefore, Large Eddy Simulation (LES) of soot formation in a model aero engine combustor experimentally investigated at the DLR havebeen conducted using a flamelet-based combustion model and a detailed soot model. A visualization of the complex interaction between the flame and the underlying turbulent flow field is highlighted in figure 1 that shows the temperature field in the combustion chamber. For this project, several simulations have been performed on the JARA clusters for different operation points. In addition, data from Direct Numerical Simulations performed before at the ITV in Aachen have been used to identify shortcomings and to improve the LES modeling, which resulted in a better agreement between the simulation results. Figure 2 shows a qualitative comparison between the measured average soot volume fraction and the corresponding result obtained in the LES.

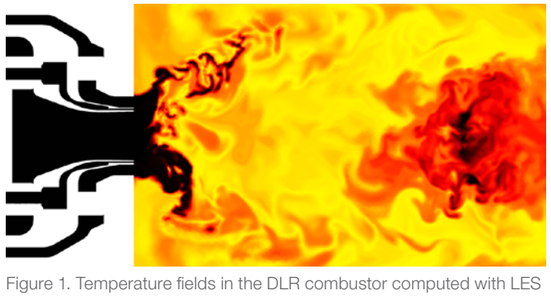

Figure 1. Temperature fields in the DLR combustor computed with LES

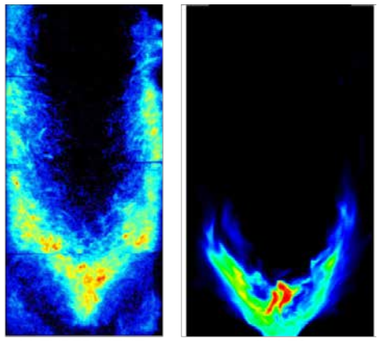

(a) EXPERIMENT (b) LES

Figure 2. Comparison of experimental and computed soot volume fraction

Publications:

- WICK A, ATTILI A, BISETTI F, PITSCH H.
  DNS-driven analysis of the flamelet/progress variable model assumptions on soot inception, growth, and oxidation in turbulent flames. Comb. and Flame 2019.

Selected conference participations

- A. WICK, K. KLEINHEINZ, L. BERGER, H. PITSCH.
  Modeling of emissions in gasturbines.
  FVV 2018 Autumn Conference, Würzburg, Germany, September 27-28, 2018
- A. WICK, A. ATTILI, F. BISETTI, H. PITSCH.
  DNS-Driven Analysis of Flamelet-Based Turbulent Soot Models for LES.
  12th International ERCOFTAC Symposium on Engineering Turbulence Modelling and Measurements, Montpellier, France, September 26-28, 2018

National and international cooperations

- Michael Mueller, Princeton University, USA
- Fabrizio Bisetti, University of Texas at Austin, USA

Investigation of Spray Combustion of Oxymethylenethers and Oxymethylenether/Diesel Blends using Large Eddy Simulations

Project ID: jara0174
HEINZ PITSCH
Institute for Combustion Technology (ITV),
RWTH Aachen University

Synthetic CO_2-neutral fuels, such as Oxymethylenethers (OME_X), are a promising way to decarbonization of the transport sector. They can substitute currently used fuels in diesel engines while suppressing the formation of soot, without soot/NOX tradeoff.

OME_X of short chain length have, however, significantly different fuel properties such as higher vapor pressure, lower viscosity, and lower Cetane number compared to conventional diesel fuel. As these properties are known to have large impact on injection and ignition behavior, predictive and affordable simulations of spray injection and combustion are required to optimize existing engines with respect to engine design and control for OME_X fuels.

Within this work, real liquid fuel properties and newly developed chemical reaction mechanisms are combined in high-fidelity large-eddy simulations (LES) of spray injection and combustion of OME_X under engine-relevant conditions for the first time. Simulations have been performed for both OME_1 and OME_4. Integral mixing and combustion quantities, such as spray penetration, spray angle, ignition delay time, and lift-off length, as well as instantaneous flow fields are compared with experimental results obtained in a high-pressure spray chamber.

For this project, simulations were performed in a range between 240 and 960 cores. The inert simulations, used to tune spray breakup parameters for different fuels, were run on an average of 480 cores as originally proposed. For the reactive simulations, which have a higher memory demand and are computationally more expensive, the good scalability of the code was used to utilize a higher number of cores, up to 960.

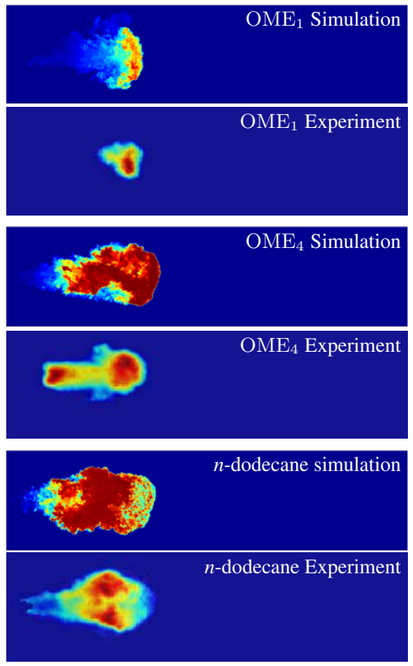

Liquid penetration length of the spray core and the gaseous penetration length of the fuel into the domain evaluated in the simulations are reasonably close to the experimental results, as well as the spray angle and structure are properly reproduced in the simulations.

Figure 1 shows OH chemiluminescence measurements and corresponding post-processed simulation results shortly after ignition in comparison. Ignition occurs in lean regions close to the spray tip in both simulation and experiment, with the simulation being faster in comparison. Accordingly, the flame lift-off length is also slightly under predicted.

Figure 1. Line-of-sight integrated OH mass fraction in simulations compared to instantaneous experimental OH*-chemiluminescence visualizing the spray flame 1 ms after start of injection.

PhD-thesis: Distribution of thermo-electric energy systems within city districts under uncertainty

Project ID: rwth0227
JAN SCHIEFELBEIN
Institute for Energy Efficient Buildings and Indoor Climate,
E.ON Energy Research Center,
RWTH Aachen University

Scope of work:
City districts offer great potential for greenhouse gas emission reduction. Urban energy system planning can support the identification of low-emission, cost-efficient solutions. However, planning objectives are sensitive to uncertain factors. Classical approaches, such as stochastic optimization or robust optimization, are either too computationally intensive on urban scale or do not allow the maximization of the objective function stability. Thus, ways to account for both objective function value optimization and sensitivity minimization have to be found.

Solution approach:
A genetic algorithm (GA) is combined with an uncertainty calculator to solve the energy balance and economic equations of an urban energy system. The aim is to identify urban energy system configurations (such as type, location, and size of device), which minimize both the mean and standard deviation of cost and emission values for different risk-attitudes of the decision maker. Uncertain factors related to user behavior, weather, building physics, energy system efficiencies, and economic parameters are taken into account. The evaluation, which includes the energy balance and economic calculation, is repeated for a specific number of sample sets of uncertain parameters for each individual (in this case urban energy system configurations), leading to a distribution of cost and emissions. These distributions are finally converted to a single fitness function value, based on the risk-attitude of the decision maker. The fitness function values are used for selection of superior individuals.

Implementation and HPC usage:
The chosen optimization and evaluation method is suitable for computational parallelization. Each optimization run is executed on a 32 core smp-l-bull machine of the RWTH Aachen University Compute Cluster, requesting 254 GB RAM per job. The parallelization is done with the Python library SCOOP using 32 parallel processes. In this case, parallelization means the parallel evaluation of different individuals. Each cluster job is limited to a maximum of 5 days runtime. Adjacent jobs are initialized with the final population of the prior job.

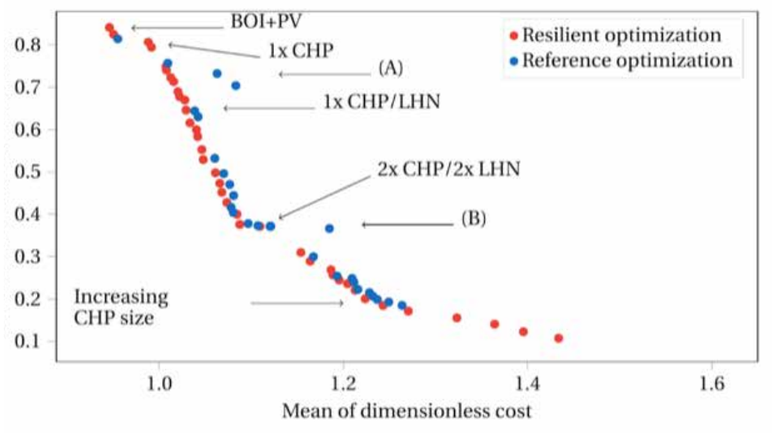

Figure 1: Dimensionless cost and emissions for resilient and reference optimization

Example results:
The resilient optimization (GA plus uncertainty calculator) is compared with the performance of a reference model. The reference model includes an energy system optimization without uncertainty and a subsequent uncertainty calculation. Figure 1 shows the example results.

The results demonstrate, that resilient and reference optimization lead to comparable results. Low-cost solutions mainly include boiler (BOI) units with photovoltaic (PV) modules, while further emission reduction is achieved with combined heat and power (CHP) usage and the connection of local heating networks (LHN). However, labels A and B mark three reference energy system solutions, which perform worse under uncertainty. In this case small scale CHP systems have been identified as pareto-optimal solutions. These small-scale CHP systems perform well for the chosen reference scenario. However, they are highly sensitive to changes in uncertain demands, as variations in demand can strongly impact the CHP electric energy self-consumption rate of the building, resulting in a reduced average economic and ecological performance.

Further results show that the resilient optimization model is capable of reducing the cost and emission standard deviation for risk-averse attitudes at the disadvantage of lower mean cost and emissions. The presented tool is able to identify advantageous urban energy system solutions and generate insights in the behavior of their objective function values under uncertainty.

Low Emission Design Comprehensive simulation of direct injection, mixture formation and combustion for the analysis of the cause-and-effect chain from the injector to the formation of raw emissions.

Project ID: bund0002
ROMUALD SKODA
Chair of Hydraulic Fluid Machinery,
Ruhr-Universität Bochum

The subproject is part of a comprehensive project which aims at the assessment of influencing parameters of the direct injection system on the subsequent processes of mixture formation, combustion and emissions by highly-resolved numerical simulation. Out part is to investigate a complete injection cycle of a close-to-production heavy-duty 9-hole Diesel injector with a full 360° model from the in-nozzle flow up to the primary breakup for the assessment of real geometry, cavitation and turbulence impact on the primary liquid jet breakup at realistic conditions in terms of injection and gas pressure, nozzle geometry and needle motion. The injection cycle does not contain a pronounced full lift phase what is typical for pilot injection.

A pressure-based incompressible three-phase flow solver was developed in the OpenFOAM framework and optimized for small time steps (~ 1 ns) and highly-parallel simulations. The primary breakup of fuel ligaments from the liquid core is directly resolved down to the available spatial resolution (~ 2.5...5 µm) by a volume-of-fluid method [1] with a finite volume grid of about 100 Mio cells. A large eddy simulation is applied for resolution of large turbulent scales with an eddy-viscosity sub grid scale model (WALE [2]). Cavitation is taken into account by a mass transfer model based on the Rayleigh equation and a volume fraction transport equation [3]. The close-to-nozzle spray region is validated on laser induced fluorescence (µLIF) measurement data from our project partners [4].

Essential features of the liquid jet-break-up as e.g. wavy jet surface structures due to Kelvin-Helmholtz instabilities are resolved (Figure 1). A vortex structure evaluation is presented in Figure 3 by the Q-criterion [5] for a sequence of snapshots of different needle positions. During the opening phase many small vortices are observed in the nozzle bore, while at the short full lift phase a significantly larger string-shaped vortex structure can be discerned which is directly associated to the cavitation structures, i.e. cloud and string cavitation at low and high needle lift, respectively. At full-lift, significant deviations to vortex structures of a quasi-stationary full-lift simulation occur, which reveals the highly-unsteady flow field generated mainly in the opening phase by cloud cavitation. This unsteadiness survives far into the closing phase – even at 65 % lift during the closing phase, the vortex structure appears more unsteady than for quasi-steady conditions. At 50 % lift (not shown), transient effects start to increase again. A statistical evaluation of ligaments in terms of a probability density function (PDF) showing the probable radial location of a ligament confirms the highly unsteady flow structure (Figure 2). The distribution for the needle lift range from 72% to 48% is close to that of the quasi-stationary simulation, where ligaments are more likely to occur at smaller radius due to less transient flow. Hence, also for the ligament positions nearly quasi-stationary behavior is observed only far after the full-lift phase been passed, well within the closing phase.

These results reveal the close interaction of cavitation and turbulent vortex dynamics and the high impact of the nozzle needle dynamics on primary break-up of high-pressure direct injection systems.

Figure 1: Representative quasi stationary simulation snapshot visualized by isosurface of liquid volume fraction with value α = 0.5.

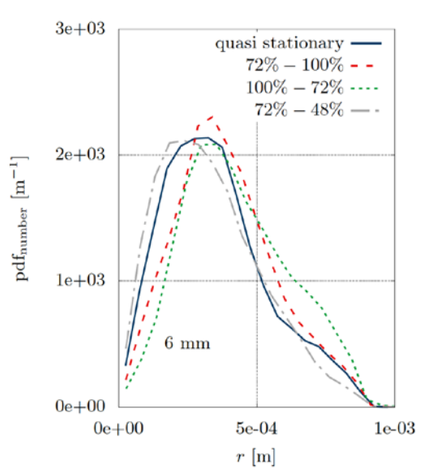

Figure 2: Radius PDF, which characterizes the position of ligaments for three needle lift ranges of the transient simulation and for the quasi-stationary simulation. Ligaments have been evaluated in a plane 6 mm downstream of the nozzle bore exit.

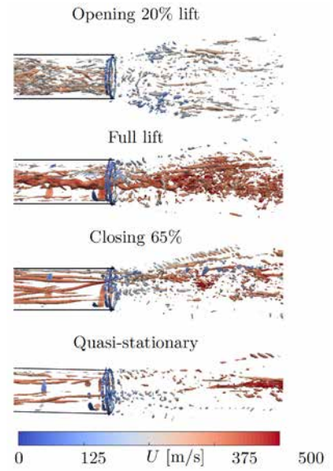

Figure 3: Isosurface of Q-criterion with value Q = 4 × 1013 1/s2 colored by magnitude of velocity for three representative time instances of the transient simulation and a typical snapshot of the quasi- stationary simulation at full lift.

References

[1] HIRT C, NICHOLS B.
Volume of fluid (VOF) method for the dynamics of free boundaries. Journal of Computational Physics. 1981;39(1):201– 225. doi:10.1016/0021-9991(81)90145-5.

[2] NICOUD F, DUCROS F.
Subgrid-scale stress modelling based on the square of the velocity gradient tensor. Flow, turbulence and Combustion. 1999;62(3):183–200.

[3] SCHNERR GH, SAUER J.
Physical and numerical modeling of unsteady cavitation dynamics. Fourth international conference on multiphase flow. ICMF New Orleans, 2001. 2001;Vol.1.

[4] WENSING M, WEISS L.
Tech. rep. Chair of Technical Thermodynamics. Friedrich-Alexander-Universität Erlangen-Nürnberg. Personal communication. 2018, Erlangen.

[5] HUNT JC, WRAY AA, MOIN P.
Eddies, streams, and convergence zones in turbulent flows. Tech. Rep. CTR-S88. Center for Turbulence Research. 1988.

Materials Engineering | DFG 405

Discrete Element Simulation of Granular Flow and Filling

Project ID: rwth0248
CHRISTOPH BROECKMANN
Institute for Materials Applications in Mechanical Engineering (IWM), RWTH Aachen University

Hot Isostatic Pressing (HIP) is a process to densify powder or cast and sintered parts in a furnace at relatively high pressure (100-200 MPa) and moderate temperatures (compared to traditional sintering temperature) of metals or ceramics. However, the prediction of the final shape of the HIPed components is important but still influenced by numerous factors, such as shape of the capsule, size of the powder particle, initial powder distribution after filling, material properties, HIP process parameters. With the improved simulation capabilities, the Discrete Element Method (DEM) was developed and applied to simulate the powder technological process. Nowadays, the powder filling and following pre-consolidation process (vibration and tapping) are also possible to be simulated by DEM, so that the density distribution in the HIP capsules can be numerically predicted.

A case study in this section considers only mono-sized spherical particles with a radius of 125 µm in the simulation to represent the powder. The material properties, such as density, static and rolling friction coefficient, of stainless steel 316L were obtained from literature. The calibration and validation were conducted by a flowmeter test. This DEM model was extended to simulate a powder filling process of 2.0×10^7 particles in a cylindrical steel capsule, without the consideration of the pre-consolidation processes such as vibration or tapping.

The external force, i.e. gravity, and the inter particle force, i.e. friction, were also applied in simulation model. The problem was solved in particle dynamics simulator, LIGGGTS. The powder was inserted firstly in a funnel and then flowed into the capsule (Figure 4 (b)). The cross-sectional view on the plane Z=0 of selected intermediate steps during filling are shown in Figure 4 (c) and (e). With in-house written scripts, the real-time relative density distributions can be mapped into a three-dimensional diagram Figure 4 (d) and (f)).

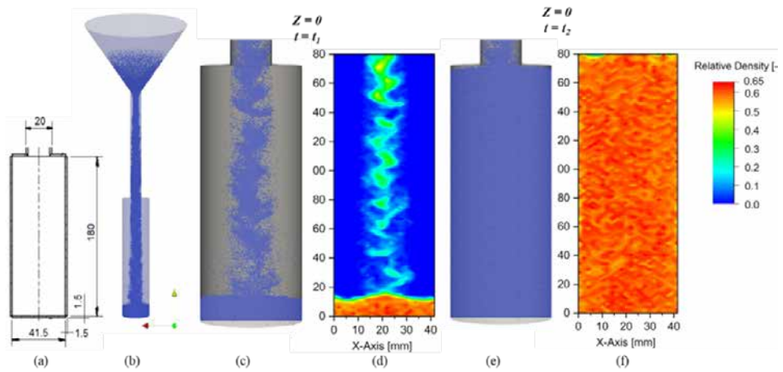

Figure 1: Filling process using DEM Simulation: (a) capsule geometry, (b) visualization of the filling process, (c) visualization and (d) exported density distribution of the cross section at intermediate step, (e) visualization and (f) exported density distribution of the cross section at the filling end.

Publications:

- DENG Y, KALETSCH A, BEZOLD A, BROECKMANN C.
  Precise prediction of near-net-shape HIP components through DEM and FEM simulation. In Proceedings of 12th International Conference of Hot Isostatic Pressing. Sydney, Australia. 2017. DOI: 10.21741/9781644900031-24.
- DENG Y, et al.
  Numerical studies of the scale-up of multi-material inert electrode production by HIP cladding. In Proceeding of EuroPM2018. Bilbao, Spain. 2018.
- KALETSCH A, et al.
  Process Simulation and Prediction of Fracture Probability in Powder Technology. Ceramic Applications. 2018;Vol.1,no.6:58–63.

Materials Science | DFG 406

Quantum mechanically guided materials

Project ID: jara0131
JOCHEN M. SCHNEIDER
Materials Chemistry
RWTH Aachen University

M. HANS
S. LIU, S. EVERTZ
J.-O. ACHENBACH
M. AMALRAJ
S. PRÜNTE
A. SAKSENA
AND L. ELALFY
Materials Chemistry,
RWTH Aachen University

Introduction
This application for computing time pertains to the peer-reviewed DFG research projects SPP 1594, SCHN 735/34, SCHN 735/35, and HU 2269/10. Besides state of the art experimental research work, our research activities “Quantum mechanically guided design of ultra-strong metallic glasses” (SPP 1594), “Quantum mechanically guided design of precious metal coatings for glass forming” (SCHN 735/34), “Quantum mechanically guided design of X2BC nanolaminates” (SCHN 735/35), and “Quantum mechanically guided design of negative thermal expansion materials” (HU 2269/10) heavily rely (as the titles suggest) on quantum mechanical data. Extensive calculations have to be carried out to insure that the objectives can be met. As we hold no CPU grants at other sites, the continuation of these DFG funded projects critically depends on the allocation of sufficient computational resources to these research activities.

In the following text the vision, research goal, and strategy of Materials Chemistry, (MCh, Lehrstuhl für Werkstoffchemie) are briefly described.

Vision: Quantum mechanically guided materials design
Goal: To contribute towards the basic understanding required to realize the synthesis and application of tailor-made multi-functional and structural materials with chemical and mechanical stability. The focus is on understanding the correlation between synthesis conditions and the structure and chemistry evolution, for designing elasticity and phase stability as well as most recently transport properties and self-healing as well as self- reporting ability. Targeted application fields are besides metal cutting and forming also tribological contacts as well as energy conversion.

Strategy & Methods:
The research strategy is to employ computational tools based on ab initio methods providing a description of phase stabilities, elastic properties, and transport properties. In situ chemistry and energy probes are utilized during ionized vapor deposition to gain understanding of the correlation between the synthesis conditions and the structure and chemistry evolution. Ex situ techniques are employed for complementary structure and chemical analysis as well as for the characterization of the film properties.
Through combination of theory and experiment we seek to understand the plasma-material interactions and to contribute towards the scientific basis that will allow for designing materials with respect to phase stability and elastic properties. Thin film combinatorics[1] is employed to address the challenges posed above: By co-deposition from multiple plasma sources we produce thin films with concentration gradients which are then spatially resolved with respect to composition, structure, elastic properties, and phase stability. This experimental research strategy is applied in an iterative fashion combined with the theoretical materials descriptions based on quantum mechanics to allow for knowledge based-materials design as outlined in Fig. 1.
Past engineering science achievements include contributions towards understanding the correlations between:

(i) elastic properties and electronic structure of nanolaminates, incl. MAX phases,
(ii) phase stability and plasma chemistry/energetics of various oxides,
(iii) phase stability, elastic properties, and electronic structure of transition metal nitrides and carbides, as well as
(iv) decohesion energy and electronic structure of solid lubricants,
(v) elastic properties and electronic structure of hydroxyapatite,
(vi) short range order, elastic properties, and electronic structure of metallic glasses as well as metallic alloys, and
(vii) transport properties and electronic structure of thermoelectrics.

These correlations constitute the scientific basis for quantum mechanically guided materials design.

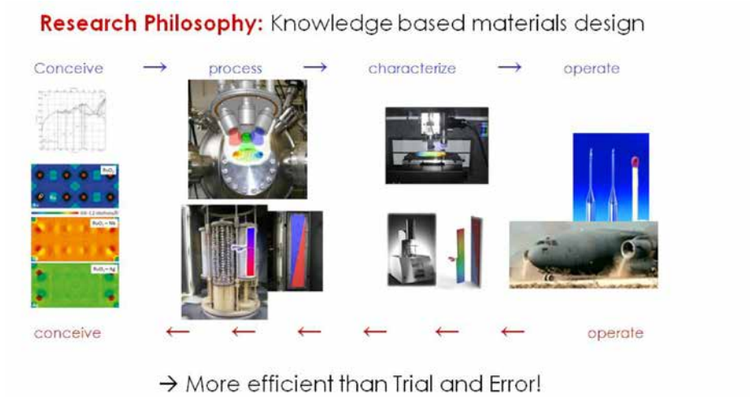

Fig. 1. Research philosophy. Image is indicating the iterative character of the materials design approach by blue and red arrows.

Preliminary work
The principle investigator has strong publication records: h-index 40, > 6500 citations (http://www.researcherid.com/rid/A-4701-2012). Many physical and chemical properties, ranging from elastic[2], plastic[3], magnetic[4], to transport properties[5], as well as complex phenomena, ranging from surface interactions with environment[6] and workpiece materials[7], to growth related phenomena [8], were investigated in these publications. The majority of these publications are based on quantum mechanical predictions, which are validated experimentally on thin films and bulk materials. Our correlative approaches have recently been described in an invited review [9]. It should be noted that even computationally very demanding amorphous materials were explored at MCh [10,11]. The principle investigator was named fellow of the American Vacuum Society in 2013 and Max Planck Fellow and RWTH Fellow in 2015. Recently, a 3 million € atom probe tomography platform was installed at MCh, enabling 3D chemical composition analysis. Atom probe tomography data elevate the quality of our structural and functional materials design activities and enable the transition from macroscopic materials design to design of nanostructured materials. It is our ambition to include composition modulations, for example over interface boundaries, in our quantum mechanical models. Hence, the computational time required to provide guidance for materials design activities on the atomic scale is compared to our past activities significantly enlarged.

In particular, we are very experienced with quantum mechanically guided design of materials systems explored in this projects. These systems are related in terms of phase stability tuning and hence merged in a single JARA application. Regarding metallic glasses, we have so far investigated many important aspects, ranging from mechanical[11-15] and magnetic properties[16] to structure evolution[10,17]. For the glass forming activities within this JARA project, interfaces are central and have been extensively studied at MCh[18-20]. Mo2BC based nanolaminates are a core of MCh expertise[21-23]. Regarding negative thermal expansion materials for thermoelectric applications, MCh has made important contributions on thermoelectric materials[24-26] and quantum mechanical treatment of thermal expansion[17,27,28].

Description of the project

Project details

Quantum mechanically guided design of ultra-strong metallic glasses

Metallic glasses exhibit high strength, approaching the theoretical strength limit, high capacity for elastic energy storage per unit volume or mass, low damping, and high toughness[29-36]. It has been suggested that the origin for the ultrahigh strength of metallic glasses is within the strong bonding nature among the constituents[32]. In particular, Co-based bulk glassy alloys have high mechanical strength and stiffness as well as good soft magnetic properties. Metallic glasses were developed mostly based on phenomenological glass forming rules. As quantum mechanical calculations of materials in the glassy state are very challenging, most topological descriptions of metallic glasses are so far based on reversed Monte Carlo approaches. Hence, basic physical and chemical materials design principles for metallic glasses have not been identified. This project aims at identifying and understanding these principles to realize future knowledge-based design of metallic glasses with high strength and stiffness as well as toughness. We will systematically explore the influence of the chemical composition on the electronic structure, topology, stiffness, and toughness. These amorphous configurations will be obtained by the so-called liquid-quench algorithm[9], which is computationally very demanding. The quantum mechanical molecular dynamics data for many glassy systems are compared to the experimental data of the stiffness, the elastic-plastic transition, the density, and the chemical order. Topological and chemical ordering is analyzed by atom probe tomography. Regarding the topology of metallic glasses, a key pathway to validate quantum mechanical predictions, synchrotron based analysis is required and hence there is fruitful collaboration established with researchers at DESY in Hamburg.

Quantum mechanically guided design of precious metal coatings for glass forming

During the isothermal precision glass molding, coated molding tools are exposed to a dynamic set of stress and frictional loads between a glass and a coating. As a result, precious metal coatings applied so far, typically fcc Pt-based solid solutions[37|, often exhibit characteristic glass adhesion, whereby the underlying physical mechanisms leading to adhesion are currently not understood. Hence, a knowledge-based approach for the reduction of adhesion by adjustment of the coating system is not available. The trial-and-error approaches currently applied are time, material, and cost intensive and did not lead to a breakthrough regarding the reduction of glass adhesion. The aim of this project is to identify the reasons for glass adhesion on precious metal coatings under typical process conditions using quantum mechanical tools. Within the project, fundamental mechanisms for glass adhesions for a commonly used glass (B270, modified soda-lime glass) will be identified by a quantum-mechanical description of the interactions on an atomic scale. Based on these interactions, alternative coating compositions will be proposed and validated experimentally.

Quantum mechanically guided design of X_2BC nanolaminates

Mo_2BC (space group Cmcm) is a promising material for cutting and forming applications.[21] In this project, in situ synchrotron x-ray diffraction experiments and small scale mechanical studies supported by electron microscopy will be conducted to delineate the relationship between coating stress and strain with the plastic behavior of Mo_2BC. We seek to identify the fundamental mechanisms that govern the plastic behavior of X_2BC nanolaminates (X = Hf, Mo) and compare these results to previously published and quantum mechanical predictions in this project. Since our initial micro-mechanical data support the notion of moderate ductility predicted by the quantum mechanical calculations, this project aims at answering the following questions linking microstructural characteristics with the mechanical properties: 1. Does the microstructure of X_2BC nanolaminate (X = Hf, Mo) coatings influence their mechanical behavior? 2. What deformation mechanisms are active in X_2BC nanolaminates (X = Hf, Mo)? Typically, layered solids such as MAX phases are known as plastically anisotropic materials. Upon loading, such solids deform by glide of basal plane dislocations. Based on post mortem microscopy experiments, we aim for the characterization of the dislocations structure and its interaction with other microstructural features in order to identify and understand the deformation mechanism active in amorphous and nanocomposite (nanocrystals in an amorphous matrix) and fully crystalline X_2BC coatings. 3. Does the Cauchy pressure serve as a predictor for the plastic behavior of X_2BC nanolaminates (X = Hf, Mo)? While Mo_2BC was predicted to behave moderately ductile, Hf_2BC is expected based on the Cauchy pressure to be brittle.[22] Hence, a comparative investigation of these two nanolaminate systems will shed light on the question as to the predictive capability of the Cauchy pressure and potential limits thereof for nanolaminates. We also intend to investigate related nanolaminates.

Quantum mechanically guided design of negative thermal expansion materials

Thermoelectrics offer an attractive pathway for addressing an important niche in the globally growing landscape of energy demand, since they can convert heat and, in particular waste heat, to electricity.[38] In the past decades, searching for high efficiency thermoelectrics has been guided by the concept of phonon glass electron crystal.[38] Despite remarkable progress made under this concept, the energy conversion performance is still well below what is needed for thermoelectrics to compete with traditional electricity producing methods, primarily due to the nature of strong coupling between electronic and phononic transport.[38] This proposal aims at exploring a new area where the electronic and phononic transport can be decoupled, when negative thermal expansion material, pressure, and thermoelectrics meet together.

Negative thermal expansion materials have inherent nature that a large number of low frequency acoustic phonons possess strong phonon anharmonicity compared with less flexible materials, leading to very low intrinsic thermal conductivity, which is beneficial for thermoelectrics.[39] However, they have not been extensively studied for thermoelectric applications so far, due to the low thermopower or extremely low temperature range where negative thermal expansion normally occurs. Herewith we propose a new concept of applying pressure to enhance the thermoelectric coefficient by taking advantage of the unique feature that the electrical and phononic transport properties can be largely tuned in an opposite way.

The overall goal of this project is to advance the fundamental science underlying the electrical and phononic transport properties of some representative negative thermal expansion materials under mechanical compression and rationally performed doping and alloying as novel strategy for high efficiency thermoelectrics. Combined anharmonic lattice dynamics based on first principles and the Boltzmann transport equation are proposed as approaches to this end. The result of these investigations is likely to provide a major advancement to rational optimization of thermoelectrics based on negative thermal expansion materials, with the potential to make a clear contribution to the energy needs of the future. The novelty of this project manifests itself in that, applying pressure to negative thermal expansion materials not only reduces the lattice thermal conductivity by augmenting phonon anharmonicity, but also largely enhances their thermopower and pushes the negative thermal expansion range upward to higher temperatures, which in turn achieves decoupling the electrical and phononic transport in thermoelectrics and results in significant improvement in thermoelectric performance. Such opposing effects have never been realized in traditional methods for optimizing thermoelectric materials, where the electrical and phononic transport are always strongly correlated and act in unison.

Review processes

The projects in this computational time proposal have already undergone rigorous scientific reviews or are at final review stages at DFG. DFG funding is provided under SPP 1594

(until December 2018), SCHN 735/34 (until July 2018, but the extension proposal has already been submitted to DFG and should be continued for additional two years), SCHN 735/35 (until September 2019), and HU 2269/10 (until February 2020). **It is central to obtain the requested computational resources to successfully carry out these research activities. Currently, we seek for DFG funding possibilities to extend our quantum mechanical design activities regarding metallic glasses (SPP 1594) and it is crucial to have computational support to enable these efforts.**

Numerical methods and algorithms

Density functional theory[40] will be used in this JARA project. We will use standard methodology and do not plan to develop density functional theory based numerical methods and algorithms. The central task of density functional theory is to solve the Schrödinger equation for a material system, which can be written in the following way using atomic units:

$$H\Psi=E\Psi, \quad (1)$$

where H is the Hamiltonian operator defined as:

$$H = -\frac{1}{2}\sum_{i=1}^{N}\nabla_i^2 - \frac{1}{2}\sum_{A=1}^{M}\frac{1}{m_A}\nabla_A^2 - \sum_{i=1}^{N}\sum_{A=1}^{M}\frac{Z_A}{|R_A - r_i|} + \sum_{i=1}^{N}\sum_{j>i}^{N}\frac{1}{|r_i - r_j|} + \sum_{A=1}^{M}\sum_{B>A}^{M}\frac{Z_A Z_B}{|R_A - R_B|}, \quad (2)$$

and E,Ψ, m, M, and N designate the total energy of the system (eigenvalue), wavefunction, mass, number of nuclei (ions), and electrons, respectively.[41] Density functional theory is based on Hohenberg and Kohn theorems demonstrating that the groundstate electronic energy is a functional of a unique groundstate electron density.[40] This allows simplifying the all-electron many-body problem of Eq. (2) into a single-particle equation.[40] Even though this appears to be a crude approximation, Hohenberg and Kohn have proven this to be an exact solution of Eq. (1) and Kohn won the Nobel Prize for it in 1998. A challenge to attain accurate expressions for electron density functional, $E[\rho]$, is a result of the complexity of the many-body problem. A solution is known as the Kohn-Sham equations:[42]

$$E[\rho(r)] = T[\rho(r)] - \sum_{A=1}^{M} Z_A \int \frac{\rho(r)}{|R_A - r|} d^3r + \frac{1}{2}\iint \frac{\rho(r)\rho(r')}{|r - r'|} d^3r d^3r' + E_{xc}[\rho(r)], \quad (3)$$

$H_e=T+U_{eff}$

where T is the kinetic energy functional of a non-interacting electron gas in its groundstate, the second term is again the nucleus-electron interaction, the third term is the average electrostatic potential energy for the electrons, and the remaining many-body electron-electron interaction effects are gathered into the exchange-correlation energy functional $E_{XC}[\rho]$, for which the exact form is unknown. The last three terms of Eq. (3) represent an effective potential (U_{eff}). The remaining intricate electron-electron interaction effects, inherent to the many-body Schrödinger equation, are contained in $E_{XC}[\rho]$. It is viable to make simple and efficient approximations for the exchange-correlation energy and the simplest of these is the local density approximation.[42] A step to improve it is to make the exchange and correlation energies dependent not only on the local electron density, but also on the derivatives of the density. Such semi-local method is known as the generalized gradient approximation.[43] Furthermore, two kinds of basis sets, trial wavefunctions, are commonly employed: (i) plane waves and (ii) localized orbitals.[44] In addition, quasiharmonic phonon calculations will also be carried out.[45] Within this method, a change in the crystal volume due to finite temperature is approximated by the change of the crystal volume at 0 K as a function of pressure. Hence, anharmonic effects are taken into account by the pressure dependence of the phonon frequencies.

Computer resources

Code performance and workflow

Two density functional theory[40] based codes will be used, which are both MPI parallelized. Commercially available Vienna ab initio simulation package (VASP) with projector augmented wave potentials,[46-48] parameterized within the generalized-gradient approximation by Perdew, Burke, and Ernzerhof[43] will be employed. In particular, we will use the VASP code under license number 5-94, version 5.4 (www.vasp.at). The total energy in the VASP code is treated within the Blöchl approach[49] applying the converged Monkhorst-Pack[50] k-points meshes in the Brillouin zone. Full structural optimization will be performed. The total energy convergence criterion in the VASP code is typically 0.01 meV within a 500 eV cut-off for the plane wave basis set. The second code used at MCh is OpenMX,[51] where density functional theory based molecular dynamics simulations can also be run. In particular, we will use the open-source OpenMX code, version 3.8 (www.openmx-square.org). The basis functions in this case possess the form of linear combination of localized pseudoatomic orbitals[52] and the generalized gradient approximation will be utilized.[43] The energy cut-off of 150 Ry and the real space grid technique[53] will be adjusted to reach the accuracy of 10^{-6} Ry/atom.

In this project, the VASP and OpenMX codes will be employed, based on density functional theory.[40] Density functional theory based codes scale with the power of three with respect to the number of electrons. This stems from diagonalization of a Hamiltonian with a dimension proportional to the number of elections and diagonalization is technically a power three procedure. The scaling behavior of VASP and OpenMX codes is provided in Fig. 2. Two observations can be made: (i) VASP is slower than OpenMX and (ii) the speedup of VASP larger than that of OpenMX. This is mainly due to basis sets used (projector augmented wave potentials in VASP and linear combination of localized pseudoatomic orbitals in OpenMX). Even though the VASP is slower, it has higher precision. In every run, where the computational precision cannot be sacrificed, for instance when magnetism is treated, VASP is used. It should be noted that for very large systems (more than 500 atoms), in OpenMX linear scaling methods can be employed so that the speedup data in Fig. 2 would support the use of OpenMX rather than VASP. Typically, we do not plan to run with more than 200 atoms and hence the speedup values in Fig. 2 are realistic for this project. To carry out phonon calculations, the open-source code Phonopy will be employed. We need **6.8 million core hours** (up to 120 core hours per job) to run this project. Typical job settings (chained execution) are as follows: 96 cores, up to 120 core hours/job, and 2 GB/core.

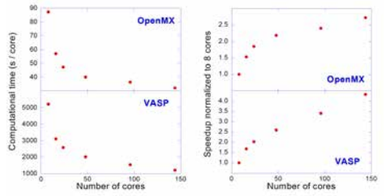

Fig. 2. Scaling behavior of VASP and OpenMX codes carried out within JARA0131 for a static TiAlN benchmark job (64 atoms). Number of cores used are typical for computational efforts at MCh. Static jobs are considerably faster than ionic relaxation jobs.

Justification of core hours requested

Subproject	Size (atoms)	Total steps	Total k core hours
Metallic glasses	120	200	1014
Precious metals	108	170	1313
X_2BC	96	720	2434
Negative expansion	64	14400	2074

Table 1. Requested time in the JARA project. Most of the computational time is spent for relaxation jobs, while there are many static jobs after each relaxation. All relaxation jobs need to run several times for 120 hours, which makes the computational demands very high.

Based on our experience (e.g. V_2AlC/Al_2O_3 interface[18]), about 1 mil core hours is required to describe an interface using quantum-mechanical methods. In this JARA project, we intend to work with several interfaces (e.g. Pt-based solid solution/glass) as well as computationally very demanding amorphous materials (e.g. metallic glasses) and phonon calculations. To describe the materials in this project, we have estimated our requirements (see Table 1) and with a detailed research plan above it is straightforward to understand the enormous computational demand. In particular, a detailed justification of our computational demands for each subproject is proved as follows.

Quantum mechanically guided design of ultra-strong metallic glasses
Shear softening in metallic glasses is not fully understood.[54] We seek for the electronic structure fingerprint of deformed Pd-Al-Y-M (M = Ni, Ir, Au) metallic glasses. The experimental validation will be carried out in a collaboration with Max-Planck-Institut für Eisenforschung GmbH. For the Ni-based system, we need to explore the role of magnetism so that two spin polarized configurations are considered in this case. This is in total 4 systems. These amorphous configurations will be obtained by the so-called liquid-quench algorithm,[9] which is computationally very demanding as approx. 120 atoms are needed for each composition. It requires melting (120 hours, 144 cores), quenching (120 hours, 144 cores), and 0 K relaxation (40 hours, 144 cores), followed by 6 static jobs at 0 K (10 hours each, 144 cores). This in total for 4 systems is 196 k core hours. At the corresponding ground states, we will calculate all elastic constants, which requires 10 static jobs for each system (10 hours per job, 144 cores). This is then 58 k core hours for the mechanical properties. To obtain the density of states for each system, 10 hours for each is necessary (144 cores), which is in total 6 k core hours. The key issue is to explore shear deformation of these configurations, which is computationally very demanding. To curry out this task, about 10 submissions (120 hours, 144 cores) are needed, which accounts for 691 k core hours for all 4 systems. Then, the density of states runs should be repeated (0 K relaxation (40 hours each, 144 cores), 6 static jobs at 0 K (10 hours each, 144 cores), density of states (10 hours for each, 144 cores)), which is 63 k core hours for all 4 systems. Hence, in total for this subproject, 1014 k core hours are required.

Quantum mechanically guided design of precious metal coatings for glass forming
During the isothermal precision glass molding, coated molding tools are exposed to a dynamic set of stress and frictional loads between a glass and a coating. As a result, precious metal coatings applied so far, typically fcc Pt-based solid solutions,[37] often exhibit characteristic glass adhesion. In the first stage of this project, phase stability and elastic property tuning of Pt-Ir-X (X = Rh, Re, Mo, Au, W, Hf, Ta, Ag, Cu) was carried out (see the JARA project report). Three concentrations of X will be explored for each Pt-Ir-X system containing 108 atoms. Growth aspects will be explored in the current computational period for one X element. (111) surfaces will be created using the slab model. This requires 120 core hours with 192 cores for each system, which is in total 69 k core hours. The bombarding X atoms will be placed 3 Å above the pristine surface, exploring 9 different sites (atop Pt, atop Ir, atop X, Pt – Pt bridge, Pt – Ir bridge, Pt – X bridge, Ir – Ir bridge, Ir – X bridge, and X – X bridge). Two different energies will be probed. The total molecular dynamics run time for each configuration is 2000 fs. To carry out these jobs, 192 cores will be employed and each job needs to be resubmitted three times for 120 hours, which accounts for all systems (all sites and energies) 1244 k core hours. It total for this subproject, this is 1313 k core hours.

Quantum mechanically guided design of X_2BC nanolaminates
MoAlB has a layered orthorhombic structure consisting of a molybdenum boride (MoB) sublattice, similar to that of the orthorhombic polymorph of MoB, interleaved by two Al layers (the unit cell contains 12 atoms).[55] It exhibits high electrical and thermal conductivities, room-temperature compressive strength close to 2 GPa, and is oxidation resistant.[55] Both the crystal structure and properties are similar to X_2BC nanolaminates (X = Hf, Mo).[21] Hence, we explore a correlation between electronic structure, defect structure, and elastic properties of this fascinating nanolaminate. We will systematically explore boron vacancies, Mo and Al antisites, as well as possible Mo substitutions with transition metals (Cr, Fe, and W). For this purpose, a 96 atom supercell should be considered. In total there are 13 configurations to be explored (3 for B vacancies, 4 for antisites, and 6 for substitutions (including additional spin polarization cases for Cr and Fe)). Each configuration needs to be relaxed (2 submissions with 120 hours each, 144 cores), lattice parameters must be determined (15 submissions with 20 hours each, 144 cores), elastic constants (9 independent values) should be calculated for each of these orthorhombic structures (36 submissions with 20 hours each, 144 cores), and the electronic structure will be obtained (2 submissions with 20 hours each, 144 cores). This is in total 2434 k core hours for all configurations to be explored in this subproject.

Quantum mechanically guided design of negative thermal expansion materials
Materials with negative thermal expansion coefficient exhibit in many cases low thermal conductivity.[56] Under pressure some materials change the behavior of thermal expansion.[56] Thermal transport of chalcopyrites have been explored in a lot of experimental and computational studies, where a temperature dependence was taken into account.[57,58] In this study, we intend to systematically explore different chalcopyrites ($InAgTe_2$, $InAgSe_2$, $InCuSe_2$, $InCuS_2$, $GaAgTe_2$, $GaCuTe_2$) and explain the reason behind the variations in the thermal conductivity. Chalcopyrites exhibit diamond-like structure with the composition I-III-VI_2, where the Roman numerals refer to groups in the periodic table of elements, with a conventional unit cell containing 16. Thermal conductivity for these materials are calculated by evaluating the second and third order force constants using the frozen phonon model,[59] where a set of displacements from the equilibrium position is induced (approx. 400 displacements for each system are required). The total energy of the displaced configurations is then evaluated using density functional theory and the software package VASP. From the 2nd and 3rd order force constants, the dynamical matrices are then constructed, which are the Fourier transformations of the force constants matrices providing the phonon distribution function. This phonon distribution function is then inserted in the Boltzmann transport equation[60] and being solved for the non-equilibrium case modeled using the relaxation time approximation and the open source code ShengBTE (http://www.shengbte.org/). In order to obtain the force constants, a 2x2x1 supercell has to be formed to the very least, so that a third neighbor cutoff radius in the range of 0.5 nm could be achieved. Hence, for each of the systems studied, for each pressure point, we need 400 single point DFT self-consistent calculation each with 64 atoms (144 cores, 1 hour each). For all 6 chalcopyrites and 6 different pressures for each system (hence 36 configurations), this is in total 2074 k core hours for this subproject.

Hence, for a meaningful materials design effort of materials in all subprojects we estimate that about 6.8 mil core hours are required.

Resource management and work schedule
Resource management
All computational resources will be managed by Marcus Hans, atom probe group leader at MCh. He will on daily basis monitor the resources (6.8 million core hours) and optimize their use. Both Jochen M. Schneider, and Marcus Hans monitor progress of the project and interpret the results together with the project contributors. We plan to publish the data in high-quality peer-reviewed journals. Furthermore, we aim at a significant improvement in management and handling of research data generated herein. We plan to implement a research data management system. This system will enable long-term archiving, curation, and the efficient reuse of these research data and constitutes a first significant step towards making these data accessible to national and international research organizations and communities. We aspire to implement state-of-the-art hardware and software as well

as new data management processes at MCh, which will go substantially beyond existing data handling procedures. We plan to use a system based on a commercial product lifecycle management (PLM) that can readily be adopted to scientific processes. We intend to link the existing data management system with our high performance computing data and complement it with a web-based direct search engine utilizing fuzzy logic similarity search algorithms for text and graphics. This will enable us to search the database and identify correlations between research datasets.

Subproject	November - January	February - April	May - July	August - October
Metallic glasses				
Precious metals				
X_2BC				
Negative expansion				

Table 2. Work schedule for this computational project. Quantum mechanically guided design is applied on ultra-strong metallic glasses, precious metal coatings, X_2BC nanolaminates, and negative thermal expansion materials.

Work schedule

The work schedule for the whole project (November 2018 – October 2019) is given in Table 2. The project requires **6.8 million core hours** (typically 120 hours per job).

Key personnel and experiences

Jochen M. Schneider, holds the chair of Materials Chemistry at RWTH Aachen University. He was awarded the Sofya Kovalevskaya Prize by the Alexander von Humboldt Foundation for excellence in thin film materials science. His research focuses on understanding material – plasma interactions for tailoring elastic properties, phase stability, as well as transport properties to enable quantum mechanically guided materials design. He is a Fellow of the AVS (Science and Technology of Materials, Interfaces, and Processing, formerly American Vacuum Society) and Max Planck Fellow at Max-Planck-Institut für Eisenforschung GmbH. He was appointed as guest professor for materials physics and materials chemistry at Uppsala University, Sweden, in 2017 and joined the editorial board of Scientific Reports (Nature Publishing Group) in 2016. Currently, he is serving as a member in the board of trustees of Leibniz Institute of Surface Engineering (IOM) in Leipzig.

Marcus Hans is the atom probe group leader at Materials Chemistry. He defended his dissertation in 2017 titled “Metastable cubic transition metal aluminum nitride and oxynitride coatings: Theoretical phase stability and defect structure predictions and verification by industrial- scale growth experiments.” His interests include quantum mechanically guided materials design of protective coatings. His skills comprise density functional theory and molecular dynamics. He has extensive experience in these computational methods, working with several codes, supervising theoretical projects and graduate students. Recently, an atom probe tomography platform was installed at MCh, enabling 3D chemical composition analysis and a transition from macroscopic materials design to design of nanostructured materials. Hence, both quantum mechanical and atom probe tomography insights from Marcus Hans are crucial for successful run of this project.

Bibliographic references

[1] GEBHARDT T, MUSIC D, TAKAHASHI T, SCHNEIDER JM. Thin Solid Films. 2012;520:5491.
[2] SHAHA KP, RUESS H, ROTERT S, TO BABEN M, MUSIC D, SCHNEIDER JM. Appl. Phys. Lett. 2013;103:221905.
[3] MUSIC D, HOUBEN A, DRONSKOWSKI R, SCHNEIDER JM. Phys. Rev. B. 2007;75:174102.
[4] TAKAHASHI T, MUSIC D, SCHNEIDER JM. J. Vac. Sci. Technol. 2012;A30:030602.
[5] MUSIC D, BASSE FHU, HAN L, DEVENDER, BORCA-TASCIUC T, GENGLER JJ, VOEVODIN AA, RAMANATH G, SCHNEIDER JM. Appl. Phys. Lett. 2014;104:053903.
[6] MUSIC D, SCHNEIDER JM. New J. Phys. 2013;15:073004.
[7] BOLVARDI H, MUSIC D, SCHNEIDER JM. Appl. Surf. Sci. 2015;332:699.
[8] MUSIC D, NAHIF F, SARAKINOS K, FRIEDERICHSEN N, SCHNEIDER JM. Appl. Phys. Lett. 2011;98:111908.
[9] MUSIC D, GEYER RW, SCHNEIDER JM. Surf. Coat. Technol. 2016;286:178.
[10] SCHNABEL V, BEDNARCIK J, MUSIC D, PAZUR T, HOSTERT C, SCHNEIDER JM. Mater. Res. Lett. 2015;3:82.
[11] SCHNABEL V, JAYA BN, KÖHLER M, MUSIC D, KIRCHLECHNER C, DEHM G, RAABE D, SCHNEIDER JM. Sci. Rep. 2016;6:36556.
[12] HOSTERT C, MUSIC D, BEDNARCIK J, KECKES J, KAPAKLIS V, HJÖRVARSSON B, SCHNEIDER JM. J. Phys. Condens. Matter. 2011;23:475401.
[13] SCHNABEL V, KÖHLER M, MUSIC D, BEDNARCIK J, CLEGG WJ, RAABE D, SCHNEIDER JM. J. Phys. Condens. Matter. 2017;29:265502.
[14] SCHNABEL V, KÖHLER M, EVERTZ S, GAMCOVA J, BEDNARCIK J, MUSIC D, RAABE D, SCHNEIDER JM. Acta Mater. 2016;107:213.
[15] SCHNABEL V, EVERTZ S, RUESS H, MUSIC D, SCHNEIDER JM. J. Phys. Condens. Matter. 2015;27:105502.
[16] HOSTERT C, MUSIC D, KAPAKLIS V, HJÖRVARSSON B, SCHNEIDER JM. Scr. Mater. 2012;66:765.
[17] EVERTZ S, MUSIC D, SCHNABEL V, BEDNARCIK J, SCHNEIDER JM. Sci. Rep. 2017;7:15744.
[18] SIGUMONRONG DP, ZHANG J, ZHOU Y, MUSIC D, EMMERLICH J, MAYER J, SCHNEIDER JM. Scr. Mater. 2011;64:347.
[19] HERRIG F, MUSIC D, VÖLKER B, HANS M, PÖLLMANN PJ, RAVENSBURG AL, SCHNEIDER JM. Metals. 2018;8:384.
[20] MUSIC D, SCHMIDT P, SAKSENA A. J. Phys. D. Appl. Phys. 2017;50:455502.
[21] EMMERLICH J, MUSIC D, BRAUN M, FAYEK P, MUNNIK F, SCHNEIDER JM. J. Phys. D. Appl. Phys. 2009;42:185406.
[22] BOLVARDI H, EMMERLICH J, TO BABEN M, MUSIC D, VON APPEN J, DRONSKOWSKI R, SCHNEIDER JM. J. Phys. Condens. Matter. 2013;25:045501.
[23] BOLVARDI H, EMMERLICH J, MRÁZ S, ARNDT M, RUDIGIER H, SCHNEIDER JM. Thin Solid Films.2013;542:5.
[24] MUSIC D, BASSE FHU, SCHNEIDER JM. Cryst. Growth Des. 2010;10:4531.
[25] MUSIC D, BASSE FHU, HASSDORF R, SCHNEIDER JM. J. Appl. Phys. 2010;108:013707.
[26] MUSIC D, GEYER RW, HANS M. J. Appl. Phys. 2016;120:045104.
[27] MUSIC D, GEYER RW, KEUTER P. Appl. Phys. Lett. 2016;09:223903.
[28] MUSIC D, BURGHAUS J, TAKAHASHI T, DRONSKOWSKI R, SCHNEIDER JM. Eur. Phys. J. B. 2010;77:401.
[29] DAS J, TANG MB, KIM KB, THEISSMANN R, BAIER F, WANG WH, ECKERT J. Phys. Rev. Lett. 2005;94:205501.
[30] WERNIEWICZ K, KÜHN U, MATTERN N, BARTUSCH B, ECKERT J, DAS J, SCHULTZ L, KULIK T. Acta Mater. 2007;55:3513.
[31] KLEMENT W, WILLENS RH, DUWEZ P. Nature. 1960;187:869.
[32] INOUE A, SHEN BL, CHANG CT. Intermetallics. 2006;14:936.
[33] ASHBY MF, GREER AL. Scr. Mater. 2006;54:321.
[34] LEWANDOWSKI JJ, GU XJ, NOURI AS, POON SJ, SHIFLET GJ. Appl. Phys. Lett. 2008;92:091918.
[35] INOUE A, SHEN B, KOSHIBA H, KATO H, YAVARI. Nat. Mater. 2003;2:661.
[36] HE G, ZHANG ZF, LÖSER W, ECKERT J, SCHULTZ L. Acta Mater. 2003;51:2383.
[37] TSENG SF, HSIAO WT, HUANG KC, CHEN MF, LEE CT, CHOU CP. Surf. Coat. Technol. 2010;205:1979.
[38] SNYDER GJ, TOBERER ES. Nat. Mater. 2008;7:105.
[39] SIKKA SK. J. Phys. Condens. Matter. 2004;16:S1033.
[40] HOHENBERG P, KOHN W. Phys. Rev. 1964;136:B864.
[41] SCHRÖDINGER E. Phys. Rev. 1926;28:1049.
[42] KOHN W, SHAM LJ. Phys. Rev. 1965;140:A1133.
[43] PERDEW JP, BURKE K, ERNZERHOF M. Phys. Rev. Lett. 1996;77:3865.
[44] HAFNER J. Acta Mater. 2000;48:71.
[45] LAZEWSKI J, JOCHYM PT, PIEKARZ P, PARLINSKI K. Phys. Rev. B. 2004;70:104109.
[46] KRESSE G, HAFNER J. Phys. Rev. B. 1993;48:13115.
[47] KRESSE G, HAFNER J. Phys. Rev. B. 1994;49:14251.
[48] KRESSE G, JOUBERT D. Phys. Rev. B. 1999;59:1758.
[49] BLÖCHL PE. Phys. Rev. B. 1994;50:17953.
[50] MONKHORST HJ, PACK JD. Phys. Rev. B. 1976;13:5188.

[51] OZAKI T, KINO H. Phys. Rev. B. 2005;72:045121.
[52] OZAKI T. PHYS. Rev. B. 2003;67:155108.
[53] SOLER JM, ARTACHO E, GALE JD, GARCIA A, JUNQUERA J, ORDEJON P, SANCHEZ-PORTAL D. J. Phys. Condens. Matter. 2002;14:2745.
[54] GREER AL, CHENG YQ, MA E. Mater. Sci. Eng. 2013;R74:71.
[55] KOTA S, ZAPATA-SOLVAS E, LY A, LU J, ELKASSABANY O, HUON A, LEE WE, HULTMAN L, MAY SJ, BARSOUM MW. Sci. Rep. 2016;6:26475.
[56] Ouyang T, Hu M. Phys. Rev. B. 2015;92:235204.
[57] WANG B, XIANG H, NAKAYAMA T, ZHOU J, LI B. Phys. Rev. B. 2017;95:035201.
[58] LEFÈVRE R, BERTHEBAUD D, MYCHINKO MY, LEBEDEV OI, MORI T, GASCOIN F, MAIGNAN A. RSC Adv. 2016;6:55117.
[59] MUSIC D, AHUJA R, SCHNEIDER JM. Phys. Lett. 2006;A356:251.
[60] CHAPUT L, LARROQUE J, DOLLFUS P, SAINT-MARTIN J, LACROIX D. Appl. Phys. Lett. 2018;112:033104.

Selected honors

- Since May 2018 Jochen M. Schneider is serving as a member in the board of trustees of Leibniz Institute of Surface Engineering (IOM) in Leipzig.

Conference contributions

- APARNA SAKSENA
  Metastable Phase Formation of Pt-X (X = Ir, Au) Thin Films,
  Contributed Talk at International Conference on Metallurgical Coatings and Thin Films (ICMCTF), San Diego, USA, April 23, 2018
- JOCHEN M. SCHNEIDER
  Combinatorial Thin Film Materials Science:
  Limitations and Opportunities for Combining Experiments and DFT Based Theory,
  Special Interest Talk at International Conference on Metallurgical Coatings and Thin Films (ICMCTF), San Diego, USA, April 23, 2018
- JAN-OLE ACHENBACH
  Low Temperature synthesis of Crystalline MoAlB Coatings by Combinatorial Direct Current Magnetron Sputtering, Contributed Poster at 14th International Ceramic Congress (CIMTEC), Perugia, Italy, June 08, 2018

National and international cooperations

- DIERK RAABE, Max-Planck-Institut für Eisenforschung GmbH, Germany
- KEKE CHANG, Chinese Academy of Sciences, China
- ULF JANSSON, Uppsala University, Sweden

Quantum mechanically guided design of wear-protective coatings for polymer forming tools

Project ID: jara0151
JOCHEN M. SCHNEIDER
Materials Chemistry,
RWTH Aachen University

M. HANS
D. M. HOLZAPFEL
H. RUESS
Materials Chemistry,
RWTH Aachen University

Scientific work accomplished and results obtained

This status report on the JARA computing time pertains to the peer-reviewed DFG research project SFB-TR 87. We have applied for 3.2 million core hours, but only 1.5 million core hours were granted, which limited the execution of this project. The following scientific work was accomplished within the granted period.

As TiAlN is a metastable solid solution of cubic TiN and hexagonal (wurzite) AlN. The first density functional theory study on TiAlN was conducted in 2003.[1] In this seminal work, ordered TiAlN supercells containing 8 atoms were considered and the Al solubility limit determined to be x = 0.7 in $Ti_{1-x}Al_xN$ (Al/Ti ratio of 2.3).[1] This is at first glance consistent with experimental observations, but there is a larger spread of reported experimental solubility, ranging from x = 0.4[2] to typically x = 0.7[3] and even up to x = 0.9.[4] To explain this disagreement, several approaches were introduced, and one is based on Al distribution in the metallic sublattice.[5] This clustering notion was validated by atom-probe tomography.[6-8] There are alternative explanations for the solubility spread, such as presence of an additional competitive phase,[9] N and metal vacancies,[10] or pressure induced solubility changes.[11,12] Clearly, more spatially resolved experimental analysis and new notions to refine quantum mechanical models are required.

It is well known that surface energy differences thermodynamically stabilize nanocrystalline γ-Al_2O_3 over α-Al_2O_3.[13] In this work, through correlative density functional theory calculations and advanced material characterization at the nanometer scale, we demonstrate that the metastable phase formation of nanocrystalline TiAlN, an industrial benchmark coating material, is crystallite size-dependent.[14] By relating calculated surface and volume energy contributions to the total energy, we predict the chemical composition-dependent phase boundary between the two metastable solid solution phases of cubic and wurzite $Ti_{1-x}Al_xN$.[14] This phase boundary is characterized by the critical crystallite size. Crystallite size-dependent phase stability predictions are in very good agreement with experimental phase formation data, where x was varied by utilizing combinatorial vapor phase condensation.[14] The wide range of critical Al solubilities for metastable cubic Ti_1-xAl_xN from 0.4 to 0.9 reported in literature and the sobering disagreement thereof with density functional theory predictions can at least in part be rationalized based on the here identified crystallite size-dependent metastable phase formation.[14] Furthermore, it is evident that predictions of critical Al solubilities in metastable cubic TiAlN are flawed, if the previously overlooked surface energy contribution to the total energy is not considered.[14]

We have also explored mechanical properties of these fascinating nitrides to a larger extent. Titanium and vanadium aluminum nitride and oxynitride coatings were deposited by high power pulsed magnetron sputtering.[15] The mechanical properties of these coatings were investigated by a combination of nanoindentation and micro-cantilever fracture toughness tests.[15] Additional modelling using cohesive-zone elements was done to produce useful reference data for future improvements based upon developments in coating architecture, such as multilayers, and in all cases a good agreement between experiment and model was found.[15] The measured elastic moduli show good agreement with those predicted by density functional theory calculations.[15] Based on the predicted and experimentally verified larger elastic moduli for the vanadium-based material systems compared to the titanium-based systems, the former systems are expected to exhibit larger values of fracture toughness.[15] Furthermore, as the nitride systems show larger elastic moduli as the corresponding oxynitride systems, larger fracture toughness values are expected for the nitrides.[15] These expected trends are reproduced in the experimental fracture toughness data.[15]

Realization of the project

The granted computing time has been used completely and we have not modified any codes run in this JARA project. We have employed the following density functional theory[16] based codes:

VASP (commercial code (license Nr. 5-94), version 5.4, www.vasp.at)

OpenMX (open-source code, version 3.8, www.openmx-square.org)

During the duration of this JARA project, 8 – 192 cores were used. In the course of structural relaxations at 0 K or density functional theory (*ab initio*) based molecular dynamics runs, maximum time (120 hours) was consecutively applied up to 10 times.

Publications with project results

(i) HANS M, MUSIC D, CHEN YT, PATTERER L, ERIKSSON AO, KURAPOV D, RAMM J, ARNDT M, RUDIGIER H, SCHNEIDER JM. Sci. Rep. 2017;7:16096.

(ii) GIBSON JSKL, REZAEI S, RUESS H, HANS M, MUSIC D, WULFINGHOFF S, SCHNEIDER JM, REESE S, KORTE-KERZEL S. Mater. Res. Lett. 2018;6:142.

Theses completed within the project

(i) BLIEM P. M.SC. Synthesis and characterization of Re-B thin films.

Additional references

[1] HUGOSSON HW, HÖGBERG H, ALGREN M, RODMAR M, SELINDER TI. J. Appl. Phys. 2003;93:4505.

[2] WAHLSTRÖM U, HULTMAN L, SUNDGREN JE, ADIBI F, PETROV I, GREENE JE. Thin Solid Films. 1993;235:62.

[3] RAUCH JY, ROUSSELOT C, MARTIN N. Surf. Coat. Technol. 2002;157:138.

[4] PRANGE R, CREMER R, NEUSCHÜTZ D. Surf. Coat. Technol. 2000;133-134:208.

[5] MAYRHOFER PH, MUSIC D, SCHNEIDER JM. J. Appl. Phys. 2006;100:094906.

[6] RACHBAUER R, MASSL S, STERGAR E, HOLEC D, KIENER D, KECKES J, PATSCHEIDER J, STIEFEL M, LEITNER H, MAYRHOFER PH. J. Appl. Phys. 2011;110:023515.

[7] JOHNSON LJS, THUVANDER M, STILLER K, ODÉN M, HULTMAN L. Thin Solid Films. 2012;520:4362.

[8] RACHBAUER R, STERGAR E, MASSL S, MOSER M, MAYRHOFER PH. Scr. Mater. 2009;61:725.

[9] HOLEC D, RACHBAUER R, CHEN L, WANG L, LUEF D, MAYRHOFER PH. Surf. Coat. Technol. 2011;206:1698.

[10] EUCHNER H, MAYRHOFER PH. Surf. Coat. Technol. 2015;275:214.

[11] ALLING B, ODÉN M, HULTMAN L, ABRIKOSOV IA. Appl. Phys. Lett. 2009;95:181906.

[12] HOLEC D, ROVERE F, MAYRHOFER PH, BARNA PB. Scr. Mater. 2010;62:349.

[13] MCHALE JM, AUROUX A, PERROTTA AJ, NAVROTSKY A. Science. 1997;277:788.

[14] HANS M, MUSIC D, CHEN YT, PATTERER L, ERIKSSON AO, KURAPOV D, RAMM J, ARNDT M, RUDIGIER H, SCHNEIDER JM. Sci. Rep. 2017;7:16096.

[15] GIBSON JSKL, REZAEI S, RUESS H, HANS M, MUSIC D, WULFINGHOFF S, SCHNEIDER JM, REESE S, KORTE-KERZEL S. Mater. Res. Lett. 2018;6:142.

[16] HOHENBERG P, KOHN W. Phys. Rev. 1964;136:B864.

Material suitable for the general public

We have demonstrated that surface energy contributions to the total energy must be considered for metastable phase stability predictions and the extent of c- and w-TiAlN phase stability regions is predominated by the crystallite size [M. Hans, D. Music, Y.-T. Chen, L. Patterer, A. O. Eriksson, D. Kurapov, J. Ramm, M. Arndt, H. Rudigier, and J. M. Schneider, Sci. Rep. 7, 16096 (2017)], a parameter which has been overlooked in the past. The here reported results provide an explanation for the sobering disagreement between density functional theory predictions and experimentally observed critical Al solubilities in metastable cubic TiAlN coatings of the last ten years. Furthermore, it is evident that critical solubility predictions for the design of metastable materials are flawed, if the previously overlooked surface energy contribution to the total energy is not considered.

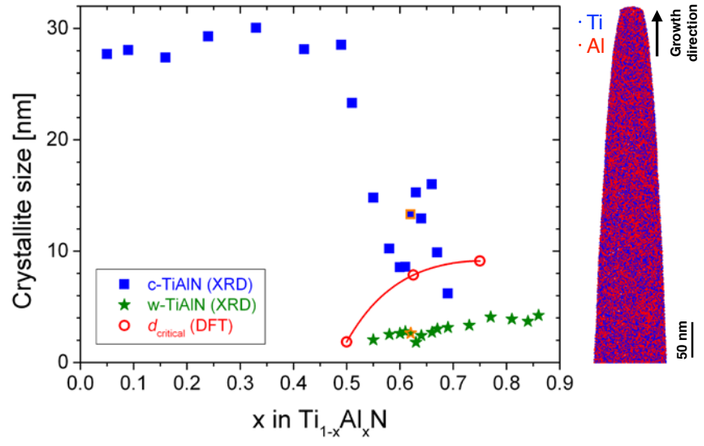

Conference contributions

- DENIS MUSIC
  Holistic Design of Multifunctional Nitrides, Oxides and Oxynitrides, Invited Talk at International Conference on Metallurgical Coatings and Thin Films (ICMCTF), San Diego, USA, April 23, 2018
- MARCUS HANS
  Stress-Dependent Elasticity of TiAlN coatings, Contributed Talk at International Conference on Metallurgical Coatings and Thin Films (ICMCTF), San Diego, USA, April 27, 2018
- MARCUS HANS
  Local chemical composition of hard coatings at the nanometer scale revealed by atom probe tomography, Invited Talk at 9th International Workshop on High-Resolution Depth profiling, Uppsala, Sweden, June 27, 2018
- JOCHEN M. SCHNEIDER
  Quantum mechanically guided design of borides or experimentally guided quantum mechanical calculations?, Invited Talk at 83rd IUVSTA Workshop, Vadstena, Sweden, September 04, 2018

National and international cooperations

- GRZEGORZ GRECZYNSKI, Linköping University, Sweden
- DAVID HOLEC, Montanuniversität Leoben, Austria
- PETER AWAKOWICZ, Ruhr-Universität Bochum, Germany

Quantum mechanically guided design of medium and high manganese steels

Project ID: jara0152
JOCHEN M. SCHNEIDER
Materials Chemistry,
RWTH Aachen University

P. KEUTER
AND F. HERRIG
Materials Chemistry,
RWTH Aachen University

Scientific work accomplished and results obtained

This status report on the JARA computing time pertains to the peer-reviewed DFG research project SFB 761 on austenitic steels. We have applied for 2.8 million core hours, but only 1.5 million core hours were granted, which limited the execution of this project. The following scientific work on was accomplished within the granted period.

High Mn and medium Mn steels are studied within this project. Mn promotes the formation of fcc (austenite) steels. At higher Mn concentrations (order of 25 at.%), only fcc forms with antiferromagnetic (AFM) ordering and these steels constitute the next generation of high strength steels known as high Mn steels.[1] These steels can plastically deform by twinning or phase transformation to hcp, which depends on the exact Mn content, among other parameters. At lower Mn concentrations (typically 10–15 at.%), a phase mixture of fcc (AFM ordering) and bcc (ferromagnetic (FM) ordering, ferrite) occurs.[2] Al as an additional element is introduced to further tune the mechanical properties (additional deformation mechanisms) and decrease the hydrogen uptake (hence lower hydrogen embrittlement occurs), but due to these additions κ-carbides (perovskite, FM ordering) can precipitate. Formation of these nanosized κ-$(Fe,Mn)_3AlC$ precipitants causes coherency strains and affect both strength and ductility of these steels.[3] However, the correlation between chemical composition, structure, coherency induced stress, and elastic properties of the phase pure κ-$(Fe,Mn)_3AlC$ phase has not been systematically investigated yet. The influence of chemical composition and stress on the elastic properties of κ-$(Fe,Mn)_3AlC$was predicted by density functional theory calculations of stoichiometric κ as well as C and Al vacancy and Al antisite containing defect configurations accounting for deviations from the stoichiometric composition and experimentally validated by nanoindentation of combinatorial thin films.[4] Based on x-ray diffraction and elastic recoil detection analysis calibrated energy dispersive x-ray analysis data, the as deposited phase pure κ-$(Fe,Mn)_3AlC$ thin films exhibit an Al/C ratio between 0.55 and 1.24 (14–20 at.% Al and 25–16 at.% C) for Fe/Mn ≈ 1 as well as an Al/C ratio between 0.48 and 1.28 (13–20 at.% Al and 28–16 at.% C) for Fe/Mn ≈ 3.5.4 Based on the Debye-Grüneisen model,[5] the elastic modulus for stoichiometric κ-$(Fe,Mn)_3AlC$ is 313 GPa.[4] The elastic modulus is reduced by 16% to 264 GPa upon 12.5% C vacancy formation and by 20% to 249 GPa upon 12.5% Al vacancy formation.[4] The reduced elastic moduli can be rationalized by considering the defect structure induced changes in averaged bond energy. The average bond energy of the stoichiometric configuration is -0.830 eV/atom, being weakened by 2.78% and 1.40% upon C and Al vacancy formation, respectively.[4] Furthermore, we predict significant stress induced elastic modulus changes: a compressive stress of 2 GPa will cause a 31 GPa increase in elastic modulus for the stoichiometric configuration.[4] This prediction can be understood based on pressure induced bond strengthening and could be verified for $\kappa(Fe,Mn)_3AlC$ thin films exhibiting a tensile stress of up to 1.3 GPa: the theoretical values constitute the upper bound for the experimental elastic modulus values.[4] The here communicated experimentally determined elastic modulus values are in good agreement with the predicted values.[4] These findings are relevant for (bulk) nanosized κ-precipitates in an austenitic Fe-Mn-Al-C matrix as their formation causes coherency strains.

Austenite (fcc) is a high-temperature phase. Stabilization by Mn additions is a promising pathway,[1] but it also brings challenges due to Mn evaporation at elevated temperatures.[6] Thus, evaporation induced roughening of fcc Fe-Mn based thin films is a serious issue. A low temperature deposition strategy for the growth of smooth fcc FeMn thin films was developed in this project.[7] Density functional theory calculations suggest that the layer structure α-Al_2O_3(0001)/Cu(111) exhibits higher interfacial strength than MgO(001)/Cu(001) and is thus chosen as substrate/nucleation layer combination to enable (local) epitaxial growth of fcc Cu(111) on α-Al_2O_3(0001) as well as (local) epitaxial growth of fcc FeMn(111) on fcc Cu(111).[7] The work of separation between Cu and $Fe_{0.6}Mn_{0.4}$ does not differ significantly between the two configurations studied, and, as such, is not decisive regarding the selection of the substrate system.[7] However, the α-Al_2O_3(0001)/Cu(111) interface exhibits a more than six times higher work of separation (5.48 J/m²) than the MgO(001)/Cu(001) interface (0.85 J/m²) and hence strong interfacial bonding.[7] This distinct difference in the calculated work of separation can be understood based on the Cu coordination at the interface, which is 1 between Cu and O for MgO(001)/Cu(001) but 3 for α-Al_2O_3(0001)/Cu(111).[7] The low temperature deposition strategy for the growth of smooth fcc FeMn thin films was critically appraised by synthesizing a 100 nm thick (combinatorial) FeMn thin film on a 10 nm Cu nucleation layer which was in turn deposited on an α-Al_2O_3(0001) substrate (α-Al_2O_3/Cu/FeMn).[7] X-ray diffraction confirms the phase formation of fcc FeMn for Mn contents above 39 at.%.[7] The (local) epitaxial growth of fcc $Fe_{0.58}Mn_{0.42}$(111) on fcc Cu(111) on α-Al_2O_3(0001) is verified by transmission electron microscopy with the following orientation relationship: α-Al_2O_3(0006) || Cu/$Fe_{0.58}Mn_{0.42}$(-1-11) and α-Al_2O_3(0-330) || Cu/$Fe_{0.58}Mn_{0.42}$(2-20).[7] The thin film exhibits the desired low surface roughness with R_a values as low as 0.6 nm, which is on the same order of magnitude as the α-Al_2O_3 substrate (R_a ~ 0.1 nm) and at least two orders of magnitude lower than the fcc FeMn based thin films deposited at high temperatures ($R_a \geq 58$ nm).[7] Thus, the introduced synthesis strategy opens the possibility of the successful implementation of thin film model systems for materials with interface dominated properties such as FeMn based steels containing κ-carbide precipitates.

Realization of the project

The granted computing time has been used completely and we have not modified any codes run in this JARA project. We have employed the following density functional theory[8] based codes:

- VASP (commercial code (license Nr. 5-94), version 5.4, www.vasp.at)
- OpenMX (open-source code, version 3.8, www.openmx-square.org)
- LOBSTER (open-source code, version 2.2, www.cohp.de)

During the duration of this JARA project, 72-92 cores were used. In the course of structural relaxations at 0 K or density functional theory (ab initio) based molecular dynamics runs, maximum time (120 hours) was consecutively applied up to 20 times.

Publications with project results

(i) F. HERRIG, D. MUSIC, H. RUESS, A.-L. RAVENSBURG, P. J. PÖLLMANN, AND J. M. SCHNEIDER,
Scr. Mater. 153, 49 (2018)
(ii) F. HERRIG, D. MUSIC, B. VÖLKER, M. HANS, P. J. PÖLLMANN, A. L. RAVENSBURG, AND J. M. SCHNEIDER,
Metals 8, 384 (2018)

Theses completed within the project

(i) F. HERRIG
Ab initio guided thin film model systems for FeMn based steels, submitted

Additional references

[1] FROMMEYER G, BRÜX U, NEUMANN P.
ISIJ Int. 2003;43:438.
[2] ZHANG R, CAO WQ, PENG ZJ, SHI J, DONG H, HUANG CX.
Mater. Sci. Eng. 2013;A583:84.

[3] YAO MJ, WELSCH E, PONGE D, HAGHIGHAT SMH, SANDLÖBES S, CHOI P, HERBIG M, BLESKOV I, HICKEL T, LIPINSKA-CHWALEK M, SHANTHRAJ P, SCHEU C, ZAEFFERER S, GAULT B, RAABE D. Acta Mater. 2017;140:258.
[4] HERRIG F, MUSIC D, RUESS H, RAVENSBURG AL, PÖLLMANN PJ, SCHNEIDER JM. Scr. Mater. 2018;153:49.
[5] MUSIC D, GEYER RW, KEUTER P. Appl. Phys. Lett. 2016;109:223903.
[6] REEH S, MUSIC D, GEBHARDT T, KASPRZAK M, JÄPEL T, ZAEFFERER S, RAABE D, RICHTER S, SCHWEDT A, MAYER J, WIETBROCK B, HIRT G, SCHNEIDER JM. Acta Mater. 2012;60:6025.
[7] HERRIG F, MUSIC D, VÖLKER B, HANS M, PÖLLMANN PJ, RAVENSBURG AL, SCHNEIDER JM. Metals. 2018;8:384.
[8] HOHENBERG P, KOHN W. Phys. Rev. 1964;136:B864.

Material suitable for the general public

Although the formation of nanosized κ-precipitates in austenitic Fe-Mn-Al-C matrices causes coherency strains and affect both strength and ductility, the composition and stress dependence of the elastic properties has not been studied systematically for $(Fe, Mn)_3AlC$. An elastic modulus decrease upon C and Al-vacancy formation and variations due to stress was predicted and experimentally verified and related to changes average bond energy [F. Herrig, D. Music, H. Rueß, A.-L. Ravensburg, P. J. Pöllmann, and J. M. Schneider, Scr. Mater. 153, 49 (2018)]. This is a crucial step towards interface design of high Mn steels.

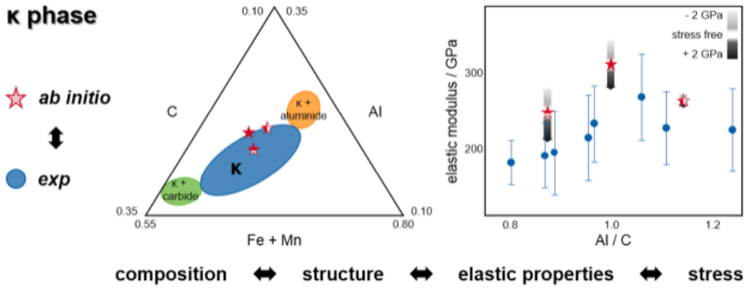

National and international cooperations

- IGOR ABRIKOSOV, Linköping University, Sweden
- LEVENTE VITOS, Royal Institute of Technology Stockholm, Sweden
- TILMANN HICKEL, Max-Planck-Institut für Eisenforschung GmbH, Germany

Electrical Engineering and Information Technology | DFG 408

Versatile Video Coding

Project ID: jara0333
CHRISTIAN ROHLFING
MATHIAS WIEN
MAX BLÄSER
JOHANNES SAUER
Institut für Nachrichtentechnik, RWTH Aachen University

MPEG Standardization

The Joint Video Experts Team (JVET), a collaborative team formed by MPEG and ITU-T Study Group 16's VCEG started work on a new video compression standard nicknamed as "Versatile Video Coding" (VVC) in April 2018 during the MPEG Meeting in San Diego. The new standard will likely be finished by the year 2020. The design goal of the new standard is to double the compression efficiency compared to previous MPEG standards and thereby making new and emerging applications such as UHD video streaming and immersive video widely available.

The Institut für Nachrichtentechnik (IENT) from RWTH Aachen University has participated in the "Joint Call for Proposals on Video Compression with Capability beyond HEVC" (CfP) which was issued by JVET in October 2017 and has contributed to the development of the new standard since then.

An essential requirement for being able to contribute to the development of the new standard is the ability to perform a large amount of video encoding and decoding using an experimental, software-based codec called the VTM software (VVC Test Model). Any new algorithm or modification to already existing technology that is presented at JVET must be thoroughly tested and evaluated by coding a pre-defined set of video sequences with different characteristics. Both the software usage and the test set of video sequences are specified by the so called "Common Testing Conditions", which apply for all standardization participants.

With the computing power of the HPC, the IENT was able to contribute to the following core experiments (CEs) of the standard:

- CE10: Combined and Multi-Hypothesis Prediction
- CE13: Coding Tools for 360° Omnidirectional Video

Further, cross-checks of experimental results obtained by other standardization participants were performed.

2D Video Coding

In the CE10 contributions by IENT, new algorithms were evaluated that perform non-rectangular block partitioning of the video, which is of particular importance for 2D video coding applications. Non-rectangular partitioning, especially geometry-based partitioning for motion compensated prediction as proposed by IENT, has the prospect of improving coding efficiency by up to 1%, as the more flexible partitioning allows better

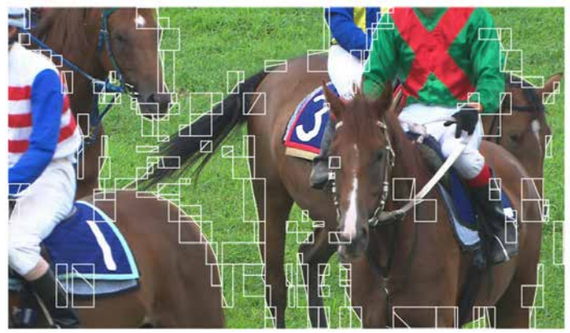

Fig.1: Example of a coded picture using non-rectangular block partitioning.

adaption to the local properties of the video. Besides better coding efficiency, it has been demonstrated that the subjective visual quality can benefit from non-rectangular partitioning at low bit rates. Figure 1 exemplifies how the proposed partitioning method adapts to the video content.

360° Video Coding

In the contributions by IENT to CE13, new tools targeting better compression of 360° video were investigated. The native format of 360° content is video on a sphere surface. However for coding, lossy conversion to a 2-dimensional representation of the video is necessary. IENT investigated the impact of geometric distortions in 360° video projected to a cube, which is then unfolded to obtain a 2-dimensional representation for coding. In particular, a geometry-corrected motion compensation method was developed, which improves the prediction across cube face boundaries, as exemplified in Figure 2. The coding efficiency can be increased by up to 2% using this novel prediction method. Further, IENT developed a method for improved loop filtering across face boundaries. While this method does not impact the objective quality measurements, the improvements can clearly be seen visually.

(a) Face A and B. Red: Geometric distortion at face boundary

(b) Blue: Corrected geometric distortion.

Fig. 2: (Corrected) geometric distortions between cube face A and neighbor face B (Straight lines bend at face border)

Publications

[1] SAUER J, BLÄSER M.
Coding of 360° video in PHEC using different numbers of tiles per face.
Doc. JVET-N0219, JVET. Mar. 2019.

[2] BLÄSER M, SAUER J.
CE10-related: Bi-directionalmotionvectorstorage for triangular prediction.
Doc. JVET-M0581, JVET. Marrakesh, Morocco. Jan. 2019.

[3] BLÄSER M, SAUER J.
CE10-related: Triangular prediction with MMVD.
Doc. JVET-M0736, JVET. Marrakesh, Morocco. Jan. 2019.

[4] SAUER J, BLÄSER M.
CE13: Results on CE13.2.2 and CE13.5.2.
Doc. JVET-M0355, JVET. Marrakesh, Morocco. Jan. 2019.

[5] SAUER J, BLÄSER M.
360° coding tools using uncoded areas.
Doc. JVET-M0547, JVET. Marrakesh, Morocco. Jan. 2019.

[6] BLÄSER M.
Crosscheck of JVET-L0124: CE10.3.1.b Triangular prediction unit mode.
Doc. JVET-L0463, JVET. Macau SR, China. Oct. 2018.

[7] BLÄSER M, SAUER J.
CE10: Results on Geometric Partitioning (Experiments 3.2.a - 3.2.c).
Doc. JVET-L0417, JVET. Macau SR, China. Oct. 2018.

[8] SAUER J, BLÄSER M.
CE13: Results on CE13.3.2, CE13.4.3 and CE13.7.7.
Doc. JVET-L0211,
JVET. Macau SR, China. Oct. 2018.

[9] SAUER J, BLÄSER M.
CE13-related: Results for experiments as CE13.3.2, CE13.4.3 and CE13.7.7 with PHEC and impact of rotation on the coding performance of PHEC.
Doc. JVET-L0212, JVET. Macau SR, China. Oct. 2018.

[10] BLÄSER M, SAUER J.
CE10: Results on Geometric block partitioning (Test 3.3).
Doc. JVET-K0146, JVET. Ljubljana, Slovenia. July 2018.

[11] SAUER J, SCHNEIDER J, BLÄSER M, WIEN M.
Reference software extension for coding block statistics.
Doc. JVET-K0149, JVET. Ljubljana, Slovenia. Jul. 2018.

[12] BLÄSER M, SAUER J, WIEN M.
Description of SDR and 360° video coding technology proposal by RWTH Aachen University. Doc. JVET-J0023, JVET. San Diego, USA. Apr. 2018.

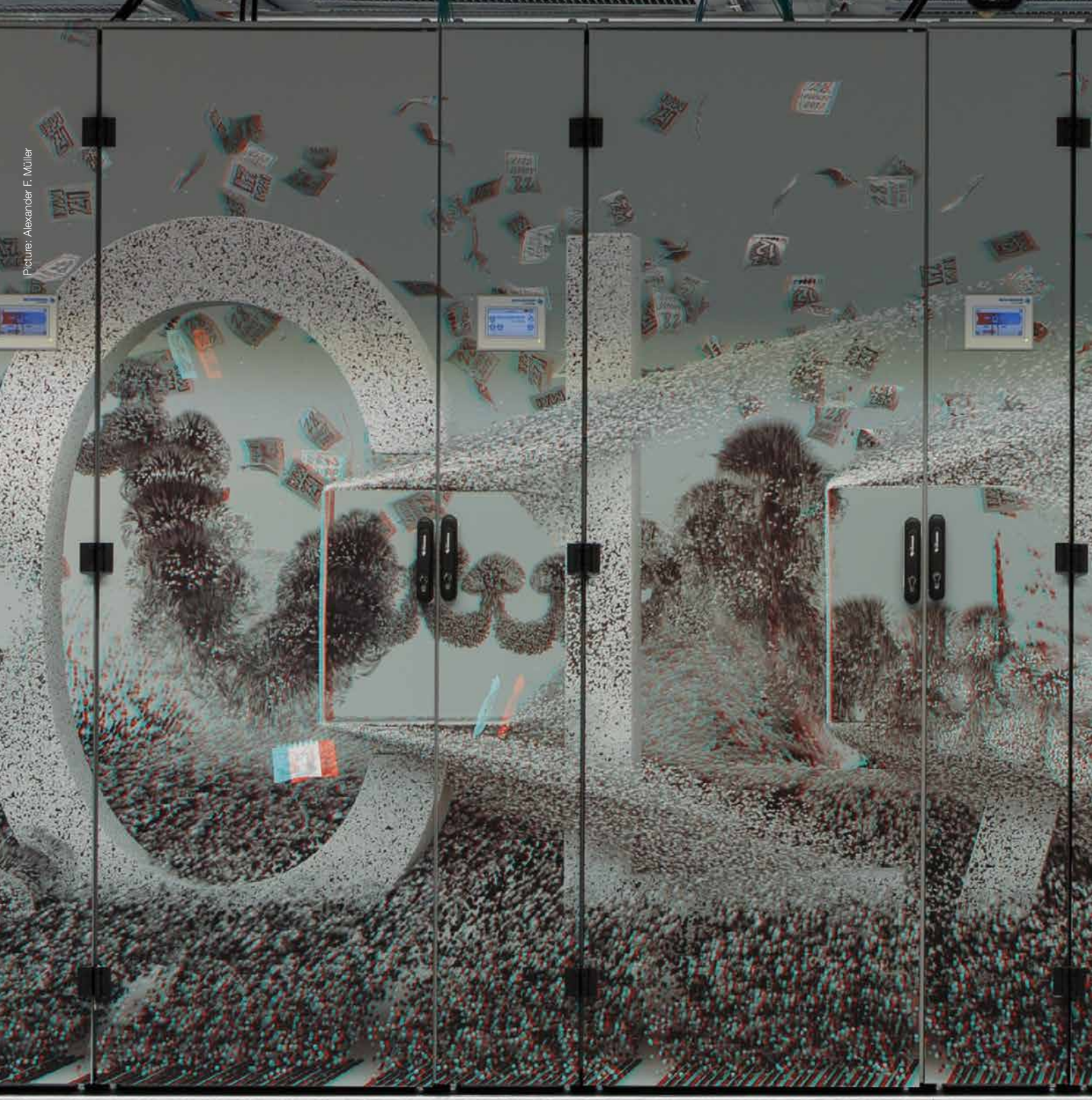

Picture: Alexander F. Müller

Thinking the Future
Zukunft denken